Title

Chemical and Cellular Formation of Reactive Oxygen Species from Secondary Organic Aerosols in Epithelial Lining Fluid.

Authors

Shiraiwa, M

Fang, T

Wei, J

et al.

Publication Date

2023-12-01

INVESTIGATORS' REPORT

Chemical and Cellular Formation of Reactive Oxygen Species from Secondary Organic Aerosols in Epithelial Lining Fluid

Manabu Shiraiwa,[1] Ting Fang,[1] Jinlai Wei,[1] Pascale S.J. Lakey,[1] Brian C.H. Hwang,[1] Kasey C. Edwards,[1] Sukriti Kapur,[1] Jessica E. Monterrosa Mena,[2] Yu-Kai Huang,[3] Michelle A. Digman,[3] Scott A. Weichenthal,[4] Sergey Nizkorodov,[1] Michael T. Kleinman[2]

[1]Department of Chemistry, University of California, Irvine, CA, USA; [2]Division of Occupational and Environmental Medicine, University of California, Irvine, CA, USA; [3]Department of Biomedical Engineering, University of California, Irvine, CA, USA; [4]Department of Epidemiology, Biostatistics and Occupational Health, McGill University, Montreal, Canada

ABSTRACT

INTRODUCTION

Oxidative stress mediated by reactive oxygen species (ROS*) is a key process for adverse aerosol health effects. Secondary organic aerosols (SOA) account for a major fraction of particulate matter with aerodynamic diameter ≤2.5 μm ($PM_{2.5}$). $PM_{2.5}$ inhalation and deposition into the respiratory tract causes the formation of ROS by chemical reactions and phagocytosis of macrophages in the epithelial lining fluid (ELF), but their relative contributions are not well quantified and their link to oxidative stress remains uncertain. The specific aims of this project were (1) elucidating the chemical mechanism and quantifying the formation kinetics of ROS in the ELF by SOA; (2) quantifying the relative importance of ROS formation by chemical reactions and macrophages in the ELF.

METHODS

SOA particles were generated using reaction chambers from oxidation of various precursors including isoprene, terpenes, and aromatic compounds with or without nitrogen oxides (NO_x). We collected size-segregated PM at two highway sites in Anaheim, CA, and Long Beach, CA, and at an urban site in Irvine, CA, during two wildfire events. The collected particles were extracted into water or surrogate ELF that contained lung antioxidants. ROS generation was quantified using electron paramagnetic resonance (EPR) spectroscopy with a spin-trapping technique. PM oxidative potential (OP) was also quantified using the dithiothreitol assay. In addition, kinetic modeling was applied for analysis and interpretation of experimental data. Finally, we quantified cellular superoxide release by RAW264.7 macrophage cells upon exposure to quinones and isoprene SOA using a chemiluminescence assay as calibrated with an EPR spin-probing technique. We also applied cellular imaging techniques to study the cellular mechanism of superoxide release and oxidative damage on cell membranes.

RESULTS

Superoxide radicals ($\cdot O_2^-$) were formed from aqueous reactions of biogenic SOA generated by hydroxy radical (·OH) photooxidation of isoprene, β-pinene, α-terpineol, and d-limonene. The temporal evolution of ·OH and $\cdot O_2^-$ formation was elucidated by kinetic modeling with a cascade of aqueous reactions, including the decomposition of organic hydroperoxides (ROOH), ·OH oxidation of primary or secondary alcohols, and unimolecular decomposition of α-hydroxyperoxyl radicals. Relative yields of various types of ROS reflected the relative abundance of ROOH and alcohols contained in SOA, which generated under high NO_x conditions, exhibited lower ROS yields. ROS formation by SOA was also affected by pH. Isoprene SOA had higher ·OH and organic radical yields at neutral than at acidic pH. At low pH $\cdot O_2^-$ was the dominant species generated by all types of SOA. At neutral pH, α-terpineol SOA exhibited a substantial yield of carbon-centered organic radicals (R·), while no radical formation was observed by aromatic SOA.

Organic radicals in the ELF were formed by mixtures of Fe^{2+} and SOA generated from photooxidation of isoprene, α-terpineol, and toluene. The molar yields of organic radicals by SOA were 5–10 times higher in ELF than in water. Fe^{2+} enhanced organic radical yields by a factor of 20–80. Ascorbate mediated redox cycling of iron ions and sustained organic peroxide decomposition, as supported by kinetic modeling reproducing time- and concentration-dependence

This Investigators' Report is one part of Health Effects Institute Research Report 215, which also includes a Commentary by the Review Committee and an HEI Statement about the research project. Correspondence concerning the Investigators' Report may be addressed to Dr. Manabu Shiraiwa, University of California, Irvine, Department of Chemistry, 1120 Natural Sciences II, Irvine, California, 92697-2025; email: *m.shiraiwa@uci.edu*. No potential conflict of interest was reported by the authors.

Although this document was produced with partial funding by the United States Environmental Protection Agency under Assistance Award CR–83998101 to the Health Effects Institute, it has not been subjected to the Agency's peer and administrative review and therefore may not necessarily reflect the views of the Agency, and no official endorsement by it should be inferred. The contents of this document also have not been reviewed by private party institutions, including those that support the Health Effects Institute; therefore, it may not reflect the views or policies of these parties, and no endorsement by them should be inferred.

* A list of abbreviations and other terms appears at the end of this volume.

of organic radical formation, as well as by additional experiments observing the formation of Fe^{2+} and ascorbate radicals in mixtures of ascorbate and Fe^{3+}. ·OH and superoxide were found to be efficiently scavenged by antioxidants.

Wildfire PM mainly generated ·OH and R· with minor contributions from superoxide and oxygen-centered organic radicals (RO·). PM OP was high in wildfire PM, exhibiting very weak correlation with radical forms of ROS. These results were in stark contrast with PM collected at highway and urban sites, which generated much higher amounts of radicals dominated by ·OH radicals that correlated well with OP. By combining field measurements of size-segregated chemical composition, a human respiratory tract model, and kinetic modeling, we quantified production rates and concentrations of different types of ROS in different regions of the ELF by considering particle-size-dependent respiratory deposition. While hydrogen peroxide (H_2O_2) and $\cdot O_2^-$ production were governed by Fe and Cu ions, ·OH radicals were mainly generated by organic compounds and Fenton-like reactions of metal ions. We obtained mixed results for correlations between PM OP and ROS formation, providing rationale and limitations of the use of oxidative potential as an indicator for PM toxicity in epidemiological and toxicological studies.

Quinones and isoprene SOA activated nicotinamide adenine dinucleotide phosphate (NADPH) oxidase in macrophages, releasing massive amounts of superoxide via respiratory burst and overwhelming the superoxide formation by aqueous chemical reactions in the ELF. The threshold dose for macrophage activation was much smaller for quinones compared with isoprene SOA. The released ROS caused lipid peroxidation to increase cell membrane fluidity, inducing oxidative damage and stress. Further increases of doses led to the activation of antioxidant response elements, reducing the net cellular superoxide production. At very high doses and long exposure times, chemical production became comparably important or dominant if the escalation of oxidative stress led to cell death.

CONCLUSIONS

The mechanistic understandings and quantitative information on ROS generation by SOA particles provided a basis for further elucidation of adverse aerosol health effects and oxidative stress by $PM_{2.5}$. For a comprehensive assessment of PM toxicity and health effects via oxidative stress, it is important to consider both chemical reactions and cellular processes for the formation of ROS in the ELF. Chemical composition of PM strongly influences ROS formation; further investigations are required to study ROS formation from various PM sources. Such research will provide critical information to environmental agencies and policymakers for the development of air quality policy and regulation.

INTRODUCTION

Anthropogenic air pollution leads to a massive increase of atmospheric $PM_{2.5}$ and oxidant concentrations on local, regional, and global scales, posing a major threat to public health (Monks et al. 2009; Pöschl and Shiraiwa 2015). The concentrations of $PM_{2.5}$ in polluted urban air are several orders of magnitude higher than in pristine air (~10-1000 μg m^{-3} vs. ~1-10 μg m^{-3}) (Pöschl and Shiraiwa 2015), and high pollutant levels can cause serious respiratory and cardiovascular diseases, leading to elevated mortality (Brunekreef and Holgate 2002; Lim et al. 2013; Pope and Dockery 2006; Rich et al. 2013). Epidemiological studies have shown a clear correlation between air pollutants and adverse health effects, including cardiovascular, respiratory, and allergic diseases (Dockery et al. 1993). Ambient and indoor air pollution by airborne PM and ozone (O_3) are among the most prominent leading risk factors for the global burden of disease (Lim et al. 2013). For example, mortality rates in the 90 largest U.S. cities were found to rise on average by 0.5% with each 10-μg m^{-3} increase in $PM_{2.5}$ (Kaiser 2000), and globally the annual number of premature deaths due to air pollution are estimated to exceed 3 million with an increasing trend (Lelieveld et al. 2015; Shiraiwa et al. 2017). However, the underlying chemical processes are poorly characterized, and a quantitative basis for assessing the relative importance of specific air pollutants is still missing (Dockery et al. 1993; Shiraiwa et al. 2017; West et al. 2016).

Organic aerosols account for a major fraction of $PM_{2.5}$ in the atmosphere (Huang et al. 2014; Jimenez et al. 2009). Formation and growth of SOA is triggered by reactions of O_3 and ·OH radicals with volatile organic compounds emitted from various biogenic and anthropogenic sources. With regard to SOA health effects, substantial amounts of particle-bound ROS are found on ambient and laboratory-generated SOA produced from various precursors such as α-pinene, limonene, linalool, and toluene (Chen et al. 2011b; Pavlovic and Hopke 2010; Venkatachari et al. 2005, 2007; Wang et al. 2010, 2011b, 2012; Zhao and Hopke 2012). Several groups have measured ROS in aerosol particles with offline analysis (Cho et al. 2005; Dellinger et al. 2007; Gehling and Dellinger 2013; Khachatryan et al. 2011; Kumagai et al. 1997; Venkatachari et al. 2005) and online systems (Fang et al. 2015; Fuller et al. 2014; Wang et al. 2011a). In addition, ROOH and peroxides were found to be major constituents of biogenic SOA and aged organic aerosol (Docherty et al. 2005; Epstein et al. 2014; Surratt et al. 2006; Ziemann and Atkinson 2012). Recently, highly oxygenated organic molecules (HOM) and extremely low volatility organic compounds (ELVOC), which contain multiple hydroperoxide functional groups formed by autoxidation (Crounse et al. 2013), are found to be an important constituent of SOA (Ehn et al. 2012, 2014; Jokinen et al. 2015; Mentel et al. 2015; Tröstl et al. 2016). Recent studies have

shown that such HOM or ELVOC compounds are relatively unstable (Badali et al. 2015; Krapf et al. 2016), and they may decompose upon interactions with water to form free radicals (Riva 2016; Tong et al. 2016).

ROS are key species of both atmospheric and physiological chemistry. ROS play a central role in the adverse health effects of air pollution, as they can cause oxidative stress (Finkel and Holbrook 2000; Nel 2005; Winterbourn 2008). ROS are defined to include hydroxyl radical (·OH), $\cdot O_2^-$, H_2O_2, and O_3, as well as a wide range of R· and RO·, such as peroxy and alkoxy radicals (Finkel and Holbrook 2000; Shiraiwa et al. 2012; Winterbourn 2008). Fine air PM contains redox-active components like transition metals and quinones originating from gasoline and diesel motor exhaust, cigarette smoke, and other sources including SOA formation in the atmosphere (Cho et al. 2005; Kumagai et al. 2012; McWhinney et al. 2013; Verma et al. 2015a). Quinones are often associated with atmospheric humic-like substances (HULIS) (Dou et al. 2015; Lin and Yu 2011; Verma et al. 2015b). Upon inhalation and deposition in the human respiratory tract, such air pollutants can induce and sustain chemical reactions that produce ROS in the ELF covering the airways (Gurgueira et al. 2002; Lakey et al. 2016). The ELF contains a range of antioxidants and surfactants (van der Vliet et al. 1999), and it extends from the nasal cavity to the pulmonary alveoli with a film thickness that decreases from several micrometers in the upper airways to dozens of nanometers in the lungs (Mudway and Kelly 2000). As illustrated in **Figure 1**, the redox-active pollutants and ROS undergo a multitude of radical and redox reaction cycles in the ELF. The initial step is the transfer of electrons from antioxidants to transition metal ions or quinones, forming reduced metal ions or semiquinones, respectively (Charrier et al. 2014; Kumagai et al. 2012; Pöschl and Shiraiwa 2015). Transition metal ions and quinones are regenerated by reaction with molecular oxygen (O_2) forming $\cdot O_2^-$ radicals that are further converted into H_2O_2 (Winterbourn 2008). ·OH radicals, the most reactive form of ROS, can be produced via Fenton-like reactions of H_2O_2 with iron or copper ions (Charrier and Anastasio 2011) and can also be released upon interaction of SOA with water (Tong et al. 2016; Wang et al. 2011b). These multiphase processes have been investigated experimentally, quantifying formation of ·OH and H_2O_2 by transition metal ions and quinones in surrogate lung lining fluid (Charrier and Anastasio 2011; Charrier et al. 2014; Jung et al. 2006; Shen and Anastasio 2011; Vidrio et al. 2008).

Macrophages are sentinel cells and the first cellular responders of the innate immune system, serving several important roles in host defense: they clear dead tissues and

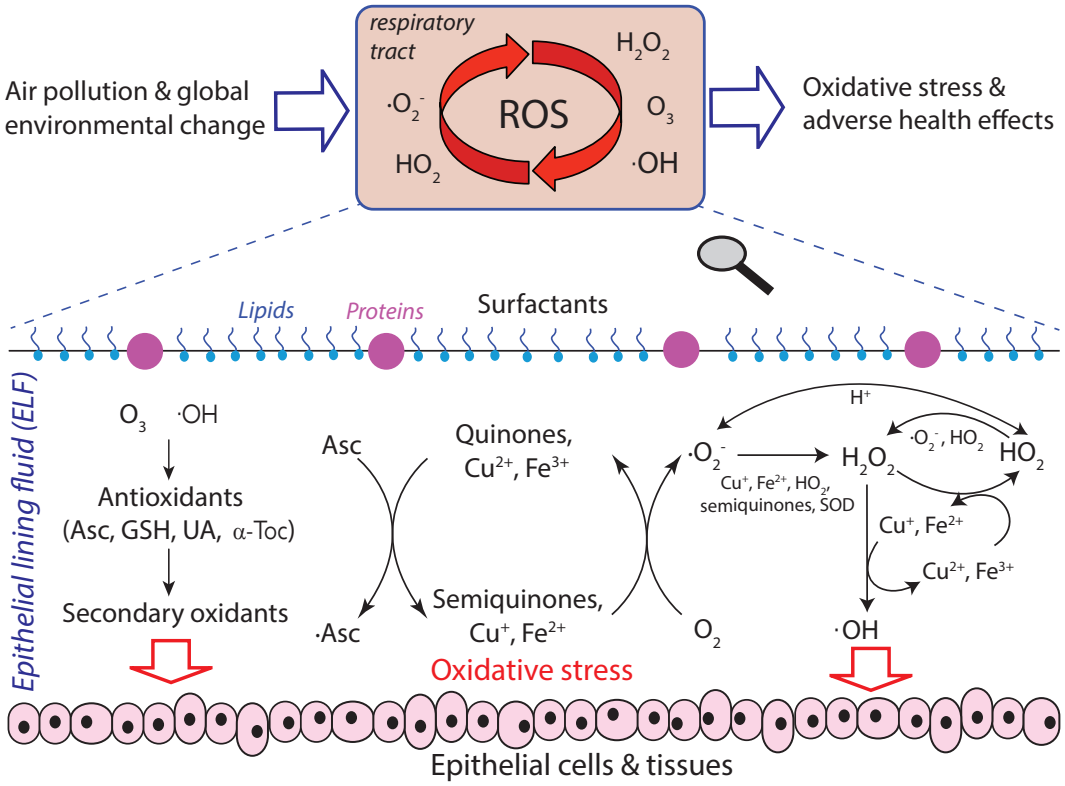

Figure 1. Interaction of air pollutants and ROS in the ELF of the human respiratory tract. Redox-active components trigger and sustain catalytic reaction cycles generating ROS. Asc = ascorbate; ·Asc = ascorbate radicals; H_2O_2 = hydrogen peroxide; HO_2 = hydroperoxyl radical; GSH = glutathione; O_2 = molecular oxygen; $\cdot O_2^-$ = superoxide radical; O_3 = ozone; ·OH = hydroxyl radical; SOD = superoxide dismutase; UA = uric acid; α-Toc = α-tocopherol. Adapted from Lakey et al. 2016.

initiate the process of tissue repair, they ingest and destroy microbes, and they produce cytokines to induce and regulate inflammation (Abbas et al. 2010; Sompayrac 2022). Alveolar macrophages reside in the ELF, protecting the lung cells and tissues from infection from bacteria, microbes, and pathogens. Macrophages may be activated by two different pathways: classical macrophage activation is triggered by innate immune signals. Activated macrophages called M1 are involved in destroying microbes and triggering inflammation, whereas M2 macrophages, by alternative macrophage activation induced by cytokines, is relevant for tissue repair and termination of inflammation (Abbas et al. 2010). M1 macrophages release $\cdot O_2^-$ after phagocytosis through a process called the *respiratory burst* due to transient consumption of O_2 (Forman and Torres 2002). This process also occurs upon exposure to atmospheric PM (Beck-Speier et al. 2005; Gurgueira et al. 2002; Kleinman et al. 2000).

Thus, ROS can be released both chemically and cellularly upon particle deposition, but the relative importance of cellular and chemical ROS is poorly understood and yet to be quantified. A previous study has quantified chemical and cellular H_2O_2 production from macrophages upon exposure to naphthalene SOA (Liu et al. 2020), but very limited research has been conducted in quantifying cellular $\cdot O_2^-$. Cellular release of $\cdot O_2^-$ can be triggered by a number of different enzymatic systems such as mitochondrial oxidative phosphorylation, NAD(P)H (reduced nicotinamide adenine dinucleotide [phosphate]) oxidase, and xanthine oxidase (XO) (Sachse and Wolf 2007). However, very little is known about which $\cdot O_2^-$ generation mechanism is activated by inhaled PM. Several methods have been developed to detect cellular $\cdot O_2^-$ using spectroscopic (Teufelhofer et al. 2003), fluorescent (Gomes et al. 2005; Holevinsky and Nelson 1995), or luminescent assays (Messner and Imlay 2002; Yamazaki et al. 2011). The Diogenes chemiluminescence assay is suitable for monitoring cellular $\cdot O_2^-$ production, as Diogenes is a very sensitive $\cdot O_2^-$ chemiluminescence enhancer that is nondenaturing to living cells; however, the chemiluminescence readouts show light intensity without providing a quantitative measure for production rate or concentration (Yamazaki et al. 2011).

While $\cdot O_2^-$ can be converted into a less reactive form (e.g., H_2O_2) by superoxide dismutase (SOD), excess $\cdot O_2^-$ is known to be cytotoxic as it can interfere with lipids, proteins, and DNA (Forman and Torres 2002; Kumagai et al. 1997; Sies et al. 2017; Winterbourn 2008). A specific consequence of PM-triggered $\cdot O_2^-$ is yet to be identified. The antioxidant defense system can counteract ROS; however, excessive production of ROS can overwhelm antioxidant defenses and trigger or enhance oxidative stress, cell death, and biological aging (Finkel and Holbrook 2000; Lucas and Maes 2013; Nel 2005; Shiraiwa et al. 2012; Winterbourn 2008). Thus, characterizing the formation of ROS in the ELF is crucial for understanding how air pollution leads to adverse health effects like asthma, allergies, and other respiratory diseases. The production rate and concentration of ROS induced by SOA in the ELF, however, so far have hardly been quantified.

SPECIFIC AIMS AND STUDY DESIGN

ROS play a central role in the adverse health effects of air PM. ROS release induced by particles can be counteracted by the antioxidant defense system; however, it can be overwhelmed by excessive ROS production, triggering oxidative stress (Kumagai et al. 1997; Nel 2005; Shiraiwa et al. 2012; Winterbourn 2008). ROS are coupling atmospheric and physiological chemistry, but their interactions at ELF are not well understood and less quantified. Particularly poorly characterized is the role of ROS upon respiratory deposition of SOA, as multiphase chemistry in the ELF is highly complex — involving redox-active components, lung antioxidants, and ROS. Previous studies (Charrier and Anastasio 2011; Charrier et al. 2014; Cho et al. 2005; Kumagai et al. 1997), including our research team's contributions (Arangio et al. 2016; Lakey et al. 2016; Tong et al. 2016), have shown that SOA can generate H_2O_2 and ·OH radicals in the ELF. However, the formation of other types of ROS, including superoxide and R· and RO·, which may play an important role in oxidative stress (Birben et al. 2012; Pöschl and Shiraiwa 2015; Pryor et al. 1995; Winterbourn 2008), had been hardly studied and quantified. It was urgent to conduct further studies to fully unravel kinetics and molecular mechanism of formation of ROS by biogenic and anthropogenic SOA.

Specific Aim 1 Elucidate the chemical mechanism and quantify the formation kinetics of ROS in the ELF by SOA.

- **Task A:** Quantify ROS formation by aqueous reactions of laboratory-generated SOA.
- **Task B:** Quantify ROS formation and OP by ambient PM.

Specific Aim 2 Quantify the relative importance of chemical ROS generated by redox reactions and biological ROS released by macrophages in the ELF.

- **Task C:** Model estimation of chemical ROS concentrations in the ELF.
- **Task D:** Quantify ROS release by macrophages using chemiluminescence and EPR upon exposure to SOA.

The ultimate research goal is to advance the fundamental understanding of ROS multiphase chemistry by SOA in the ELF for better assessment, prediction, and handling of air quality and public health. The results and implications of the proposed study should be useful for air quality regulators for the design of efficient control strategies against adverse aerosol health effects. The uniqueness of this project is to quantify and compare chemical and cellular ROS production by multipollutants (e.g., SOA, transition metals) in the ELF by experiments and kinetic modeling to advance the fundamental understanding of multiphase processes of ROS for a quantitative assessment of aerosol effects on oxidative stress.

Table 1. Research Roadmap

Research Tasks and Publications	Methods
A. ROS formation from aqueous reactions of SOA A1. Superoxide formation from SOA (Wei et al. 2021b) A2. Effects of NO_x on ROS formation from SOA (Edwards et al. 2022) A3. Effects of pH on ROS formation from SOA (Wei et al. 2022b) A4. Organic radical formation by SOA in ELF (Wei et al. 2022a)	Laboratory generation of SOA EPR spectroscopy Fluorometric H_2O_2 Assay
B. ROS formation from ambient particles B1. ROS formation from highway and wildfire PM (Fang et al. 2023; Hwang et al. 2021) B2. ROS formation vs. PM oxidative potential (Fang et al. 2023; Hwang et al. 2021)	Ambient PM sampling using a high-volume sampler and MOUDI EPR spectroscopy DTT assay
C. Modeling ROS formation in ELF (Fang et al. 2019; Lelieveld et al. 2021) Side-projects: applications to epidemiological studies (Liu et al. 2022; Ripley et al. 2022; Stieb et al. 2021; To et al. 2022; Zhang et al. 2020, 2021)	Kinetic modeling
D. Cellular vs. chemical ROS in ELF (Fang et al. 2022)	Cell culture and exposure EPR spectroscopy Diogenes chemiluminescence FLIM

FLIM = fluorescence lifetime imaging microscopy; MOUDI = micro-orifice uniform deposition impactor.

METHODS

The research roadmap including research projects, resulting publications, and corresponding methods is presented in **Table 1**.

For specific aim 1, SOA particles were generated by oxidation of biogenic and anthropogenic precursors (such as isoprene, terpenes, and aromatics) in a reaction chamber under various reaction conditions (Task A). Ambient particles were collected using a high volume sampler for $PM_{2.5}$ or a cascade impactor (Task B). The collected particles on a filter were extracted into the aqueous phase, and ROS formation was measured by multiple analytical techniques (Task A, B). The main tool was EPR spectroscopy combined with a spin-trapping technique for detection of radical forms of ROS (i.e., ·OH, superoxide, R·, and RO·). H_2O_2 was quantified by a fluorometric H_2O_2 assay, and organic (hydro-)peroxides contained in SOA particles were measured with an iodometric-spectrophotometric technique. The dithiothreitol (DTT) assay was used to measure OP and redox activity of PM.

For specific aim 2, the kinetic multilayer model for surface and bulk chemistry in the ELF (KM-SUB-ELF) (Lakey et al. 2016) was developed and applied for analysis and interpretation of experimental data of chemical ROS concentrations due to redox reactions as measured by EPR (Task C). As a side project, KM-SUB-ELF was applied for field measurements of metal concentrations to estimate ROS concentrations in the ELF, which were applied for epidemiological studies. Macrophages were exposed to SOA that led to the release of superoxide, which was quantified using the Diogenes chemiluminescence as calibrated by EPR with a spin-probing technique. We also applied fluorescence lifetime imaging microscopy (FLIM) to study the cellular mechanism of superoxide release and oxidative damage on cell membranes.

PARTICLE GENERATION AND SAMPLING

Laboratory Generation of SOA Particles

SOA particles were generated from dark ozonolysis and ·OH photooxidation (SOA_{O3} and SOA_{OH}, respectively) of isoprene (Sigma-Aldrich, 99%), β-pinene (Sigma-Aldrich, 99%), α-terpineol (Arcos Organics, 97%), and d-limonene (Arcos Organics, 96%). SOA_{O3} particles were produced in an oxidation flow reactor under dry and dark conditions. Prior to each experiment, the reactor was purged with zero air (Parker 75-62 purge gas generator). O_3 was introduced into the reactor by flowing pure O_2 at 1 standard liters per minute (slm) through a commercial O_3 generator (OzoneTech OZ2SS-SS). After the O_3 concentration stabilized, pure isoprene, β-pinene, α-terpineol and d-limonene were injected into 5 slm of purge air flow separately, using a syringe pump at a rate of ~2 μL per minute. High concentrations of precursor (2.2×10^{15} cm^{-3} for isoprene and 1.4×10^{15} cm^{-3} for β-pinene, α-terpineol and d-limonene) and O_3 (1.8×10^{14} cm^{-3}) were used to generate enough material for analysis.

SOA_{OH} particles were generated in a 19 L potential aerosol mass (PAM) reactor (Kang et al. 2007). 100–500 L of VOC precursors (isoprene, β-pinene, α-terpineol and d-limonene) were placed in an open 1.5 mL amber glass vial, which was kept inside a glass bottle prior to the PAM reactor. The precursors were then injected into the chamber by a 0.5 slm of carrier flow mixed with a 6 slm of humidified (Perma Pure humidifier, MH-110-12P-4) flow of purified air from a zero-air generator (Model 7000, Environics). The ·OH radicals were generated through photolysis of water molecules by 185 nm UV radiation. The exposure time for the photooxidation of precursors in the PAM reactor was about 3 minutes with relative humidity around 30%–40%. Despite the high ·OH concentrations (~10^{11}–10^{12} cm^{-3}) compared with ambient levels (~10^{6} cm^{-3}), the PAM-generated SOA are found to be similar to ambient and chamber-generated SOA in terms of yield, oxidation state, hygroscopicity, and chemical composition (Lambe et al. 2011, 2015; Peng and Jimenez 2020). Additional advantages of the PAM reactor include shortened experimental timescales, ability to reach long photochemical ages, and minimized wall losses (Peng and Jimenez 2020).

A scanning mobility particle sizer (SMPS, Grimm Aerosol Technik) was used to record the number concentrations and size distributions of SOA produced in the PAM reactor. The typical particle diameter of SOA_{OH} ranged from 30–500 nm, and the geometric mean diameter by mass varied from 70–120 nm. Particle sampling was initiated after the number concentrations stabilized. The SOA particles were collected on 47mm polytetrafluoroethylene (PTFE) filters (Millipore FGLP04700, 0.2 µm pore size) at a flow rate of 13 slm for 40 minutes and 5 slm for 3 hours for SOA_{O3} and SOA_{OH}, respectively.

The filter samples were extracted in 1 mL spin-trap solutions (10 mM) or Milli-Q (deionized, resistivity = 18.2 M/cm) water for 7 minutes. The filter extracts were used for radical measurements or the H_2O_2 fluorometric assay, respectively. The mass difference before and after the extraction was regarded as SOA dissolved in reagents, and an average molar mass of 200 g/mol was used for the calculation of SOA molar concentrations in filter extracts. The SOA_{O3} and SOA_{OH} concentrations were in the range of 1–16 mM, and the pH of SOA extracts varied between 4 and 6. At least three samples were prepared for each SOA_{O3} and SOA_{OH} for EPR analysis and H_2O_2 measurement, respectively.

Ambient Sampling with a High-Volume Sampler and a Micro-Orifice Uniform Deposition Impactor

Highway PM A high-volume sampler (Hi-Vol, Tisch Environmental, flow rate 1.13 m^3 min^{-1}) was used to collect ambient $PM_{2.5}$ onto prebaked 8" × 10" micro-quartz filters at an urban site (a campus building at the University of California, Irvine (UCI), 33°38'40.4"N 117°50'39.3"W, elevation 20 meters) and two highway sites in Anaheim (**Figure 2**, Interstate 5, 33°49'09.4"N 117°55'07.5"W) and Long Beach (Figure 2, Interstate 710, 33°51'34.0"N 118°12'01.0"W) within 20 meters of the highway roads. Interstate 5 (I-5) is one of the busiest highways in Southern California and is known as a commuter route from Orange County to the city of Los Angeles. The other highway site, Interstate 710 (I-710), is a major route that connects Long Beach and the Los Angeles city with a higher fraction of heavy-duty vehicles and is known as a heavy-duty corridor (Shirmohammadi et al. 2017). Particle filter samples were collected for 4–12 hours daily from 1/28/2020 to 2/3/2020 at the Anaheim site, for 6–12 hours per day from 2/4/2020 to 2/10/2020 (except on 2/9/2020) at the Long Beach site, and for 8–11 hours at the urban site from 2/23/2020 to 2/29/2020 (except on 2/28/2020). Field blanks were collected every other day at each site. After the collection, all filters were wrapped in a prebaked aluminum foil and immediately stored in a freezer (-18°C). Portions of the filters collected from the highway sites were cut using a circular punch with a diameter of 2.54 cm and used for measurements of environmentally persistent free radicals (EPFR), ROS, and DTT activities. Those from the urban sites were analyzed for EPFRs. Measurements of EPFRs, ROS, and DTT on each filter was repeated 3–5 times. EPFR measurements were conducted within 2 weeks of sample collection, and ROS and DTT measurements were conducted within 4–6 months. Note that EPFRs are stable at least a year after collection. Additionally, $PM_{2.5}$ samples were collected at both highway sites on one 47 mm Teflon-membrane filter and two 47 mm quartz-fiber filters in parallel using a medium-volume sampler with a Bendix Model 240 $PM_{2.5}$ cyclone. These filters were used to determine PM mass, metals, organic carbon, and elemental carbon at the highway sites. The sampling flow rate was 37.7 L min^{-1} for each filter channel. The sampling duration was 4 hours covering the following periods: 6:00–10:00, 10:00–14:00, and 14:00–18:00. The total sampling periods overlapped with the

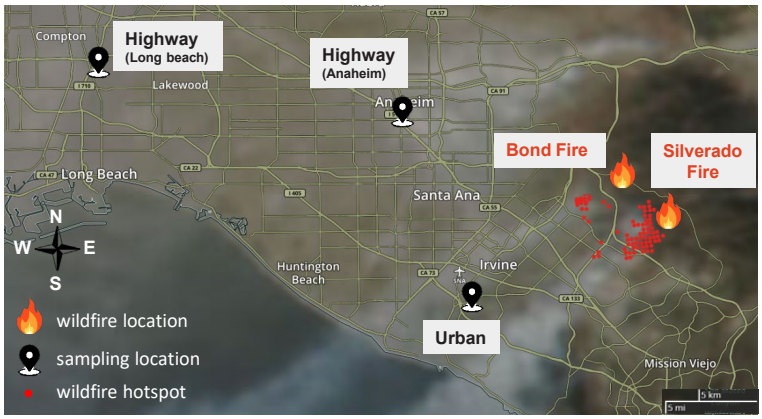

Figure 2. Sampling and wildfire locations, with smoke plumes and wildfire hotspots from the Silverado Fire as viewed by moderate resolution imaging spectroradiometer. Adapted from Fang et al. 2023.

Hi-Vol sampling periods. The Teflon-membrane filters were analyzed for $PM_{2.5}$ mass and metal, while the quartz fiber filters were analyzed for organic and elemental carbon (Wang et al. 2018).

Wildfire PM A micro-orifice uniform deposition impactor (MOUDI Model 100NR) was used to collect size-segregated ambient PM on Teflon filters (Millipore Omnipore Membrane Filter, PTFE, 0.2 μm pore size, JFWP04700) at an urban site, which is located on the rooftop of a UCI campus building at (33°38'40.4"N 117°50'39.3"W, elevation 20 meters). In winter 2020, two wildfire events occurred near the sampling site according to the California Department of Forestry and Fire Protection: Silverado and Bond Fires (Figure 2). The Silverado Fire started in Silverado Canyon (33°44'10.1"N 117°39'25.9"W) on October 26, 2020, and was contained on November 7, 2020. The Bond Fire started off the California State Route 241 in the Irvine area (33°44'37.8"N 117°40'29.9"W) on December 2, 2020, and was active for 7 days until December 10, 2020. These wildfire events were characterized with greatly reduced visibilities and substantial increases of PM mass concentrations up to 280 and 450 μg m^{-3} for the submicron (PM_1) and coarse (PM_{10}) fractions, respectively. Figure 2 shows the sampling and wildfire locations and the smoke plumes from the Silverado Fire on October 26, 2020, affecting the Irvine area. The fire location was roughly 20 kilometers from the urban sampling site.

Eight sets of MOUDI filter samples were collected at the urban location continuously for 3 days for each set during wildfire events from October 26 to December 9, 2020. Three MOUDI sets were collected at the highway sites (Anaheim site: 12 hrs on January 31, 2020; Long Beach site: 12 hrs on February 7, 2020 and 5.5 hrs on February 8, 2020). Three sets were collected for 10–12 hours daily at the urban site on February 23–25, 2020, which are considered to be urban background samples. The MOUDI was operated with selected stages with the remaining stages removed and without a back-up filter at a flow rate of 30 L min^{-1}. The 50% cut-off aerodynamic diameters used for wildfire samples were 18, 10, 1, 0.18, and 0.056 μm. Those for the highway and urban samples were 18, 10, 3.2, 1, 0.56, and 0.056 μm. EPFRs, ROS formation, and OP measured with the DTT assay (OP-DTT) in PM_1 and $PM_{1–10}$ are sums of the activities from MOUDI stages up to 1 μm and between 1 and 10 μm, respectively. Field blanks were collected without turning on the MOUDI pump at each site ($N = 11$). After the collection, all blank and sample filters were stored in petri dishes and immediately stored in a freezer (–18°C). EPFRs, ROS formation, and OP-DTT measurements were performed on these filter samples following the procedures in our previous study (Hwang et al. 2021). The data are presented as per volume of air sampled (pmol m^{-3} for EPFRv and ROSv, or nmol min^{-1} m^{-3} for total OP-DTTv) or per mass of PM (pmol μg^{-1} for EPFRm and ROSm, or nmol min-1 μg^{-1} for OP-DTTm). Frequency size distributions of EPFRs, ROS formation, and OP were calculated by dividing the size distribution with the sum of activities from all MOUDI stages. Note that frequency distributions are independent of ambient levels that can vary substantially among different sites and sampling times.

The hourly mass concentrations of PM_1 and PM_{10} for the urban site were obtained from the Purple Air real-time air quality data (*https://www2.purpleair.com/*) from sensors located within 0.5 kilometers of the sampling location (UCI buildings Aldrich Hall for urban samples; the Multipurpose Science and Technology Building for wildfire samples). The mass concentration of $PM_{1–10}$ was obtained by subtracting the mass concentration of PM_1 from PM_{10}. The PM mass concentrations during sampling periods were integrated and used to normalize the data of EPFRs, ROS, and total OP-DTT. Note that particles smaller than 56 nm were not collected, but they only represent a minor fraction of the mass. The Purple Air data were not available at the highway sites.

ROS DETECTION AND QUANTIFICATION

EPR Spectroscopy

Radical forms of ROS (i.e., ·OH, superoxide, R· and RO·) were detected using a continuous wave EPR spectrometer (Bruker) deployed in the lab at UCI. EPR spectroscopy is based on the Zeeman effect, occurring when unpaired electrons are immersed in a magnetic field, which splits the energy levels of the electrons into two or more levels. The electrons with the same direction of the magnetic field have a lower energy than the electrons with the opposite direction. In these conditions, the sample can absorb energy from a microwave radiation. Upon absorption, electrons have enough energy to flip their direction against the magnetic field. The absorption spectrum of a paramagnetic compound is recorded by irradiating the sample with a fixed microwave frequency radiation and sweeping the magnetic field. The absorption takes place when the gap between the energy levels matches the energy of the microwave radiation.

The investigators successfully conducted measurements using X-band microwave frequencies of ~9.8 GHz (Arangio et al. 2016; Tong et al. 2016). EPR spectra were recorded at a room temperature by setting the following typical operating parameters: a modulation frequency of 100 kHz; a microwave frequency of 9.8 GHz; a microwave power of 2.149 mW (20 db); a modulation amplitude of 1.0 G; a sweep width of 110.0 G; a sweep time of 175 seconds; a receiver gain of 40 db; a time constant of 40.96 milliseconds; a conversion time of 160 milliseconds; and a scan number of 6. Paramagnetic species are characterized based on their *g*-factor values. Free electrons have a *g*-factor value of 2.0023 and organic radicals have higher *g*-factor values (2.0030–2.0060), depending on the number of oxygen atoms in the molecule (Dellinger et al. 2007; Pedersen 1985).

EPR can detect and quantify relatively stable radicals, such as ascorbate radicals (Asc·⁻) (Buettner and Jurkiewicz 1993), that may be generated upon electron-transfer reactions of antioxidants and semiquinone radicals contained in naphthalene SOA (McWhinney et al. 2013). EPR can also detect and quantify short-lived reactive radicals by applying a spin-trapping technique. A spin trap is a molecule that reacts preferentially with specific radicals (i.e., ·OH, superoxide, organic radicals etc.). Addition of a spin-trapping agent results in reaction of spin traps with specific short-lived radicals, forming stable radicals that can be directly detected by EPR. In this project, we used ·OH (5-*tert*-butoxycarbonyl-5-methyl-1-pyrroline-N-oxide) (high purity, Enzo Life Sciences GmbH), which are very efficient in trapping for ·OH, $\cdot O_2^-$, and organic radicals (Tong et al. 2016; Zhao et al. 2001).

For quantification and determination of the relative abundance of ·OH, $\cdot O_2^-$, R·, and RO·, EPR spectra were fit and simulated using Xenon and the Matlab-based computational package Easyspin (Stoll and Schweiger 2006). Four types of radicals were used to fit the spectra: BMPO-OH (hyperfine coupling constants of a^N = 14.3 G, a^H_β = 12.7 G, a^H_γ = 0.61 G); BMPO-OOH (a^N = 14.3 G, a^H = 8.1 G); BMPO-R (a^N = 15.2 G, a^H = 21.6 G); and BMPO-OR (a^N = 14.5 G, a^H_β = 16.6 G). The deconvolution of spectra allows us to estimate the relative contribution of four types of ROS.

The spin-counting method embedded in the Bruker software, Xenon, was used to quantify detected radicals. In this method, the absolute amount of free radicals was directly quantified with the spin-counting theory with careful calibration of an EPR resonator. Spin concentrations were calculated using the spin-counting method (Eaton et al. 2010), which we had successfully applied in our previous studies (Arangio et al. 2016; Tong et al. 2016). The detection limit of radicals by EPR is ~1×10^{10} spins μg^{-1} (the number of spins or radicals per µg of particle mass).

Diogenes Chemiluminescence

A Diogenes chemiluminescence assay combined with EPR spectroscopy was applied to quantify cellular and chemical $\cdot O_2^-$ production with and without SOD pretreatments. The Diogenes chemiluminescence assay is suitable for monitoring cellular $\cdot O_2^-$ production kinetics during exposure, as Diogenes is a very sensitive $\cdot O_2^-$ chemiluminescence enhancer that is nondenaturing to living cells (Yamazaki et al. 2011). A Diogenes probe reacts with $\cdot O_2^-$ to emit flash chemiluminescence signal that is proportional to the $\cdot O_2^-$ production rate. The output of the Diogenes chemiluminescence is in relative light units (RLU). To convert RLU to $\cdot O_2^-$ production rates, the Diogenes chemiluminescence assay was calibrated with an EPR spectrometer coupled with a spin-probe technique using the standardized cell-free $\cdot O_2^-$ generation system — the hypoxanthine (HX) and XO system. With the catalysis of XO, HX is oxidized to xanthine, which is then oxidized to uric acid. This oxidation process produces electrons that are passed to O_2 to produce $\cdot O_2^-$ (Fridovich 1970; McCord 1985).

A spin-probe molecule CMH (1-hydroxy-3-methoxycarbonyl-2,2,5,5-tetramethylpyrrolidine) was used to react with $\cdot O_2^-$ to form EPR-detectable nitroxides radical CM· that has a characteristic three-peak EPR spectra (Dikalov et al. 2011). CM· is stable over time and thus it can be used to calculate the $\cdot O_2^-$ production rate. Instrument parameters for EPR spectra acquisition were set to the following: a microwave frequency of 9.652 GHz; a modulation frequency of 100 kHz; a modulation amplitude of 1 G; a center field of 3,520 G; a sweep width of 80 G; a microwave power of 20 mW; a number of scans of 5; and a receiver gain of 30 dB. Concentrations of $\cdot O_2^-$ were obtained by simulating the CM· spectra and counting the total number of spins using the SpinFit and SpinCount modules embedded in the Bruker Xenon software.

The concentration of HX was fixed at 250 µM, and XO was varied in the range of 0–0.6 mU mL^{-1} (U as the enzyme unit in µmol min^{-1}). First, XO and the probe reagent (either 50 µL Diogenes or 15 µL 3 mM CMH) were mixed in incomplete media, yielding negligible chemiluminescence or CM· signal. Next, HX was added to initiate the reaction in a final volume of 200 µL. Chemiluminescence and EPR measurements were then carried out with 1.5 to 7 minutes of reaction. Pretreatments with SOD diminished the signals to the background levels, confirming that the enhanced signals were due to the presence of $\cdot O_2^-$. $\cdot O_2^-$ production rates calculated from the EPR spin-probe method show a linear relationship with RLU from chemiluminescence (R^2 = 0.993). Therefore, the slope from the linear regression was used to convert the Diogenes chemiluminescence data to $\cdot O_2^-$ production rate with units of µM min^{-1}.

For cellular $\cdot O_2^-$ measurements, after cells were cultured in 96-well plates, the media was gently removed and 50 µL of the Diogenes probe made in sterile water was added to each well and incubated for 2 minutes. Then 100 µL of incomplete media (for SOD-pretreated wells, 85 µL of incomplete media and 15 µL 1,250 U mL^{-1} SOD in PBS buffer were added instead) and 50 µL of sample were added to start the exposure. For inhibitor experiments, 10 µL of the inhibitor (roughly 100 µM apocynin) was added before sample exposure. To prevent cross-well interferences, black sealing films (AbsorbMax, EXCEL Scientific, Inc.) were used to seal the bottom of the plates. Continuous luminescence measurements were conducted using the plate reader every 3 minutes for 4 hours to obtain the $\cdot O_2^-$ production rate. The total $\cdot O_2^-$ production was obtained by integrating the area under the curve from the kinetic of $\cdot O_2^-$ release as a function of exposure time. Incomplete media and filter blanks were used as vehicle controls for 9,10-phenanthrenequinone (PQN) and SOA, respectively. The $\cdot O_2^-$ production rate and total production from exposure to samples were corrected by subtracting those from controls. Cell-free wells were also used as *acellular controls* to capture any background signals, which were subtracted from the data with cells when necessary.

For quality control, we used PQN as the positive control and calibration using CMH to check the linearity of EPR deter-

mination of the CMH concentration. One well of DMEM cell culture media, one well of deinonized water, and one filter blank with and without SOD pretreatment were run in each experiment. The measurements of chemical $\cdot O_2^-$ production followed the same protocol as cellular $\cdot O_2^-$ measurements, except cells were absent and the reaction time started when PQN or isoprene-derived SOA particles were dissolved or extracted in incomplete media (pH 7.4). Accounting for the time it took to prepare samples, chemical $\cdot O_2^-$ measurements usually started at 15 minutes. As this delay may miss a significant portion of the generated ROS, kinetic modeling was applied to account for ROS generation in earlier times.

Statistical Analyses For Diogenes chemiluminescence data, for each dose, triplicate measurements were performed on a 96-well plate on the same experimental day along with vehicle and acellular controls that were used to correct experimental data. For every experiment, we included a positive control (either 1.74 μg mL^{-1} PQN or 1 μM phorbol 12-myristate 13-acetate [PMA]), vehicle control (incomplete media for PQN and filter blank for isoprene SOA), and acellular control (without the presence of cells). Experiments with some different doses were done on different days. One-way ANOVA followed by the Tukey post-hoc test on the total superoxide production from the same dose of PQN (1.74 μg mL^{-1}), performed on different days, show that no significant differences were determined between the means of data ($P > 0.1$). The time profile of superoxide production and total production are presented as the mean of the triplicate measurements, with error bars representing the uncertainties propagated from the standard deviations of triplicate measurements of samples and controls. For imaging, all data points for each sample were averaged from multiple cells ($N > 10$). Results were analyzed by using unpaired student *t* tests. The results were considered statistically significant at $P \leq 0.05$ for all exposure groups compared with control groups.

Fluorometric H_2O_2 Assay

A modified protocol (Wei et al. 2019) was applied for the H_2O_2 measurement using a fluorometric H_2O_2 assay kit (MAK165, Sigma-Aldrich). 250 L DMSO and 1 mL assay buffer were added to the red peroxidase substrate and horseradish peroxidase for reconstitution, respectively. The reagents were divided into ten sets of aliquots (25 L red peroxidase substrate, 100 L horseradish peroxidase, and 2 mL assay buffer each). Prior to each analysis, one set of reagents was used to prepare 2 mL working solutions, consisting of 20 L red peroxidase substrate, 80 L horseradish peroxidase, and 1.9 mL assay buffer. All H_2O_2 measurements were conducted within 2 hours of the preparation of working solutions, due to the high instability of the probe. A calibration was performed using H_2O_2 standards concentrations ranging from 0.05–1.5 M, which were prepared by diluting 30 wt% H_2O_2 (Sigma-Aldrich). The reaction vials (3 mL) consisted of 2.94 mL solution (Milli-Q water + filter extracts) and 60 L working solution. The H_2O_2 yields from different SOA samples varied significantly, and dilution factors were adjusted so that the final H_2O_2 concentrations in the reaction vial were below 1.5 M. All H_2O_2 measurements were conducted with a filter blank that used the same dilution factor as the samples. The addition of working solution was considered to be the start of the reaction, and the reaction vials were incubated at room temperature for 15 minutes until the measurement. The fluorescence of the reagents was measured by a spectrofluorophotometer (RF-6000, Shimadzu) at excitation and emission wavelengths of 540 and 590 nm, respectively.

Oxidative Potential by the DTT Assay

Two circular punches from each filter sample were extracted in 7 mL of Millipore water for 8–10 minutes using the vortex mixer. The DTT assay was conducted on the extracts and the filter using the DTT protocol of Gao and colleagues (2017). The measured total DTT activities include the contributions from both the water-soluble and water-insoluble fractions. In brief, 7 mL of the extracts and the filter were incubated at 37°C with 2 mL potassium phosphate buffer and 1 mL DTT (1 mM) and were shaken continuously in a ThermoMixer (Eppendorf North America, Inc.). At specified time points (5, 10, 15, 20, 25 min), a small aliquot (100 μL) of the incubated mixture was withdrawn and mixed with 1 mL trichloroacetic acid to quench the consumption of DTT. The quenched mixture was further mixed with 2 mL Tris buffer (0.08 M with 4 mM EDTA [ethylenediaminetetraacetate]) and 0.5 mL of DTNB (0.2 mM, 5,5'-dithiobis-(2-nitrobenzoic acid)). 1 mL of this mixture was diluted with 9.5 mL of water and filtered using a 0.22 μm pore syringe filter (Millex). The filtered solution was immediately measured for absorbance at 412 nm and 700 nm wavelength using the Liquid Waveguide Capillary Cell with an optical path length of 100 cm (World Precision Instruments, Inc.) coupled to the ultraviolet-visible spectrophotometer (DH-MINI, Ocean Optics, Inc.) and the multiwavelength light detector (FLAME-T-UV-VIS-ES, Ocean Optics, Inc.). The total DTT activities were calculated from the linear regression of absorbance versus time and presented as the total DTT activities per volume of air (total DTTv, pmol min^{-1} m^{-3}) and per mass of $PM_{2.5}$ (total DTTm, pmol min^{-1} μg^{-1}) (Fang et al. 2015). For quality control, we used PQN as the positive control. A 5 mM solution of PQN is made in DMSO, which is then serially diluted to a final concentration of 40.8 ng/mL in deionized water. The standard is used in the same amount as the sample (0.7 mL). The OP value must have a coefficient of variation less than 15%; otherwise, the experiment was repeated.

CELL CULTURE AND EXPOSURE

Cell Culture

We chose RAW 264.7 macrophages, as they are a widely applied and established macrophage cell line for studying the oxidative stress responses of macrophages (Forman and Torres 2002; Franzi et al. 2011; He et al. 2017; Hiura et al. 1999; Li et al. 2003). Macrophage cells (ATCC TIB-71) were obtained and passaged in complete media (DMEM media supplemented with 10% FBS and 1% antimycotic/ampicillin) until >80% confluent. Cells were then seeded at a density of 4×10^4 cells/mL with 200 µL per well into 96-well plates (Corning) and incubated at 37°C and 5% CO_2 in an incubator for about 2 hours for cells to fully adhere to the bottom of the culture plate.

Cytotoxicity

Cell cytotoxicity was measured using the CellTox Green Cytotoxicity Assay, which measures the changes in membrane integrity that may occur as a result of cell death. In brief, after cells were cultured in 96-well plates, complete media was replaced by 100 µL incomplete media and 50 µL CellTox Green reagent for each well. The CellTox Green reagent was made according to the package directions. To facilitate the dye binding to DNA, cells were incubated in dark for at least 15 minutes before 50 µL of each sample was added to initiate exposure. Fluorescence signals were then measured with a Microplate Reader (Promega, GloMax) for 4 hours with excitation and emission wavelengths of 475 nm and 525 nm, respectively. The fluorescence signals were given as RLUs.

FLUORESCENCE LIFETIME IMAGING

Phasor Approach to FLIM

The Phasor-FLIM imaging technique was applied with NADPH oxidase activator, PMA, and inhibitor, apocynin, to study the NADPH oxidase activities as a potential mechanism of cellular $\cdot O_2^-$ release. The Phasor-FLIM has been previously used to study cellular metabolism in great details (Digman et al. 2008; Ranjit et al. 2019; Stringari et al. 2012; Weber 1981). FLIM measures the time a fluorophore spends during an excited state before emitting a photon and returning to the ground state, which can vary from picoseconds to hundreds of nanoseconds. Lifetime measurements take advantage of absolute measurements that are independent of probe concentration, absorption, or luminescence intensity. Furthermore, the phasor approach has a robust computation analysis and provides an additional dimension to fluorescence data mapping. The phasor approach takes in fluorescence decay intensity from FLIM and Fourier-transforms either the multi- or mono-exponential lifetime into phasor plots on a g-s coordinate.

The NADPH oxidase complex is an important source of $\cdot O_2^-$ in phagocytosis as activated by bacterial products and cytokines (Bedard and Krause 2007). It should be noted that NADH (nicotinamide adenine dinucleotide) has identical fluorescence properties with NADPH (Rehman et al. 2017); thus FLIM cannot differentiate NADH and NADPH, and we denote the FLIM signals as NAD(P)H. Note that NADH reacts with O_2 to produce either water or H_2O_2 (Yang and Ma 2007), or produces significantly lower $\cdot O_2^-$ than NADPH (Li and Shah 2001). Combining with the experiments conducted using NADPH oxidase activator PMA (Nguyen et al. 2017) and inhibitor apocynin (El-Sawalhi and Ahmed 2014), we were able to use the Phasor-FLIM method to study the NADPH oxidase activities. NAD(P)H expresses in two forms inside cells, bound and free states. Each state has its own fluorescence lifetime after laser excitation, reflecting differences in structure. Binding to proteins or enzymes causes the NAD(P)H structure to extend, disrupting the π-π interaction and increasing the fluorescence lifetime. Since the oxidized $NAD(P)^+$ does not emit auto-fluorescence, in contrast to NAD(P)H, the conversion of NAD(P)H to $NAD(P)^+$ will reduce the fraction of bound NAD(P)H and cause a shift from the bound to the free end of the NAD(P)H free-bound trajectory (Pate et al. 2014; Stringari et al. 2011). The benefits of this method are multifold; it shows cell morphology, indicates the localization of NADPH oxidase activities, and provides time-dependent cellular responses without the addition of labeling probes that may interfere with samples or cellular responses from samples.

For FLIM imaging, RAW 264.7 macrophage cells were seeded at a density of 4×10^4 cells mL^{-1} and incubated overnight before exposure to PQN and isoprene-derived SOA for imaging. PQN and SOA in media in the absence of cells produced low fluorescence background signals. Cells were imaged at 37°C and 5% CO_2 environment before exposure and at different time points after the addition of samples. FLIM images were acquired with a Zeiss LSM710 META laser scanning microscope coupled to a 2-photon Ti:Saphirre laser (Mai Tai, Spectra Physics, Newport Beach, CA) for excitation at 740 nm using a 40× water-immersion objective (1.2 NA; Zeiss), and a photomultiplier tube (H7422P-40; Hamamatsu) for detection. An ISS A320 FastFLIM box was used to collect the fluorescence decay, and data were Fourier transformed into g and s coordinates using the SimFCS software (Globals Software·G–SOFT LLC., Irvine UCI–CA) in the phasor approach. 20 frames of images were collected for each time point. The bound NAD(P)H fraction of each macrophage cell can be obtained according to its relative location on the phasor plot. Because NAD(P)H mainly resides in cell membranes and cytoplasm (Panday et al. 2015) and that the fluorescence lifetimes of nuclei do not change significantly before and after sample exposure, the nuclei were cropped out, that is, only the fluorescence signals from the cell membranes and cytoplasm were included in calculating the bound NAD(P)H fractions. The bound NAD(P)H fractions from all data points for each sample were averaged from multiple cells (N = 12–23). PQN exhibited an unusually long lifetime distribution and relatively higher photon counts compared with other samples (over maximum 1 µs) in that the phasors from PQN fell outside of the NAD(P)H free-bound trajectory,

while those from the nuclei remained on the trajectory. This abnormal long lifetime was likely caused by the delayed emission of phosphorescence from triplets of PQN (Togashi and Nicodem 2004). The phosphorescence lifetime of aromatic ketones in a triplet state is known to be in the range of milliseconds for transitions forbidden by structure symmetry in the condition of low oxygen quenching. We verified the emission of phosphorescence from PQN using hyperspectral imaging. Before exposure, the cells' emission spectra exhibited a peak within a wavelength range of 450–525 nm, which is consistent with NAD(P)H emission wavelengths. After the same cells were exposed to PQN for 30 minutes, we observed significant increases in the intensity below 450 nm, likely due to the emission of phosphorescence from PQN. To avoid the lifetime of phosphorescence interfering with the NAD(P)H fluorescence lifetime, we used PBS buffer to wash cells after 10 minutes of incubation. After replacing with fresh incomplete media, cells were loaded back to the FLIM system for imaging. With this method, the lifetime phasors of PQN fell onto the NAD(P)H free-bound trajectory.

FLIM-Laurdan

The FLIM-Laurdan imaging technique was used to study the effect of $\cdot O_2^-$ on cell membrane fluidity as a result of lipid peroxidation (Golfetto et al. 2013). Laurdan (6-dodecanoyl-2-dimethylaminonaphthalene) is a fluorescent membrane marker used to investigate membrane fluidity. This solvatochromic probe has the ability to attach in different depths and orientation of lipid bilayers and shift its spectral emission maximum upon hydrophobic environmental change. When Laurdan is in a hydrophobic environment, it has two excited states, the locally excited state, which is intrinsic to the fluorophore, and an internal charge transfer state created by a larger dipole moment. This polar relaxation causes water molecules in more hydrophilic environments to reorient to the same orientation of Laurdan's dipole that causes energy loss. According to former works done by the Laboratory of Fluorescence Dynamics, Laurdan lifetime in the blue channel decreases when the probe is in a more hydrophobic environment (Golfetto et al. 2013). Therefore, shorter Laurdan fluorescence lifetimes correspond to increases in membrane fluidity due to lipid peroxidation. We measured the difference of Laurdan lifetime, which does not require the need of fluorescence intensity. Lifetime imaging is a relatively more stable approach since it is independent of dye concentration and also provides local changes upon the cell membrane. The dipolar relaxation effect of Laurdan is found to cause quenching of lifetime in both blue and green channels, only that the green channel does not shift along the phasor plot universal circle. Hence, we used a 460/80 nm cubical filter to collect only blue emission spectra and project phasor points onto the universal circle to acquire absolute lifetime values. After seeding cells in an 8-well plate, complete media was replaced with incomplete media, and Laurdan dye was added to each well to achieve a final concentration of 5 μM 30 minutes before exposure to control, PQN, PMA, and isoprene-derived SOA. After some period of exposure, the 8-well plate was loaded to the FLIM system for imaging at 800 nm.

Third Harmonic Generation Imaging

The third harmonic generation (THG) imaging technique was applied to detect the accumulation of lipids inside the cells after exposure to PQN (Dvornikov et al. 2019). The excitation of the THG signal requires laser wavelengths of up to ~1,000 nm, which conventional tunable titanium sapphire lasers could not achieve. The THG imaging was carried out in the deep imaging via emission recovery system from the Laboratory of Fluorescence Dynamics, which uses Spectra Physics Insight DS+ femtosecond laser tunable in the range of 68–1,300 nm. The actual focal depth difference was found to be ~0.75 mm for a different wavelength excitation, where NAD(P)H is 740 nm and THG is 1,050 nm. The THG signal is generated at the interface between media with differences in third order nonlinear susceptibility, refractive index, and dispersion, and can be used to detect lipids. Note that THG microscopy is not affected by long lifetime phosphorescence from PQN.

KINETIC MODELING

Aqueous Kinetic Model

A kinetic model was developed for an aqueous environment and applied to simulate the simultaneous formation of ·OH and the superoxide family ($\cdot O_2^-/HO_2\cdot$), that is, the superoxide radical and its conjugated acid ($HO_2\cdot$), by aqueous reactions of SOA. The reactions include chemical reactions of SOA components, ROS coupling reactions, and radical-trapping reactions by BMPO. SOA chemistry includes decomposition of ROOH, which generates ·OH radicals (Tong et al. 2016, 2018), ·OH oxidation of primary and secondary alcohols (R_1R_2CHOH) and a subsequent reaction with O_2 to form α-hydroxyperoxyl radicals ($R_1R_2C(O_2)OH\cdot$), decomposition of $R_1R_2C(O_2)OH\cdot$ to generate hydroperoxyl radical ($HO_2\cdot$) (Bothe et al. 1978; Herrmann et al. 2005), ·OH oxidation of ROOH (Herrmann et al. 2005), $R_1R_2C(O_2)OH\cdot$ and other SOA components, and $HO_2\cdot$ termination of $R_1R_2C(O_2)OH\cdot$. Rate coefficients of decomposition of ROOH and $R_1R_2C(O_2)OH\cdot$, as well as H-abstraction of R_1R_2CHOH, were assumed to be independent of the structures of R groups (R_1 and R_2) contained among different SOA, representing a major model assumption. This assumption is in line with the CAPRAM 3.0 model (Herrmann et al. 2005), in which the rate constants of H-abstraction on alcohols vary within one order of magnitude regardless of carbon numbers and functionalities besides the hydroxy group. The radical composition profiles generated by different SOA are solely determined by the relative abundance of ROOH and R_1R_2CHOH groups in SOA. Potential variation of these rate constants depending on R structures can be partly translated into uncertainties in molar fractions of ROOH and R_1R_2CHOH. The rate coefficients of ROS coupling reactions were obtained from literature values and the unknown rate coefficients, and molar fractions of ROOH and R_1R_2CHOH

contained in SOA were determined using the Monte Carlo genetic algorithm (MCGA) to reproduce experimental data (Berkemeier et al. 2017).

A kinetic model was also applied to simulate the radical formation by aqueous reactions of isoprene SOA with Fe^{2+} in surrogate lung fluid (SLF) containing antioxidants (see Wei et al. 2021a for details). The reactions include radical chemistry involving SOA, ROS coupling, reactions of Fe ions, reactions involving antioxidants, and BMPO chemistry. The mechanisms of ·OH and $\cdot O_2^-/HO_2\cdot$ formation from SOA were explicitly addressed in our previous study (Wei et al. 2021b) with the addition of Fe^{2+}-catalyzed ROOH decomposition (Goldstein and Meyerstein 1999; Tong et al. 2016). The RO· formation originates from Fe^{2+}-catalyzed decomposition of organic peroxides (ROOR) and ROOH, which can be further converted to R· through isomerization (Gilbert et al. 1976), decomposition (Erben-Russ et al. 1987), and bimolecular reactions (Carrasquillo et al. 2015). Note that the rate coefficients involving SOA chemistry were assumed to be independent of the structures of R groups contained in isoprene SOA, representing a major model assumption. The rate coefficients of ROS coupling reactions were obtained from literature values. For Fe–oxidant interaction, we also consider potential impacts of Fe–citrate ligand on the rate coefficients as demonstrated by Gonzalez and colleagues (2017). The rate coefficients of antioxidants with radicals and Fe ions were also adopted from literature, except that the scavenging of R· and RO· by ascorbate was assumed to be a few orders of magnitude slower than that of ·OH and $\cdot O_2^-/HO_2\cdot$. This is in line with the experimental results showing BMPO-OH and BMPO-OOH below the detection limit, in contrast to the significant formation of BMPO-R and BMPO-OR. The redox cycling of Fe^{3+}/Fe^{2+} by ascorbate is also considered. The unknown rate coefficients and molar fractions of ROOH, R_1R_2CHOH, and ROOR contained in isoprene SOA were determined using the MCGA to reproduce experimental data (Berkemeier et al. 2017). In the Monte Carlo search, input parameters were varied randomly within individual bounds: the boundaries of all reaction rate constants were generally constrained to within two or three orders of magnitude based on literature values. The uncertainties of the rate coefficients were obtained by running the MCGA numerous times (>100), among which 40 parameter sets were selected that reasonably captured the temporal trends of the experimental data.

KM-SUB-ELF Model

KM-SUB-ELF treats mass transport and chemical reactions involving ROS, antioxidants, surfactants and redox-active components contained in PM (Lakey et al. 2016). The model contains over 50 reactions including Fenton and Fenton-like chemistry, redox cycling of quinones, Fe and Cu, and radical–radical reactions. Rate coefficients were set to literature values when available and unknown or uncertain rate coefficients had previously been optimized to reproduce measurements of H_2O_2 and ·OH production by quinones, Fe, and Cu in surrogate ELF, which also showed that other transition metals such as Mn, Co, V, Ni, Zn, Cd, and Cr do not induce significant ROS formation (Charrier and Anastasio 2011; Charrier et al. 2014). The model considers ROS formation by SOA derived from α- and β-pinene, isoprene, limonene, and ROS by quinones from naphthalene. Experimental studies showed that naphthalene SOA produce mainly H_2O_2 and $\cdot O_2^-$, while α- and β-pinene, isoprene, and limonene SOA produce mainly ·OH and organic radicals via the decomposition of ROOH, which can be enhanced in the presence of iron ions via Fenton-like reactions (Tong et al. 2016, 2018). Organic hydroperoxides generated by multigenerational oxidation and autoxidation account for a substantial fraction of SOA (Docherty et al. 2005; Ehn et al. 2014). The ROS molar yields of SOA are based on those from α- and β-pinene, isoprene, and limonene SOA (Tong et al. 2016). The model includes a H_2O_2 formation rate of 1.5×10^9 s^{-1} per μg of SOA, which is based on a 0.06% mass yield of H_2O_2 from terpene SOA at pH 7.5 (Lakey et al. 2016; Wang et al. 2011b) and a total ·OH molar yield of 0.1% from SOA (Tong et al. 2016).

For the modeling study, ambient concentrations of the different chemical species were used as inputs to a lung deposition model, which predicts concentrations of chemical species and OP in the ELF in different compartments of the human respiratory tract (ICRP 1994). Fang and colleagues (2017a) collected size-segregated ambient particles with aerodynamic diameters of 0.056–18 μm on filters at road-side and urban sites in Atlanta, GA, in spring 2016. They measured PM OP and chemical composition including organic carbon, brown carbon, and water-soluble metals. As quinones and SOA measurement were not available for these samples, their ambient concentrations were estimated from the organic carbon ambient concentration using conversion factors based on previous studies at the same urban site and during the same seasons (Verma et al. 2015b). In addition, they measured PM OP for water-soluble extracts of all samples by the DTT and ascorbic acid assays (OP^{DTT} and OP^{AA}) (Fang et al. 2017b). To evaluate contributions of HULIS to ROS formation in this study, we estimated HULIS concentrations in the $PM_{2.5}$ samples based on brown carbon measured by absorbance at the 365 nm wavelength with an UV-VIS spectrometer.

We modeled respiratory deposition for a person doing light work, assuming unit density spherical particles and nose-only steady breathing with a flow rate of 1.5 m^3 hr^{-1}, a respiration frequency of 20 min^{-1}, and a tidal volume of 1,250 cm^3. Deposition efficiencies in different compartments of the extrathoracic, bronchial, and alveolar regions can be found in a previous study (Fang et al. 2017b). Concentrations of water-soluble Fe and Cu, SOA, and quinones deposited in the ELF for different compartments were calculated using the following two equations: (Lakey et al. 2016)

$$C_{i,j}^{ELF,k} = \frac{C_i^a \cdot DE_j^k \cdot F \cdot t \cdot N_A}{MW_i \cdot A^k \cdot D^k} \quad (1)$$

$$C_i^{ELF,k} = \sum_{j=1}^{10} C_{i,j}^{ELF,k} \quad (2)$$

where $C_{i,j}^{ELF,k}$ is the concentration of species i (molecules cm^{-3}) in particle size bin j that deposited in the ELF in respiratory compartment k; C_i^a is the ambient concentration (g m^{-3}) of chemical species i; DE_j^k is the deposition efficiency; F is the breathing flow rate of 1.5 m^3 hr^{-1} and t is the accumulation time of 1.5 hours (accumulation time chosen based on the range of time for particles to be removed by the immune system and metabolic activities [Ghio et al. 1998, 2006]); N_A is the Avogadro number; MW_i is the molecular weight of the species i (MW for ROS-generating quinones is 183.18 g mol^{-1}, obtained by taking the average value of the MW of phenanthrenequinone, 1,2-naphthoquinone, and 1,4-naphthoquinone; MW_{SOA} is assumed to be 200 g mol^{-1}); and A^k and D^k are the ELF surface areas (cm^2) and thickness (cm) in compartment k, respectively. $C_{i,j}^{ELF,k}$ is then summed up for all size ranges to obtain the total concentration of species i in the ELF in compartment k, denoted as $C_i^{ELF,k}$.

For the $PM_{2.5}$ sample, an average deposition efficiency of 0.384 and an ELF volume of 16.7 mL were used. OP measurements were inputted into the same equations (equations 1 and 2) to calculate the OP in the ELF, except that the Avogadro number and MW were excluded from the equations.

ELF concentrations of water-soluble Fe and Cu, SOA, and quinones were inputted into the KM-SUB-ELF model to predict the concentrations and production rates of ROS in different ELF regions for the size-segregated samples and in the whole tract for $PM_{2.5}$ samples. ROS obtained from the model include ·OH, H_2O_2, and the $\cdot O_2^-$ family. We also applied KM-SUB-ELF to quantify the effects of $PM_{2.5}$, O_3, and NO_2 on ROS formation, interconversion, and reactivity, and discuss different chemical metrics for oxidative stress, such as cumulative production of ROS and H_2O_2 to ·OH conversion (Lelieveld et al. 2021).

RESULTS

ROS FORMATION FROM AQUEOUS REACTIONS OF SOA

Superoxide Formation from SOA

Biogenic SOA were generated by both dark ozonolysis and ·OH photooxidation (SOA_{O3} and SOA_{OH}) of isoprene, β-pinene, α-terpineol, and d-limonene. Particle water extracts were analyzed with EPR spectroscopy coupled with a spin-trapping technique for detection of free radicals. The observed spectra were simulated and deconvoluted into spectra for different BMPO adducts with radicals including ·OH, $\cdot O_2^-/HO_2\cdot$, R·, and RO· (BMPO-OH, BMPO-OOH, BMPO-R, and BMPO-OR, respectively). Note that BMPO-OOH is generated by the trapping of either $\cdot O_2^-$ or $HO_2\cdot$. Integration of deconvoluted spectra allows us to quantify contributions from each radical species. **Figure 3** shows quantifications of different types of radicals in water extracts of SOA generated by ozonolysis or ·OH oxidation of isoprene, β-pinene, α-terpineol, and d-limonene. Relative yields of BMPO-OH of isoprene and β-pinene SOA_{O3} after 20 min of reactions are 44% and 52%, respectively, both of which further increased to >70% after 2 hours. This is in very good agreement with a previous study that demonstrated major ·OH formation from biogenic SOA formed by ozonolysis (Tong et al. 2018). α-terpineol SOA_{O3} generates ·OH exclusively, while d-limonene SOA_{O3} generates $\cdot O_2^-/HO_2\cdot$ dominantly (80%) with minor contributions from ·OH (11%) and organic radicals (7%). In contrast to major ·OH formation by most of SOA_{O3}, more than 80% of radical species generated from SOA_{OH} are in the form of $\cdot O_2^-/HO_2\cdot$. All types of SOA_{OH} are found to have a similar $\cdot O_2^-/HO_2\cdot$ formation efficiency (molar concentration ratios of BMPO-radical adduct to SOA) of 0.018%–0.03%.

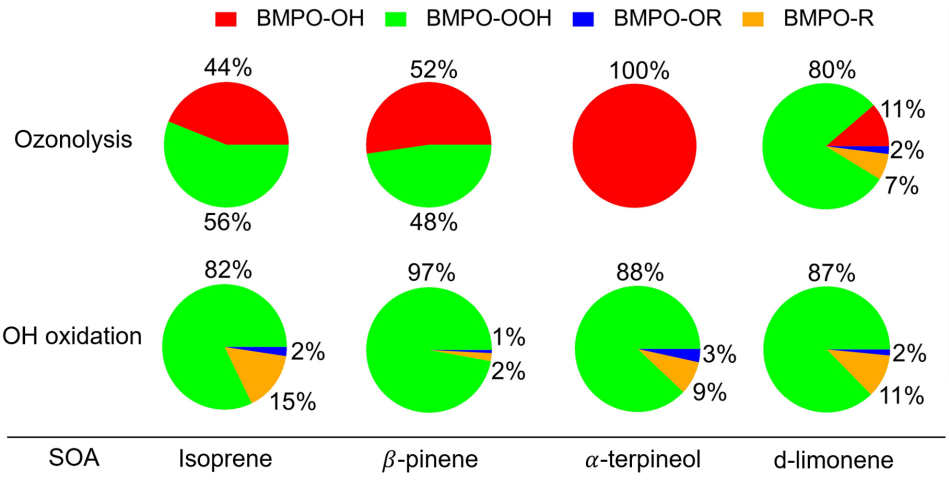

Figure 3. Relative yields of BMPO-radical adduct from aqueous reactions of SOA generated by dark ozonolysis (SOA_{O3}) versus ·OH photooxidation (SOA_{OH}) of isoprene, β-pinene, α-terpineol, and d-limonene. Reprinted with permission from Wei et al. 2021b. Copyright 2021 American Chemical Society.

The molar yields of H_2O_2 from SOA were also quantified using a fluorometric H_2O_2 assay. Isoprene SOA generally yields higher H_2O_2 compared with other types of SOA. The H_2O_2 yield from β-pinene SOA_{O3} (1.8% ± 0.3%) is comparable with results of Wang and colleagues (2011b), 1.3% ± 0.9%, but around half of the amount reported by Tong and colleagues (2018), (3.2% ± 0.7%). Isoprene SOA_{O3} generally produces higher H_2O_2 (4.2% ± 0.7%) compared with β-pinene SOA_{O3} (1.8% ± 0.3%), which is comparable with Tong and colleagues (2018), (8.0% ± 0.8% for isoprene SOA_{O3} and 3.2% ± 0.7% for β-pinene SOA_{O3}). For both oxidation systems with various precursors, the production of $\cdot O_2^-/HO_2\cdot$ is tightly correlated with H_2O_2 formation, with R^2 greater than 0.9, indicating that $\cdot O_2^-$ is an important precursor of H_2O_2, or that $\cdot O_2^-$ and H_2O_2 have similar types of source compounds. For β-pinene, α-terpineol, and d-limonene SOA, the H_2O_2 yields from SOA_{O3} are about one order of magnitude higher than those from SOA_{OH}. This is consistent with the reaction mechanism of ozonolysis, in which stabilized Criegee intermediates hydrolyze to form α-hydroxyhydroperoxides that can readily decompose into carbonyls and H_2O_2 (Hasson et al. 2001; Qiu et al. 2020a; Wang et al. 2011b). The distinct profiles of ROS composition by SOA_{O3} and SOA_{OH} reflect differences in chemical compositions and functionalities caused by different oxidation pathways. Monoterpene SOA from ozonolysis generally contains higher fractions of ROOR (12%–65%) compared with those from photooxidation (6%–18%) (Docherty et al. 2005; Mertes et al. 2012), partly because ROOH are decomposed with prolonged UV exposure (Badali et al. 2015; Epstein et al. 2014). As ROOH can be a primary source of ·OH radicals through decomposition (Tong et al. 2016, 2018), lower ROOH fractions should lead to minor contributions of ·OH formation for SOA_{OH}.

Reaction Mechanism The temporal evolution of ·OH and $\cdot O_2^-/HO_2\cdot$ formation from the aqueous reactions of SOA was measured. As shown in **Figure 4A**, the molar yields of BMPO-OH adducts from SOA_{O3} increase over time to reach a steady state after approximately 2 hours. In contrast, the molar yields of BMPO-OOH adducts from SOA_{O3} (except α-terpineol SOA_{O3}, which was below the detection limit) reach their maximum concentrations within a short period of time (<30 min), followed by a slight decrease (Figure 4B). For SOA_{OH}, $\cdot O_2^-/HO_2\cdot$ yields reach their maximum within 40 minutes but decrease gradually over 4 hours (Figure 4C). The BMPO-OH concentrations from all SOA_{OH} are below the detection limit. The highly distinct time-dependent profiles

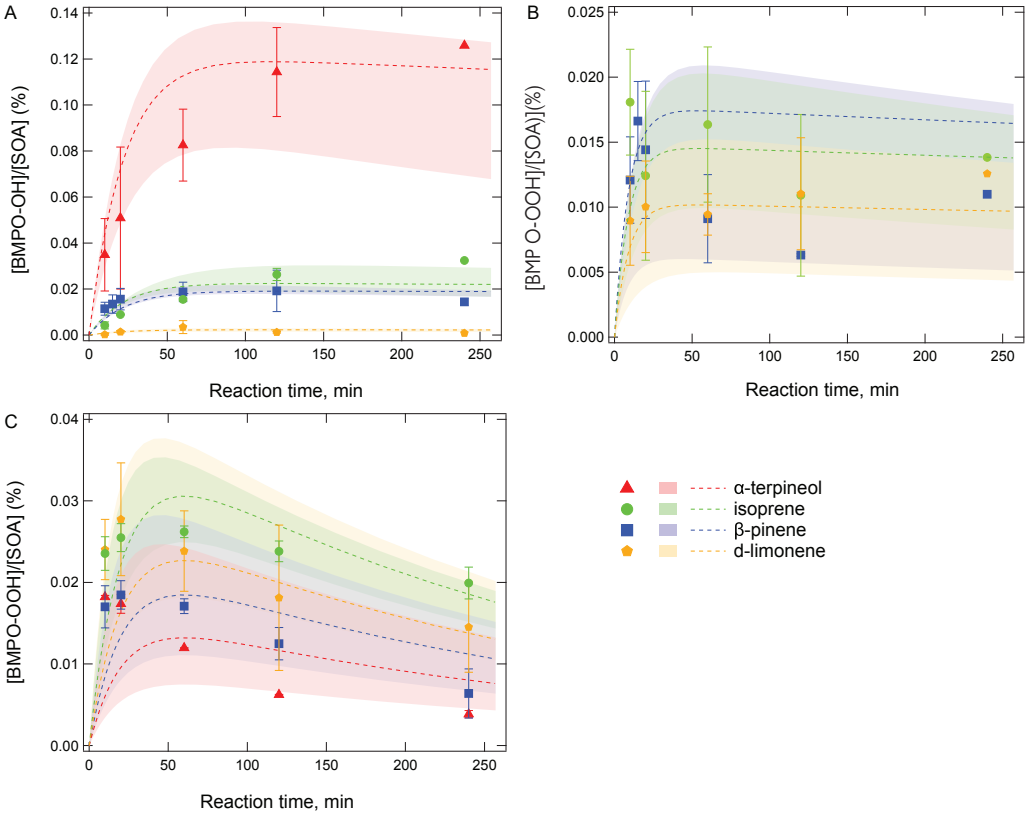

Figure 4. Temporal evolution of molar yields of A. BMPO-OH and B. BMPO-OOH adducts from aqueous reactions of SOA generated from dark ozonolysis (SOA_{O3}), and C. BMPO-OOH adducts from SOA generated from ·OH photooxidation (SOA_{OH}) of α-terpineol), isoprene, β-pinene, and d-limonene. The markers and error bars are experimental data with one standard deviation. The dashed lines represent the best fits of kinetic model with the shaded area denoting the modeling uncertainties. The $\cdot O_2^-/HO_2\cdot$ formation from α-terpineol SOA_{O3} and ·OH formation from all SOA_{OH} are below detection limits. Reprinted with permission from Wei et al. 2021b. Copyright 2021 American Chemical Society.

of ·OH and $\cdot O_2^-/HO_2\cdot$ formation leads to an interesting evolution of radical composition by SOA. For example, radical production from isoprene and β-pinene SOA_{O3} is initially dominated by $\cdot O_2^-/HO_2\cdot$, while ·OH becomes dominant after 20 min. In comparison, d-limonene SOA_{O3} and all types of SOA_{OH} are consistently dominated by $\cdot O_2^-/HO_2\cdot$ (>70%) over 4 hours.

To further elaborate on the reaction kinetics and mechanism, a kinetic model was developed and applied to simulate the temporal evolution of ·OH and $\cdot O_2^-/HO_2\cdot$ radicals. The following reactions were implemented into the kinetic model for ·OH and $\cdot O_2^-/HO_2\cdot$ formation:

$$\text{R1: ROOH} \rightarrow \text{RO}\cdot + \cdot\text{OH}$$

$$\text{R2: } R_1R_2CHOH + \cdot OH \xrightarrow{O_2} c_1\, R_1R_2C(O_2)OH\cdot$$

$$\text{R3: } R_1R_2C(O_2)OH\cdot \rightarrow R_1C(O)R_2 + HO_2\cdot$$

·OH can be generated from the first-order decay of ROOH (R1) (Chen et al. 2011a; Tong et al. 2016, 2018). Krapf and colleagues (2016) provided molecular evidence of the unimolecular decomposition of labile hydroperoxides in the condensed phase through the cleavage of the weaker O-O bond, which must lead to ·OH formation. In addition, direct ·OH formation has been observed from the decomposition of cumene hydroperoxide (Tong et al. 2016) (a common proxy of atmospheric ROOH) at room temperature, and a recent study (Tilgner and Herrmann 2018) demonstrated that the implementation of R1 in the aqueous chemistry model CAPRAM would account for an important source of aqueous ·OH formation from HOM. Note that ·OH formation in R1 results from the decomposition of ROOH without additional functionalities on the α-carbon, as the decomposition of α-hydroxyhydroperoxides leads to the formation of carbonyl and H_2O_2 instead of to ·OH (Qiu et al. 2020a). The generated ·OH can abstract a hydrogen atom from α-carbon of primary or secondary alcohols to form α-hydroxyalkyl radicals ($R_1R_2C(OH)\cdot$) with a yield of c_1, which immediately combine with dissolved to form α-hydroxyperoxyl radicals ($R_1R_2C(O_2)OH\cdot$) (R2). These radicals can subsequently undergo unimolecular decomposition to form $HO_2\cdot$ (R3) (Bothe et al. 1978; Herrmann et al. 2005).

The kinetic model also considers a number of other reactions including ·OH loss via reactions with SOA components, ROS coupling reactions, radical trapping by BMPO, and decay of BMPO-radical adducts. Molar fractions of ROOH and R_1R_2CHOH contained in SOA were estimated using the MCGA to reproduce experimental data (Berkemeier et al. 2017). The decomposition rate of ROOH estimated in this study ($[0.9 – 6.5] \times 10^{-5}$ s^{-1}) is in agreement with previous studies (Tong et al. 2016, 2017), and the lifetime of α-hydroxyperoxyl radicals (0.002–0.06 s) is also consistent with the aqueous chemistry model CAPRAM 3.0 (Herrmann et al. 2005). As shown in Figure 4, the modeling results show good agreement with measurements within modeling uncertainties, indicating that the above reaction mechanisms are plausible for ·OH and $\cdot O_2^-/HO_2\cdot$ formation as they can explain the temporal evolution of distinct radical profiles depending on precursors and oxidation pathways.

The model-estimated molar fractions of ROOH in isoprene, β-pinene, and d-limonene SOA_{O3} are 6%–25%, 7%–35%, and 2%–12%, respectively. These estimated ranges are reflected in uncertainties of model predictions, as indicated by the shaded areas in Figure 4. These estimated values are comparable with the peroxide mass fractions reported by previous studies for the same types of SOA (~30%, ~85%, ~2%, respectively) (Bateman et al. 2011; Docherty et al. 2005; Nguyen et al. 2010; Shiraiwa et al. 2017), assuming that the molar masses of peroxides and SOA components are the same. Note that the measured total peroxide contents include both ROOR and ROOH, which may explain the lower estimated fraction of ROOH in isoprene and β-pinene compared with values found in the literature. In addition, it may imply that some ROOH may be more stable and do not decompose within the timescale of the experiment, as has been observed for isoprene hydroxyl hydroperoxide in a recent study (Fang et al. 2020). Significantly higher fractions of ROOH are estimated in isoprene and β-pinene SOA_{O3}, compared with their corresponding SOA_{OH} (3%–5% and 1%–3%), leading to the major contribution of ·OH formation in SOA_{O3}. The molar fractions of $R_1R_2CH(OH)$ in d-limonene SOA are estimated to be higher compared with ROOH, contributing to the $\cdot O_2^-/HO_2\cdot$ -dominated profile for both d-limonene SOA_{O3} and SOA_{OH}. Significant amounts of $R_1R_2CH(OH)$ are predicted in most SOA (34%–74%). Primary and secondary alcohols are generated via multigenerational gas-phase oxidation as shown in a number of previous experimental and theoretical studies as summarized in review papers (Vereecken and Francisco 2012; Ziemann and Atkinson 2012). α-terpineol SOA_{O3} is estimated to contain a very small fraction of $R_1R_2CH(OH)$ (0.1%–1%), leading to suppression of the $\cdot O_2^-/HO_2\cdot$ formation. This is likely caused by the specific position of hydroxy groups in α-terpineol: tertiary alcohol without α-H for abstraction and subsequently no formation of peroxyl radicals. The predicted very low fraction of $R_1R_2CH(OH)$ in α-terpineol SOA_{O3} is consistent with previous experimental measurements (Leviss et al. 2016), showing that the primary products (>90%) from α-terpineol ozonolysis only contain tertiary alcohols.

Effects of NO_x on ROS Formation from SOA

Naphthalene and α-pinene SOA generated in the chamber were collected for analysis of ROS. SOA samples were extracted in a spin-trapping BMPO solution that was able to capture different types of radical species for detection with EPR spectroscopy. **Figure 5** shows that α-pinene SOA generated under the NO_x-free condition mainly generates ·OH radicals and $\cdot O_2^-/HO_2\cdot$, which is consistent with our previous study (Wei et al. 2021b). ·OH radicals can be generated by the decomposition of ROOH (Tong et al. 2016), and superoxide can be formed by ·OH oxidation of primary and secondary alcohols and unimolecular decomposition of

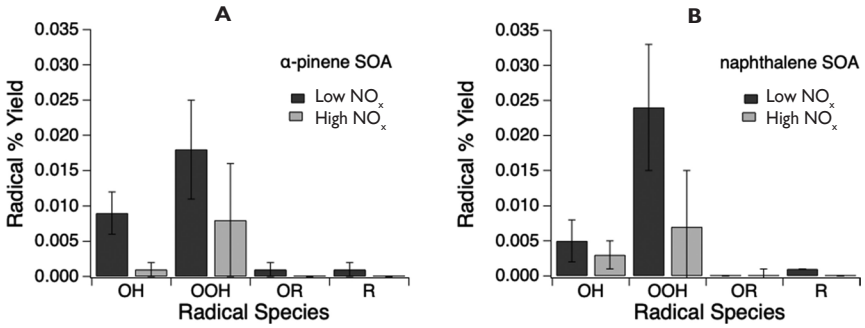

Figure 5. Molar yields of BMPO radical adducts (BMPO-OH, BMPO-OOH, BMPO-OR, and BMPO-R) generated from aqueous reactions of A. α-pinene SOA and **B**. naphthalene SOA, generated with NO_x concentrations of 0 and 700 ppb. Error bars represent one standard deviation of 5 replicate measurements. Adapted from Edwards et al. 2022.

α-hydroxyperoxy radicals (Wei et al. 2021b). Naphthalene SOA generated under the NO_x-free condition shows the dominant superoxide formation, which is most likely generated via redox reactions of quinones (Tong et al. 2018). The formation of organic radicals is relatively minor for both SOA.

For SOA generated under high NO_x, ROS production was diminished for both naphthalene and α-pinene SOA. For α-pinene SOA, the total radical yield decreased with ·OH, and superoxide formation decreased by a factor of ~10 and ~2, respectively. For naphthalene SOA, the total radical yield was reduced, with ·OH and superoxide reduction by a factor of ~1.5 and ~3, respectively. Given that the pH of SOA extracts were in the range of 3–6 and considering that the pKa of HO_2· was 4.88, HO_2 would be the dominant species as the pH approaches 3, $\cdot O_2^-$ would be dominant at pH 6, and HO_2· and $\cdot O_2^-$ production would be similar around pH 5. SOA extracts were slightly more acidic for high NO_x SOA compared with low NO_x SOA; in any case, we expect both species HO_2· and $\cdot O_2^-$ to be present for this pH range. Note that our recent study showed that ROS production by α-pinene and naphthalene SOA generated under NO_x free would be higher at lower pH (Wei et al. 2022), but the influence of NO_x has a greater effect on ROS yield than does the pH of the system. Acid may reduce the formation of semiquinone, which may contribute to the reduction of ROS formation.

Given that ROOH is an important source of ROS, we have quantified peroxides using an iodometric spectrophotometric method. We found that α-pinene SOA generated with the NO_x-free condition contains substantial amounts of peroxides, which decreased significantly by a factor of ~7 for SOA generated with 700 ppb NO_x, while peroxide contents are comparable for naphthalene SOA for both NO_x conditions. The fate and reaction pathways of peroxy radicals (RO_2·) are critical for SOA formation. There are competitions of NO_x and HO_2· to react with RO_2· radicals leading to different products as follows:

R4: $RO_2 + NO \rightarrow RONO_2$ or $RO + NO_2$

R5: $RO_2 + NO_2 \rightarrow RO_2NO_2$

R6: $RO_2 + HO_2 \rightarrow ROOH + O_2$

Under high NO_x conditions, R4 and R5 dominate over R6; hence, ROOH is substantially reduced.

High-Resolution Mass Spectrometry High-resolution mass spectrometry shows that both naphthalene and α-pinene SOA show significant incorporation of nitrogen at high NO_x conditions. The addition of NO_x during SOA formation has led to the formation of many nitrogen-containing compounds. While our mass spectrometry method does not provide individual functional group information, based on previous work we expect the nitrogen-containing groups in the naphthalene SOA to be mostly nitroaromatics (RNO_2) and in the α-pinene SOA to be organonitrates ($RONO_2$). Both SOA types show monomer (>250 Da) and dimer (250–500 Da) regions. The α-pinene SOA also shows the formation of a small trimer region above 500 Da. The major peaks in both naphthalene SOA conditions generally have formulas of $C_{8-10}H_{6-8}O_{2-5}$. The major peaks in both α-pinene SOA conditions have formulas of $C_{8-10}H_{12-16}O_{2-5}$. For the α-pinene SOA, there are also a few C_7 compounds that are abundant and less typical of previously reported α-pinene SOA. These C_7 compounds may be a result of in-source fragmentation due to the spray voltage being too high during mass spectrometry analysis, particularly since this is not evident in the aromatic naphthalene SOA, which will be less susceptible to fragmentation. The high NO_x environment saw the incorporation of nitrogen into the final product, forming an organic nitrate. In the complete product list, more organic nitrate compounds were present as well, agreeing with the aforementioned studies that show the formation of these compounds in a high NO_x environment.

Effects of pH on ROS Formation from SOA

Acidity is an important physicochemical property of atmospheric aerosols, but its effects on the ROS formation from SOA have been poorly characterized. By applying the EPR spin-trapping technique and the Diogenes chemiluminescence assay, we investigated radical yields and composition at differing pH in the range of 1–7.4 from SOA generated by oxidation of isoprene, α-terpineol, α-pinene, β-pinene, toluene, and naphthalene. The solid color bars in **Figure 6** show the relative abundance and BMPO-radical yields from

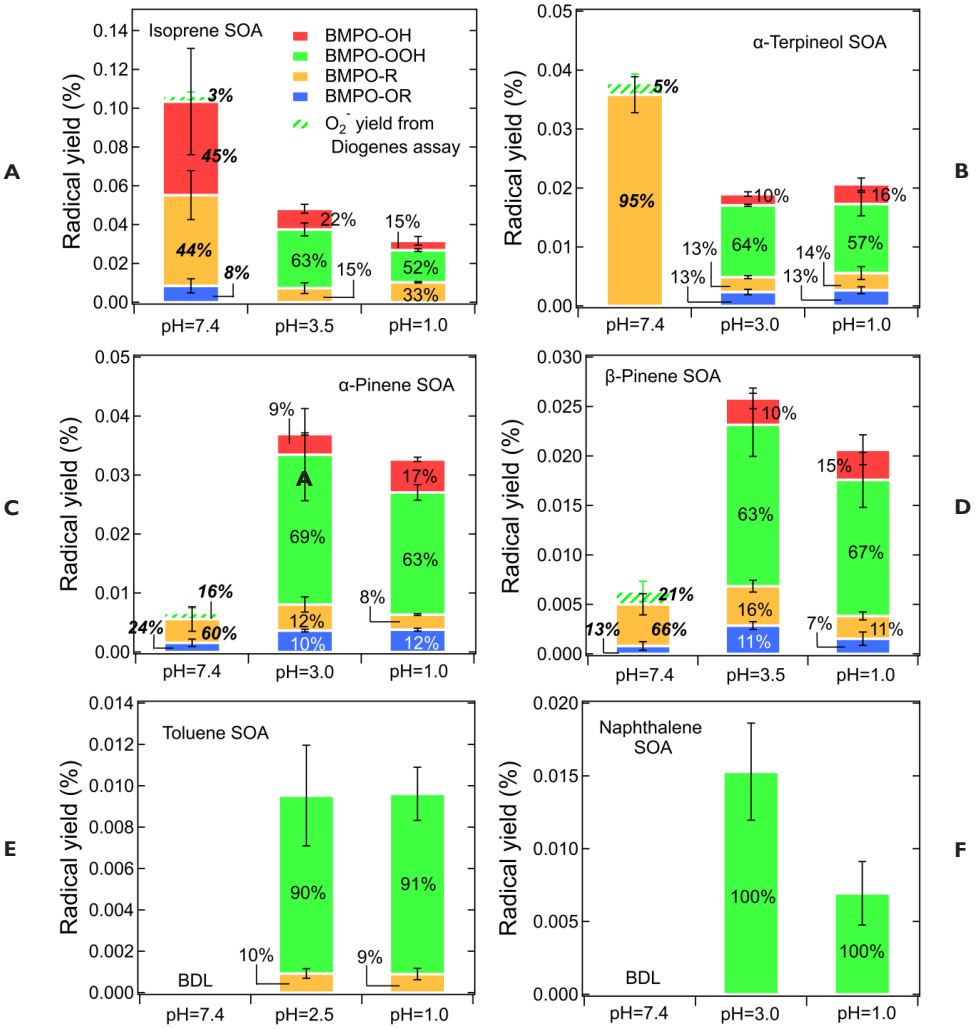

Figure 6. Yields and relative abundance of different radical species from A. isoprene SOA, **B.** α-terpineol SOA, **C.** α-pinene SOA, **D.** β-pinene SOA, **E.** toluene SOA, and **F.** naphthalene SOA at different pH in the presence of spin-trapping agent BMPO. The solid-colored bars represent BMPO-radical adducts measured by EPR, while the green dashed bars represent superoxide yields estimated from the Diogenes assay. Note the italic bold numbers at pH 7.4 are calculated combining the results of EPR and the Diogenes assay. The error bars represent the error propagation from the two duplicates in EPR measurements or the Diogenes assay with the uncertainty in SOA mass measurements. Adapted from Wei et al. 2022.

SOA generated from six different precursors. The BMPO-radical adduct yields from isoprene and α-terpineol SOA at neutral pH are significantly enhanced to 0.10% and 0.035% from <0.05% and <0.02% at acidic conditions, respectively. Isoprene SOA at neutral pH generated substantial amounts of ·OH (45%) and R· (44%) with a very minor contribution from RO· (8%), while α-terpineol SOA shows dominant R· formation at neutral pH (Figure 6A, B). In comparison, both isoprene and α-terpineol SOA produced $\cdot O_2^-/HO_2\cdot$ (52%–64%) predominantly in acidic conditions, while ·OH (10%–22%) and R· and RO· (13%–33%) constituted only minor fractions, as consistent with our recent study (Wei et al. 2021a). It should be noted that the highly acidic condition (pH = 1.0) does not lead to notable differences in radical yields and relative abundance compared with the original SOA extracts with moderately acidic conditions (pH = 3.0–3.5).

In addition, we characterized radical formation from α-pinene, β-pinene, toluene, and naphthalene SOA (Figure 6 C–F) at differing pH. α-pinene and β-pinene SOA (Figure 6C, D) showed an inverse trend to isoprene and α-terpineol SOA, with substantially lower BMPO-radical yields at neutral pH (<0.01%) compared with acidic conditions (0.02%–0.036%). At neutral pH, α-pinene and β-pinene SOA mainly generated low amounts of R· and RO·, while the dominant formation of $\cdot O_2^-/HO_2\cdot$ (>60%) was observed under acidic conditions, similar to isoprene and α-terpineol SOA. For aromatic (toluene and naphthalene) SOA (Figure 6E, F), we observed

dominant superoxide formation (90%–100%) in acidic solutions, whereas no radicals above detection limit were found at neutral pH.

An interesting result as observed from Figure 6 is that no BMPO-OOH (green solid bars) was detected at pH 7.4 for all SOA, raising a question if the EPR spin-trap method with BMPO can detect superoxide efficiently at neutral pH. Given the pKa of $HO_2\cdot$ (4.88), the predominant form of superoxide in acidic conditions (pH 3.0 and 1.0) should be $HO_2\cdot$, whereas it is $\cdot O_2^-$ at neutral pH (Gutteridge 1995). It has been reported that a nitrone spin trap can react with $HO_2\cdot$ very efficiently (e.g., BMPO + $HO_2\cdot \rightarrow$ BMPO-OOH), while the trapping of $\cdot O_2^-$ is a two-step process via an initial addition of $\cdot O_2^-$ to BMPO to form the BMPO-O_2^- adduct followed by protonation by water (or other acidic sources) to form BMPO-OOH (Villamena et al. 2005). As a consequence, the overall rate of $\cdot O_2^-$ trapping in neutral conditions can be an order of magnitude slower compared with $HO_2\cdot$ trapping in acidic conditions (Tsai et al. 2003). Hence, we applied the Diogenes chemiluminescence assay, which is more sensitive in superoxide measurements at neutral pH. All biogenic SOA show positive superoxide production rates, varying from 0.005–0.013 μM min^{-1}. In contrast, toluene and naphthalene SOA do not generate $\cdot O_2^-/HO_2\cdot$ above the detection limit, as consistent with the EPR spin-trap method (Figure 6E, F). Overall, the cross-validation by the Diogenes assay suggests that the superoxide yields at neutral pH may be underestimated by BMPO trapping. Therefore, we estimated the total superoxide production yields by the Diogenes assay at neutral pH, which are added as green dashed bars in Figure 6. For isoprene and α-terpineol SOA, the additional $\cdot O_2^-$ formation at pH 7.4 can further increase the enhancement factors compared with acidic conditions, while the radical yields from α-pinene and β-pinene SOA are still much lower at neutral pH even after considering $\cdot O_2^-$ formation. Both methods confirm that superoxide formation is below the detection limit from toluene and naphthalene SOA at pH 7.4, consolidating that aromatic SOA containing quinone-type compounds mediate redox cycling and $\cdot O_2^-$ formation in a pH-dependent manner (Guin et al. 2011).

To better understand the pH effects on ROS formation mechanism from SOA, we measured radical formation from commercially available ROOH at differing pH. We found predominant ·OH formation (70%–90%) from 10 mM cumene hydroperoxide and *tert*-butyl hydroperoxides at neutral pH, with total radical yields up to 0.014% and 0.04%, respectively. The unimolecular decomposition of labile ROOH can lead to ·OH formation through the cleavage of the weaker O-O bond (Krapf et al. 2016; Tilgner and Herrmann 2018). In acidic solutions (pH 3.0 and 1.0), however, both ROOH generate much lower ·OH (radical yields <0.0009%). While the first-order decomposition of peroxides should be a thermal process depending on temperature instead of pH, it may be suppressed at higher acidity due to the acid-catalyzed rearrangement of alkyl hydroperoxides (Anderson and Smith 1968; Levin et al. 2006; Walling 1963). This alternative pathway would lead to alcohol and ketone formation as the end products, involving no radical formation (Yaremenko et al. 2016). A similar mechanism has also been shown for aliphatic alkyl hydroperoxides including *tert*-butyl hydroperoxide (Deno et al. 1970). Therefore, it may partially account for the decreased radical formation by isoprene and α-terpineol SOA at lower pH, although the complex and multifunctionalized nature of ROOH in SOA may not be accurately represented by cumene or *tert*-butyl hydroperoxides. The major contribution from ·OH by isoprene SOA may be due to its higher fraction of ROOH (3%–5%) compared with α-terpineol SOA (1%–3%) (Wei et al. 2021b).

Quinones, often contained in aromatic SOA, are well known to induce superoxide formation: in the presence of an electron donor, quinones can be reduced to semiquinone radicals that can further react with dissolved O_2 to form superoxide (Bates et al. 2019; McWhinney et al. 2013). The pH dependence of the quinone redox cycling has rarely been discussed in the context of ambient PM, so we measured radical formation in the mixture of 0.2 mM 5-hydroxy-1,4-naphthoquinone (5-H-1,4-NQ) and 0.2 mM ascorbate. Note that 5-H-1,4-NQ alone did not generate radicals above the detection limit. We found significantly higher superoxide production at lower pH. It has been demonstrated that the quinone–hydroquinone couple has a redox potential dependent on pH in a straightforward Nernstian manner (Guin et al. 2011), which follows that increasing pH causes a decrease in the redox potential (Walczak et al. 1997). This provides a thermodynamic explanation on favoring $\cdot O_2^-/HO_2\cdot$ formation through stronger quinone redox cycling in acidic conditions compared with neutral pH (Figure 6E, F). It has been shown that hydroquinones can be unstable at physiological pH, undergoing autoxidation to form semiquinone radicals and quinones with the concomitant generation of $\cdot O_2^-$ and H_2O_2 (Yuan et al. 2014). Further studies are necessary to evaluate the relevance of such pathways, especially for SOA generated from phenolics such as catechol and cresol (Hoffmann et al. 2018; Schwantes et al. 2017).

In addition to radicals, we characterized H_2O_2 yields from all SOA at differing pH. Overall, higher H_2O_2 yields are consistently observed for all SOA as pH decreases from 7.4 to 1.0, with the enhancement factors varying from 1.5 to 3. This is in good agreement with Wang and colleagues (2011b) who observed that H_2O_2 generation by α-pinene, β-pinene, and toluene SOA increased by a factor of 1.5, 2.4, and 1.75, respectively, when pH decreased from 7.5 to 3.5. Isoprene SOA shows significantly higher yields of H_2O_2 (4.0%–6.6%), compared with other SOA (<2.0%) with the H_2O_2 level (4.2%) in the original extract (pH 3.5), in excellent consistency with our previous study (4.3% ± 0.4%) (Wei et al. 2021b). Naphthalene SOA shows the second highest H_2O_2 yields (1.4%–2.0%), which is comparable with Liu and colleagues (2020) (1.9%–2.5%). Qiu and colleagues (2020b) recently proposed that the decomposition of α-hydroxyalkyl-hydroperoxides is a proton-catalyzed process associated with H_2O_2 formation, which is a highly plausible mechanism accounting for the elevated H_2O_2 yields from biogenic SOA. For toluene and

naphthalene SOA, the enhanced superoxide formation with higher acidity may subsequently lead to H_2O_2 yields because $\cdot O_2^-$ is known as an important precursor of H_2O_2 (Hayyan et al. 2016). Given the low $\cdot O_2^-$ formation but high H_2O_2 yields from naphthalene SOA, additional H_2O_2 sources could be important, including decomposition of hydroxyhydroperoxides (Liu et al. 2020), which may account for significant fractions in naphthalene SOA (Kautzman et al. 2010).

Organic Radical Formation by SOA in ELF

Respiratory deposition of SOA and iron may lead to the generation of ROS and free radicals in lung fluid to cause oxidative stress, but their underlying mechanism and formation kinetics are not well understood. In this work we demonstrate substantial formation of organic radicals in SLF by mixtures of Fe^{2+} and SOA generated from photooxidation of isoprene, α-terpineol, and toluene. **Figure 7A** shows the observed EPR spectra of isoprene SOA in water and SLF in the absence of Fe^{2+} or in the presence of 0.4 mM Fe^{2+}. As shown in Figure 7B, we find striking enhancements in the observed total radical yields with Fe^{2+} addition in both water (from 0.07% to 0.57%) and SLF (from 0.005% to 0.42%) with large changes in radical composition. Isoprene SOA in water leads to the predominant formation of superoxide (64%) with a minor contribution from ·OH and R·. Upon the addition of 0.4 mM Fe^{2+}, the radical profile becomes dominated by ·OH (77%) with contributions from $\cdot O_2^-/HO_2\cdot$ (15%) and R· (8%). In the presence of antioxidants in SLF without Fe^{2+}, only R· are observed, while a minor contribution from RO· (16%) is also observed with 0.4 mM Fe^{2+}. ·OH and $\cdot O_2^-/HO_2\cdot$ radicals are not observed in SLF, indicating effective scavenging of these highly reactive species by antioxidants, which is consistent with the formation of $Asc^{\cdot-}$ (Buettner and Jurkiewicz 1993) in Figure 7A.

In addition to isoprene SOA, α-terpineol and toluene SOA are also characterized for the radical yields in water and SLF. In water, α-terpineol and toluene SOA alone consistently generate radicals dominated by $\cdot O_2^-/HO_2\cdot$ (>90%). The total radical yields are elevated by a factor of 4–8 upon Fe^{2+} addition: α-terpineol SOA exhibits dominant (83%) ·OH formation, which is similar to isoprene SOA (77%), while we observe no ·OH above the detection limit from toluene SOA + Fe^{2+} in water. In SLF, Figure 7B shows consistent enhancement effects by Fe^{2+} in organic radical formation, with radical yields increasing substantially from 0.008% to 0.19% for α-terpineol SOA and from below the detection limit to 0.04% for toluene SOA, respectively. R· are the dominant species for α-terpineol (92%) and toluene (74%) SOA with minor contributions from RO· (8% and 26%, respectively). Overall, we observe the highest radical yields and strongest enhancement effects of Fe^{2+} (by a factor up to ~80) from isoprene SOA, followed by α-terpineol and toluene SOA.

To elucidate the chemical mechanisms of organic radical formation by SOA and Fe^{2+}, we developed and applied a kinetic model to simulate the temporal evolution of R· and RO· radicals. The following reactions were implemented into the kinetic model for radical formation from isoprene SOA and Fe^{2+} based on previous studies:

R1: $ROOH \rightarrow RO\cdot + \cdot OH$

R7: $ROOH + Fe^{2+} \rightarrow RO^- + \cdot OH + Fe^{3+}$

R2: $R_1R_2CHOH + \cdot OH \xrightarrow{O_2} c_1\ R_1R_2C(O_2)OH\cdot$

R3: $R_1R_2C(O_2)OH\cdot \rightarrow R_1C(O)R_2 + HO_2\cdot$

R8: $ROOR' + Fe^{2+} \rightarrow RO\cdot + R'O^- + Fe^{3+}$

SOA contains ROOH, which can undergo thermal decomposition to yield ·OH radicals (R1), which can be drastically promoted by Fe^{2+} with the Fenton-like reaction leading to

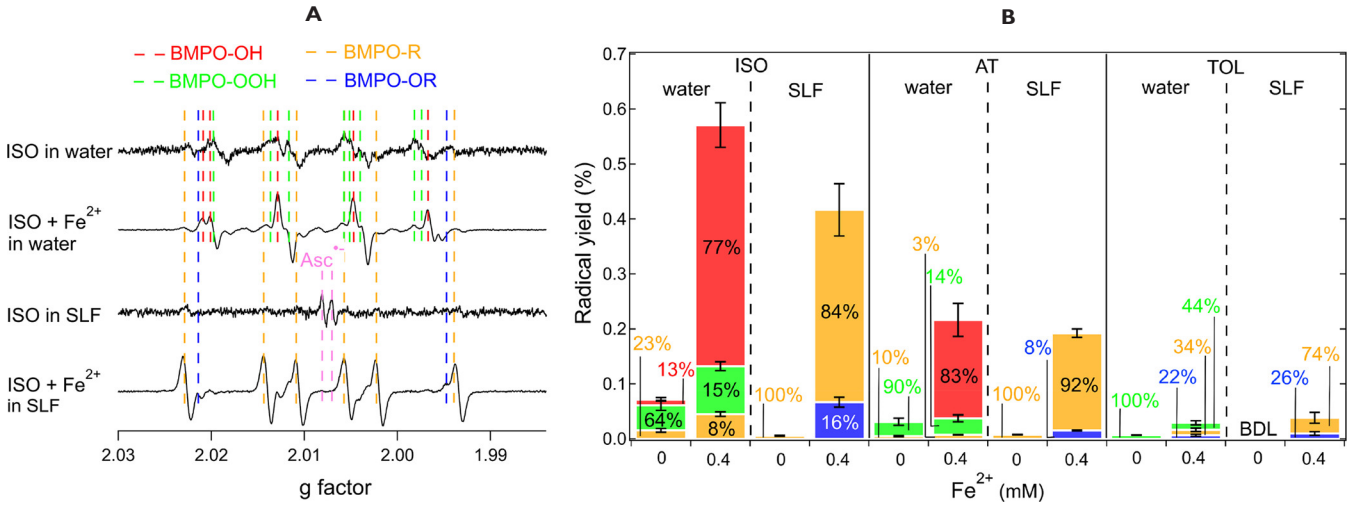

Figure 7. A. EPR spectra of isoprene SOA with 0 or 0.4 mM Fe^{2+} in water and SLF in the presence of spin-trapping agent BMPO. The dashed vertical lines represent different BMPO-radical adducts and $Asc^{\cdot-}$. **B.** Yields and relative abundance of different radical species including BMPO-OH (red), BMPO-OOH (green), BMPO-R (yellow) and BMPO-OR (blue) from isoprene (ISO), α-terpineol (AT), and toluene (TOL) SOA in water and SLF with 0 or 0.4 mM Fe^{2+}. The radical yields shown peaked at a reaction time of 20 min in water and 60 min in SLF, respectively. The error bars represent the error propagation from the two duplicates in EPR measurement and the uncertainty in SOA mass measurements. BDL = below the detection limit. Reprinted with permission from Wei et al. 2021a. Copyright 2021 American Chemical Society.

enhanced formation of ·OH (R7) (Tong et al. 2016). HO_2· is formed subsequently by ·OH oxidation of primary or secondary alcohols (R_1R_2CHOH), followed by fast addition of dissolved O_2 (R2) and unimolecular decomposition of α-hydroxyperoxyl radicals (R3) (Herrmann et al. 2005). Our recent study showed that this mechanism can explain the dominated $·O_2^-/HO_2$· formation from the aqueous reactions of isoprene and terpene SOA in the absence of Fe^{2+} (Wei et al. 2021b). While organic peroxides (ROOR') are thermally stable, they are known to be reactive toward Fe^{2+}, releasing RO· radicals (R8) in analogy to R7 (Denisov and Tumanov 2005; Eames and Watkinson 2001). To confirm Fe^{2+}-facilitated decomposition of ROOR, we measured radical formation in mixtures of Fe^{2+} and commercially available ROOH and peroxides in water and SLF. *tert*-butyl peroxybenzoate, *tert*-butyl peracetate (a ROOR) and cumene hydroperoxide (an ROOH) produce various radicals via Fenton-like reactions of Fe^{2+} in water. In SLF, only R· was formed, and other radicals (·OH, $·O_2^-$, RO·) were hardly observed. It indicates efficient scavenging of reactive radicals by antioxidants and rapid conversion of RO· to R·. Indeed, we observed significantly higher formation of R· than RO· from isoprene SOA in both water and SLF (**Figure 8**A, B), most likely due to the rapid conversion of RO· to R· via isomerization, decomposition, and a bimolecular reaction resulting in H abstraction (Studer and Curran 2016).

The significantly higher formation of organic radicals in SLF than in water can be attributed to redox cycling of Fe^{3+}/Fe^{2+} mediated by antioxidants: $Fe^{3+} + AscH^- \rightarrow Fe^{2+} + H^+ + Asc·^-$. Fe^{3+} can be reduced rapidly to regenerate Fe^{2+} by $Asc·^-$ (Buettner and Jurkiewicz 1996; Lakey et al. 2016; Sun et al. 2020; Valko et al. 2005) to sustain organic radical formation. The model sensitivity analysis revealed that such recycling of Fe^{2+} contributes to 5–10 times higher organic radical formation in the SLF than in water. Note that a very recent study suggested that Fe^{3+} and ascorbate reactions are catalytic rather than redox reactions (Shen et al. 2021): Fe^{3+} + ascorbate + O_2 → Fe^{3+} + dehydroascorbic acid + H_2O_2. To further investigate the nature of the Fe^{3+}–ascorbate reaction, we measured Fe^{2+} in the mixtures of Fe^{3+} and ascorbate in water or PBS buffer solutions. We found that 12%–14% of Fe^{3+} can be reduced to form Fe^{2+} in water, which can be further enhanced when buffered by PBS (18%–47%). In addition, EPR measurements showed that $Asc·^-$ is formed in the Fe^{3+}–ascorbate mixtures when buffered by PBS, which is only generated by redox

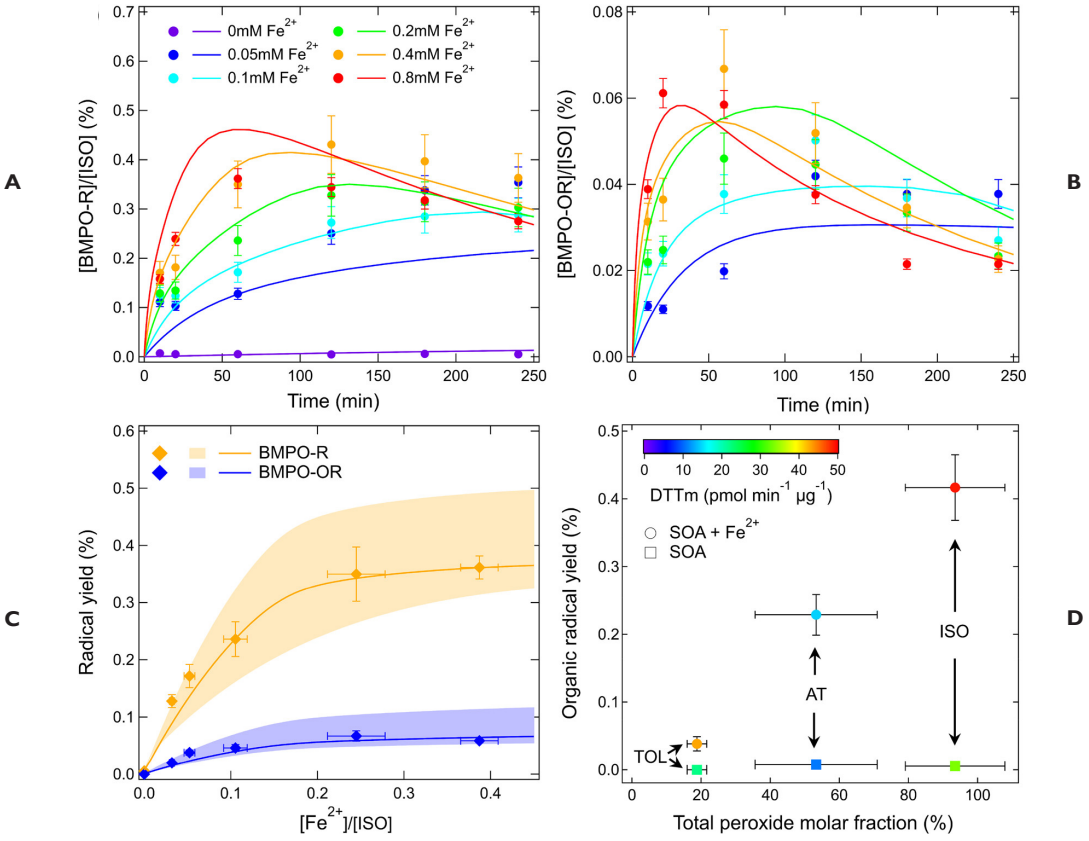

Figure 8. Temporal evolution of molar yields of A. BMPO-R and B. BMPO-OR from aqueous reactions of isoprene SOA and Fe2+ (0–0.8 mM) in SLF. **C**. Yields of R· (yellow) and RO· (blue) from isoprene SOA in SLF as a function of $[Fe^{2+}]/[ISO]$ molar ratios. The markers are experimental data. The solid lines represent the best fits of the kinetic model and the shaded areas represent the modeling uncertainties. **D**. Organic radical yields (BMPO-R + BMPO-OR) are plotted against total peroxide molar fractions in isoprene, α-terpineol, and toluene SOA with 0 (square) or 0.4 mM (circle) Fe^{2+}. The color scale represents the DTT consumption rate normalized by SOA mass (DTTm). The error bars in all panels represent the error propagation from the two duplicates in EPR measurement or total peroxide measurement and the uncertainty in SOA mass measurements. Reprinted with permission from Wei et al. 2021a. Copyright 2021 American Chemical Society.

instead of catalytic reactions. Interestingly, both Fe^{2+} and $Asc^{\cdot-}$ measurements indicate that Fe^{3+}–ascorbate redox reactions are highly pH-dependent and more prominent when buffered by PBS. We also conducted sensitive analysis in the model, showing that the redox reactions remain the dominant channel of Fe^{3+}–ascorbate interaction even if the catalytic reactions are considered. Future studies are required to elucidate the relative importance of catalytic and redox reactions between Fe^{3+} and ascorbate particularly under differing pH.

Overall, the implemented mechanisms successfully reproduce the time dependence of organic radical formation (Figure 8A, B) as well as the concentration dependence (Figure 8C), demonstrating the consistency of model simulations with experiments. We measured peroxide molar fractions in SOA, showing a positive correlation with organic radical yields by SOA in the presence of Fe^{2+} (circles in Figure 8D). It indicates that peroxides (ROOR + ROOH) are highly probable sources of aqueous organic radical formation. This is in line with a very recent study showing that the total ROS production from cooking SOA can be enhanced substantially through atmospheric aging, coinciding with the elevation in peroxide contents (Wang et al. 2021). Isoprene SOA is measured to have high peroxide content (~97%) compared with the measurements of Surratt and colleagues (2006) (~61%, from a Teflon chamber). This difference may be due to excess $RO_2\cdot$ chemistry in the PAM reactor, inducing more production of peroxides through termination steps such as $RO_2\cdot + HO_2\cdot \rightarrow$ ROOH and $RO_2\cdot + RO_2\cdot \rightarrow$ ROOR (Ziemann and Atkinson 2012). Toluene SOA has the lowest peroxide content with 18%, which is consistent with a previous study (Sato et al. 2007), leading to a lower organic radical yield.

To investigate the linkage between organic radical formation and OP, we performed the DTT assay on mixtures of SOA and Fe^{2+}; the results are shown by the color scale in Figure 8D. The DTT consumption rates normalized by SOA mass (DTTm) for isoprene SOA (33.4 ± 6.2 pmol min^{-1} μg^{-1}) and toluene SOA (22.3 ± 2.5 pmol min^{-1} μg^{-1}) are consistent with previous studies (Fujitani et al. 2017; Jiang et al. 2016). With the Fe^{2+} addition, clear enhancements of DTTm are observed for all types of SOA. Due to the moderate DTT activity from Fe^{2+} alone, SOA and Fe^{2+} demonstrate a strong synergistic effect in causing OP. Figure 8D shows no clear association between organic radical yields and DTTm. Despite the lowest organic radical yields from mixtures of toluene SOA and Fe^{2+}, they induce relatively high DTTm (42.8 ± 0.4 pmol min^{-1} μg^{-1}), which is comparable with mixtures of isoprene SOA and Fe^{2+} (49.0 ± 11.2 pmol min^{-1} μg^{-1}). Tuet and colleagues (2017b) reported generally higher DTT activities from anthropogenic SOA than from biogenic SOA, although the interactions of SOA and transition metals in OP are still understudied. Dedicated studies are necessary to further elucidate the link between ROS formation and OP from SOA.

ROS FORMATION FROM AMBIENT PARTICLES

ROS Formation from Highway and Wildfire PM

The EPR measurements show that ambient $PM_{2.5}$ collected from the two highway sites generate mainly ·OH and R· upon interaction with water (**Figure 9**). ROS from highway and urban background are predominantly comprised of ·OH (84%–88%) with a 12%–16% contribution from R· for both PM_1 and $PM_{1–10}$. The dominant contribution of ·OH in ROS formation at highway and urban particles is also supported by ·OH and total radical forms of ROS showing very similar size distributions, ROSm levels, and a tight correlation (R^2 = 0.99). In contrast, for the wildfire PM, ·OH and R· have roughly equal contributions (~50%) to the total radical forms of ROS in $PM_{1–10}$, whereas in PM_1, R· (54%) and ·OH (28%) contribute substantially with some contribution from RO· (13%) and $\cdot O_2^-/HO_2\cdot$ (5%). The correlation between ·OH and total radical forms of ROS from the wildfire PM is strong for particle sizes larger than 1 µm (R^2 = 0.89), while the correlation for PM_1 is weaker (R^2 = 0.40).

As shown in **Figure 10A**, ROS generated by wildfire PM have distinct frequency size distributions compared with those in highway and urban PM. Total radical forms of ROS in wildfire particles show a bimodal distribution with one peak at small sizes (0.056–0.18 µm) and the other peak at large sizes (10–18 µm), whereas total radical forms of ROS in highway PM exhibit a single mode peaking at the 0.56–1 µm size range; urban PM has another peak at 10–18 µm. The ambient concentrations of ROSv in PM_1 and $PM_{1–10}$ follow the

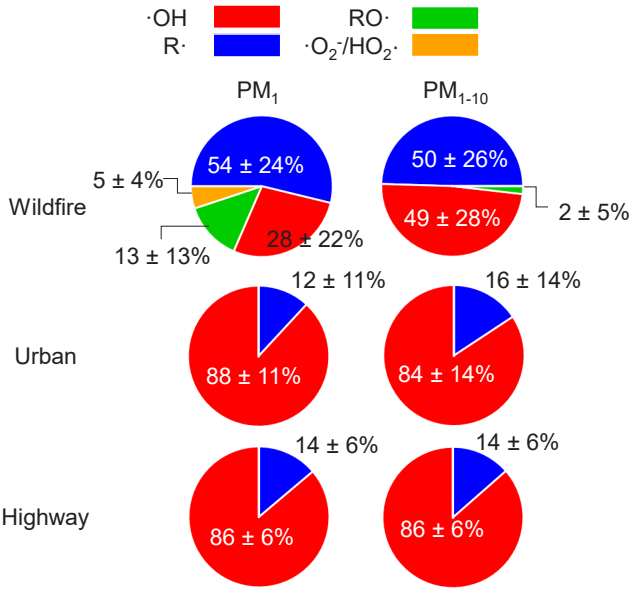

Figure 9. Averaged fractions of ·OH, R·, RO·, and $\cdot O_2^-/HO_2\cdot$ in total radical formation in the aqueous extracts of PM_1 and $PM_{1–10}$ collected during wildfire events and at highway and urban sites in the Los Angeles area (see sampling locations in Figure 2). Adapted from Fang et al. 2023.

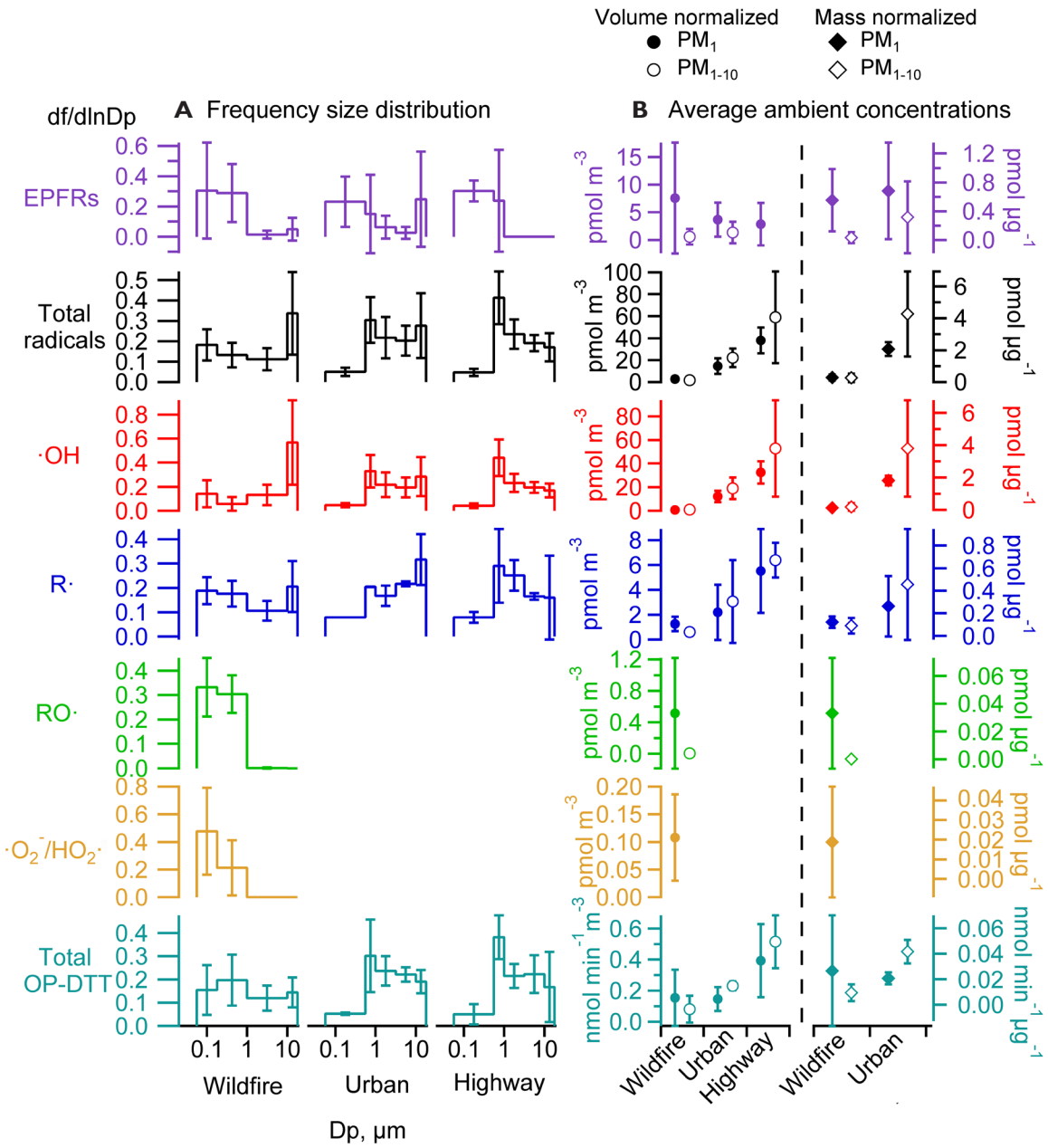

Figure 10. A. Average frequency distributions and **B**. air volume-normalized and PM mass-normalized concentrations of EPFRs, ROS, and total OP-DTT of ambient PM collected during wildfire events ($N = 8$) and at highway ($N = 3$) and urban ($N = 3$) sites. Data are presented as mean and the standard deviation from different sampling days. PM_1 and PM_{1-10} are sum of all MOUDI stages up to 1 µm and between 1 and 10 µm, respectively. PM mass concentrations are not available at the highway sites. Adapted from Fang et al. 2023.

order of highway > urban > wildfire (Figure 10B). In terms of ROSm, the urban PM has much higher levels in PM_1 and PM_{1-10} compared with the wildfire PM. These results suggest that wildfire emissions lead to less total radical formation compared with traffic emissions. This may be because biomass burning PM contains many pyrolyzed, less oxidized, and insoluble components as well as inorganics such as potassium and sulfate, which are not redox active (Khamkaew et al. 2016; Li et al. 2021).

RO· and $\cdot O_2^-/HO_2\cdot$ are only observed in wildfire PM_1. RO· shows a strong correlation with total radical forms of ROS ($R^2 = 0.71$) and a moderate correlation with R· ($R^2 = 0.53$). $\cdot O_2^-/HO_2\cdot$ is moderately correlated with the total radical forms of ROS ($R^2 = 0.41$) and ·OH ($R^2 = 0.50$) but is not correlated with RO· or R·. The correlations among different radical species suggest that the organic radicals (RO· and R·) would be associated with similar aqueous chemistry that may be distinct from the formation chemistry of ·OH and $\cdot O_2^-/HO_2\cdot$. Biomass

burning has been found to be an important primary source for ROOH (Lee et al. 1997; Snow et al. 2007). The decomposition of ROOH can generate alkoxyl and ·OH radicals (Fang et al. 2020; Tong et al. 2016, 2018). Alkoxyl radicals can undergo decomposition (e.g., RO· → R'· + R"C(O)H) and isomerization (e.g., RO· → (OH)R·) to form alkyl radicals (Chen et al. 2011a), whereas ·OH oxidizes primary or secondary alcohols to form α-hydroxyalkyl radicals, followed by O_2 addition to form α-hydroxyperoxyl radicals that may decompose to form $\cdot O_2^-/HO_2\cdot$ (Wei et al. 2021b). The correlations between ·OH and $\cdot O_2^-/HO_2\cdot$ may also be explained by a common role of iron ions in the decomposition of H_2O_2 to form ·OH and reduction of O_2 to form $\cdot O_2^-$ (Fenton 1894; Santana-Casiano et al. 2005); synergistically, these Fe-mediated ·OH and $\cdot O_2^-$ formations may be enhanced by the presence of HULIS and quinones in biomass burning PM (Charrier and Anastasio 2015; Gonzalez et al. 2017; Xiong et al. 2017). Other chemical components in biomass burning may also explain the ROS formation: for example, ROOR can react with iron ions to form organic radicals (Wei et al. 2021a); Fe–organic complexes may release ROS by photolytic reactions (Alpert et al. 2021), and EPFRs can also reduce the O_2 to form $\cdot O_2^-$ (Khachatryan et al. 2011). Overall, the observed ROS formation should be a consequence of highly complex chemistry involving a variety of reactive and redox-active components in biomass burning PM; future laboratory studies are warranted to characterize specific ROS formation pathways and to investigate the interplay of different components with surrogate mixtures with known PM components.

Measured ROS Formation vs. OP by DTT Assay

In Figure 10A, total OP-DTT for highway and urban PM shows a unimodal distribution with the peak at 0.56–1 μm, and total OP-DTT in PM_{1-10} is higher than in PM_1. The highway PM has higher levels of total OP-DTTv than does the urban PM, which may be partly caused by nonexhaust emissions of transition metals with large OP at highways (Fang et al. 2016; Gao et al. 2017; Saffari et al. 2014; Zhang et al. 2016). The two highway sites have similar levels of total DTT activities and the average total DTTv (normalized by sampled air volume) and DTTm (normalized by particle mass) are ~0.47 nmol min^{-1} m^{-3} and ~37 pmol min^{-1} μg^{-1} respectively. These values are similar or slightly higher than previous measurements at highway or road sites (Charrier et al. 2015; Gao et al. 2017; Shirmohammadi et al. 2017). The distribution of total OP-DTT for wildfire PM is relatively uniform across different particle diameter ranges, and submicron wildfire PM exhibits higher total OP-DTTv and OP-DTTm compared with coarse fractions. It is worth noting that wildfire PM shows a higher contribution from submicron particles to EPFRs, ROS formation, and total OP-DTT compared with highway and urban PM. This observation is consistent with the fact that DTT-active organics including quinones and HULIS (Dou et al. 2015; Verma et al. 2015b) are mostly contained in the submicron size range (Garofalo et al. 2019; Kleeman et al. 1999). Since submicron particles after inhalation can deposit deep into the lung, reaching the alveoli (Heyder 2004), it suggests that biomass burning contributes to deposition of organics and ROS in the lower respiratory tract and hence may play a role in inducing inflammatory responses and oxidative stress deeper in lung.

OP-DTT has been extensively used to indicate toxicity, assuming that it represents the ability of aerosols to generate ROS; this assumption still needs to be evaluated by investigating correlations between OP-DTT and ROS formation (Fang et al. 2019; Hwang et al. 2021; Xiong et al. 2017; Zhang et al. 2022). A recent study found that secondary inorganic components, crustal material, and biogenic SOA control PM mass concentrations, while OP is associated mostly with anthropogenic sources, in particular with residential biomass burning and metals from vehicular nonexhaust emissions (Daellenbach et al. 2020). Interestingly, total OP-DTT from highway and urban shows a positive moderate correlation with total radical forms of ROS (R^2 = 0.61, **Figure 11**) and ·OH (R^2 = 0.59). Interestingly, the total DTTv activities at the Anaheim are strongly correlated with ROSv (R^2 = 0.91). For individual ROS species, the correlations of total DTTv with organic radicals (R^2 = 0.85) are stronger than with OH radicals (R^2 = 0.71), suggesting that the DTT decay and the formation of organic radials are contributed by similar organic compounds. This is consistent with a recent study reporting that ROOH can consume DTT (Jiang et al. 2016). The lower correlation of total DTTv activities with OH radicals is expected as the DTT assay is less sensitive to Fe, which plays a large role in generating OH radicals through Fenton chemistry (Fang et al. 2019). There is little correlation between total DTTv activities and ROSv or individual species at the Long Beach site ($R^2 \leq 0.16$).

Total OP-DTT from wildfire samples does not correlate with any radical generation ($R^2 \leq 0.02$) (Figure 11). The correlation in highway and urban PM samples may be explained by transition metals such as Cu or Fe that can oxidize DTT (Charrier and Anastasio 2012; Charrier et al. 2016) and also participate in Fenton/Fenton-like reactions with H_2O_2 or hydroperoxides to generate ·OH (Chevallier et al. 2004; Fang et al. 2020). Previous studies have also found mixed results for such correlation analyses. For example, Zhang and colleagues (2022) found that OP-DTT and ROS measurements were positively correlated for photochemically aged naphthalene SOA with soot particles, while there was a weaker correlation for β-pinene SOA. Xiong and colleagues (2017) found that ambient $PM_{2.5}$ samples collected from an urban site in Illinois showed no correlation between OP-DTT and ·OH formation. The lack of correlation between OP-DTT and total radical forms of ROS in wildfire PM in this work indicates that OP would not be a good metric for radical generation in biomass burning aerosols. The mixed results in this study provide promising but cautious implications from ambient data that DTT activities could represent ROS generation, but further measurements with longer sampling time periods, and also at various locations with differing sources, are necessary to better understand the associations of ROS generation and DTT activities with oxidative stress induced by atmospheric

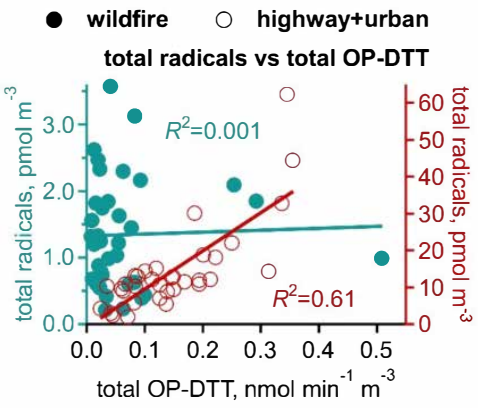

Figure 11. Correlations of total radicals with total OP-DTT during wildfire events and at highway and urban sites. Each data point represents data obtained from an individual MOUDI stage. Adapted from Fang et al. 2023.

PM and its adverse effects on human health. As this study did not measure nonradical forms of ROS such as H_2O_2 and singlet oxygen, further studies are necessary to fully evaluate validations and limitations of the use of OP as an indicator of ROS formation and PM toxicity. Other OP assays such as ascorbic acid or glutathione assays that measure the consumption of antioxidants could also be used to assess the relations of OP with ROS generation in future studies.

MODELING ROS FORMATION IN ELF

Respiratory deposition can lead to the formation of ROS in the ELF due to redox reactions of PM components with lung antioxidants. As a direct quantification of ROS is challenging, PM OP is more commonly measured using antioxidant surrogates, including DTT and ascorbic acid, assuming that the decay of surrogates corresponds to ROS formation. However, this assumption has not yet been validated and the lack of ROS quantification in the respiratory tract causes major limitations in evaluating PM impacts on oxidative stress. By combining field measurements of size-segregated chemical composition in Atlanta, a human respiratory tract model, and kinetic modeling, we quantified production rates and concentrations of different types of ROS in different regions of the ELF by considering particle-size-dependent respiratory deposition.

ROS Concentration in ELF in Various Respiratory Regions

Figure 12 shows the modeled total and individual ROS concentrations in the ELF in alveolar, bronchial, and extrathoracic regions after particle-size-dependent respiratory deposition at road-side and urban sites in Atlanta, GA. ROS concentrations and production rates depend strongly on the size-dependent composition of ambient PM and their deposition efficiencies in different ELF regions. The extrathoracic region is found to have the highest ROS concentrations

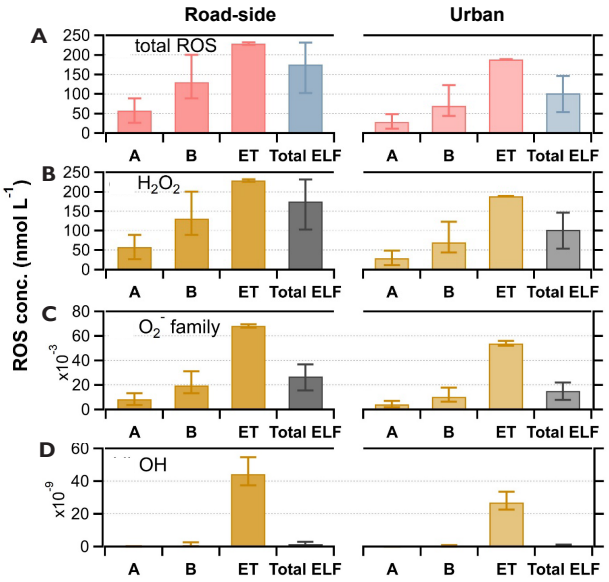

Figure 12. Estimates of ROS concentrations in the epithelial lining fluid in various respiratory compartments after 1.5 hours of inhalation and deposition of ambient size-segregated water-soluble Fe and Cu, SOA, and quinones at road-side and urban sites in Atlanta, GA. A. Total ROS; **B–D**. Individual ROS. Respiratory compartments include alveolar (A), bronchial (B), and extrathoracic (ET) regions. The blue and grey bars (denoted as Total ELF) represent ROS concentrations without considering particle-size dependence of ELF deposition in different regions and assuming homogeneous PM deposition in the total ELF volume. Uncertainties associated with the ELF thickness are represented by the error bars. Other model uncertainties are discussed in the text. Reprinted with permission from Fang et al. 2019. Copyright 2019 American Chemical Society.

compared with the lower respiratory tract, for all types of ROS, at both sites due to efficient PM deposition and a small ELF volume.

In Figure 12, Total ELF represents ROS concentrations if PM respiratory deposition would be assumed to be homogeneous without considering the particle-size dependence of ELF deposition in different respiratory regions. Comparisons of ROS from Total ELF to those in each respiratory region by considering size-dependent deposition suggest that assuming homogeneous deposition would lead to an underestimation of ROS concentrations in the extrathoracic region, while those in bronchi would be slightly overestimated and those for alveoli would be largely overestimated. This suggests that a proper consideration of the particle-size effect and dilution due to the ELF volume variations are important for accurate estimations of ROS concentrations in different respiratory regions. Comparing the two sites, the road-side site has higher levels of ROS estimated in the ELF in various respiratory compartments. This is due to higher ambient concentrations of various chemical species at the road-side site, resulting in higher concentrations of chemical species and ROS formation in the ELF.

H_2O_2 is the most abundant ROS in the ELF owing to its low reactivity and slow decomposition, and it is about four and ten orders of magnitude more abundant than the $\cdot O_2^-$ family and ·OH radicals, respectively. Although H_2O_2 is not a free radical, it may play a critical role in PM-induced oxidative stress, as H_2O_2 can diffuse through cell membranes and serve as a reservoir species to release more reactive forms of ROS in vivo (Mathai and Sitaramam 1994). ·OH radicals are mainly generated in the extrathoracic region. Transition metal ions are largely contained in coarse particles, which lead to higher deposition in the extrathoracic region, resulting in increased rates of Fenton and Fenton-like reactions to yield ·OH radicals. While ·OH concentrations are kept low due to scavenging by antioxidants, these results imply that oxidative damage to cells or tissues caused by highly reactive ·OH radicals would be more likely in the extrathoracic region than in the lower respiratory tract.

Composition-Dependent ROS Production Rates

We investigated modeled ROS production rates in different regions of ELF by individual chemical components, including Cu, Fe, SOA, and quinones, contained in size-segregated particles collected at the road-side site in Atlanta. We found that Cu has the highest ROS production rates, followed closely by Fe, while SOA rates are one order of magnitude less than Cu or Fe. Quinones have the lowest ROS production rates. The rate-limiting step for ROS production is the reduction of antioxidants. ELF concentrations of Cu and Fe are similar, but Cu has the highest ROS production rates due to the higher reaction rate coefficient (k = 1.4 × 10^{-18} cm^3 s^{-1}) of Cu with ascorbic acid compared with the analogous Fe reaction (k = 1.1 × 10^{-19} cm^3 s^{-1}). Quinones do not contribute substantially to ROS production due to much lower ambient and ELF concentrations and lower rate coefficients (~10^{-21}–10^{-19} cm^3 s^{-1}). In terms of size dependence, ROS production rates by Cu and Fe are mostly contributed to by coarse particles with particle sizes larger than 1 µm, while SOA and quinones have a broader distribution with more contribution from fine particles smaller than 1 µm (PM_1). Larger particles dominate the contribution to ROS production in the extrathoracic region, mainly driven by the effective deposition of larger particles in the upper respiratory tract.

Figure 13A shows the modeled contributions of different chemical species in generating various ROS in the extrathoracic and alveolar regions. H_2O_2 and $\cdot O_2^-$ family production rates are mostly governed (>90 %) by Cu and Fe. SOA contrib-

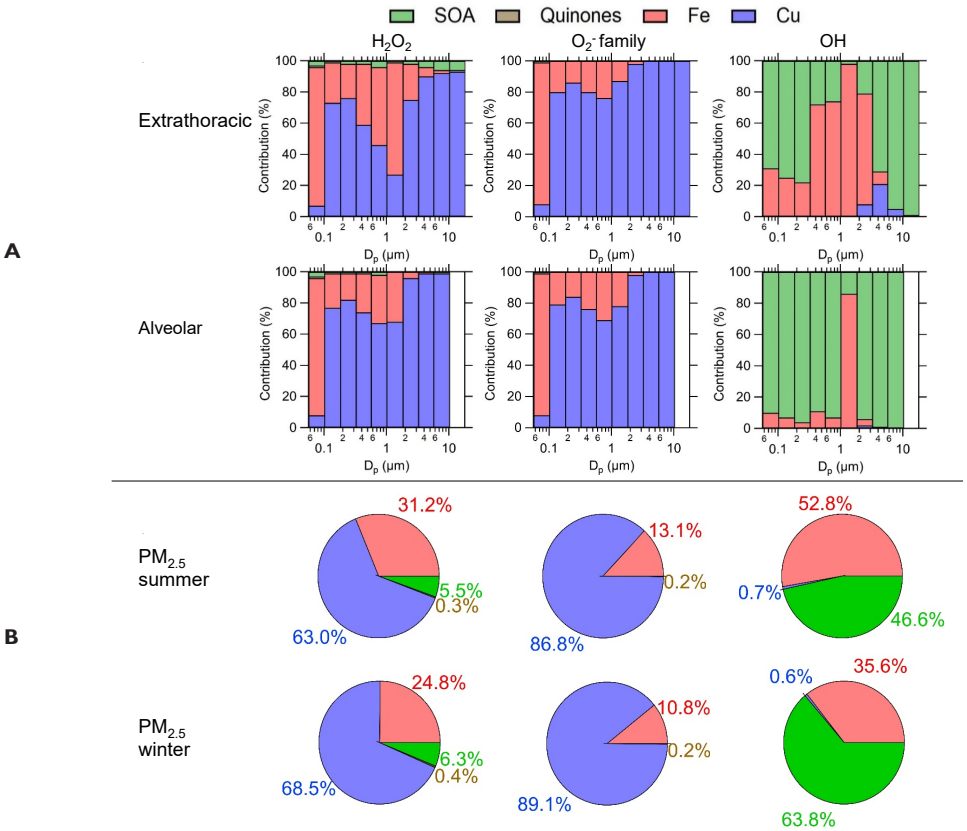

Figure 13. Modeled contributions of Cu, Fe, SOA, and quinones to production rates of H_2O_2, $\cdot O_2^-$ family, and ·OH. A. in the extrathoracic and alveolar regions based on size-dependent deposition of particles collected at the road-side site and **B**. in the respiratory tract (without considering size-dependent deposition) based on $PM_{2.5}$ particles collected at the urban site in Atlanta in summer and winter. Reprinted with permission from Fang et al. 2019. Copyright 2019 American Chemical Society.

ute a very small fraction (<10%) to H_2O_2, and its contribution to the $\cdot O_2^-$ family is negligible. The relative importance of Cu and Fe depends highly on particles sizes: at larger sizes, Cu contributes the most, whereas Fe plays a larger role at smaller size ranges. Figure 13B shows average contributions in the respiratory tract without considering particle-size-dependent deposition by $PM_{2.5}$, showing that Cu has the largest contribution to both the H_2O_2 and $\cdot O_2^-$ families, followed by Fe. This also suggests that the role of Fe in ROS production can be underestimated if size-dependent deposition is not considered. Correlations between Cu and H_2O_2 or $\cdot O_2^-$ production rates are strong ($R^2 > 0.90$). The high similarity in chemical sensitivity of H_2O_2 and the $\cdot O_2^-$ family leads to strong correlations between them ($R^2 \geq 0.92$), except in the extrathoracic region where the correlation is moderate ($R^2 = 0.6$). The low correlation in the extrathoracic region may be due to the high contribution of Fe to H_2O_2 generation in this region.

In contrast, OH has a different chemical selectivity from other ROS, as shown by weaker correlations with H_2O_2 and the $\cdot O_2^-$ family (R^2 = 0.25–0.84). ·OH production rates are mainly attributed to SOA and Fe due to decomposition of ROOH and Fenton reactions, respectively. SOA and Fe can be comparably important in generating ·OH. In the extrathoracic region, Fe plays a major role by contributing more than 60% of the ·OH production for the 0.35–3.2 μm size range, while the SOA contribution dominates in smaller and larger particles (Figure 13A). In the alveoli, SOA contribute most of the ·OH production except for the 1–1.8 μm size range where Fe is responsible for producing more than 80% of ·OH radicals. For overall $PM_{2.5}$ contributions in summer, contributions from Fe and SOA are approximately equal, and SOA show a larger contribution (on average 64%) in winter (Figure 13B). ROS production of SOA may depend on various factors such as precursors and levels of oxidants (i.e., O_3, ·OH, NO_x) upon formation and aging (Chowdhury et al. 2018; Tong et al. 2018). Further experiments are required using SOA formed in a wide range of conditions along with detailed chemical characterization for a better evaluation of ROS activity and toxicity of SOA.

ROS Production Rates vs. OP

Figure 14 shows the comparisons of modeled production rates of H_2O_2, the $\cdot O_2^-$ family, and ·OH with the OP by the DTT and ascorbic acid assays. Modeled $\cdot O_2^-$ family production rates show moderate to strong correlations with OP^{DTT} and OP^{AA} in the extrathoracic (R^2 = 0.76–0.83) and alveolar regions (R^2 = 0.55–0.72). Correlations to chemical species show that both the $\cdot O_2^-$ family production rates and OP^{DTT} correlate well with quinones and Cu in the extrathoracic region. In the alveolar region $\cdot O_2^-$ family production rates only correlate with Cu (R^2 = 0.99), while OP^{DTT} correlates mainly with organic species (R^2 = 0.69).

Moderate to strong correlations of $\cdot O_2^-$ family production rates with OP^{DTT} and OP^{AA} are also found for $PM_{2.5}$ samples in summer (R^2 = 0.69 and 0.49 for OP^{DTT} and OP^{AA}, respectively), whereas the correlation is weaker in winter (R^2 = 0.27 and 0.32 for OP^{DTT} and OP^{AA}, respectively). The $\cdot O_2^-$ family production is mainly governed by Cu and Fe via metal redox chemistry converting O_2 to $\cdot O_2^-$. Organics contribute little for all sizes or ELF regions due to low ELF concentrations of quinones and low $\cdot O_2^-$ production of SOA. OP^{DTT} in the alveolar region is dominated by accumulation-mode organic species (Fang et al. 2017b). $\cdot O_2^-$ production rates correlate better with OP in the extrathoracic region than in the alveolar region.

H_2O_2 shows a strong correlation with OP, as H_2O_2 is mainly produced by $\cdot O_2^-$ reacting with various species including quinones, Fe, Cu, and ascorbic acid, as well as by decomposition of certain species (e.g., hydroxyhydroperoxides) in SOA (Wang et al. 2011b). Previous studies have also found correlations of OP with H_2O_2 production rates for quinones and metal ions (Xiong et al. 2017), as well as for laboratory-generated SOA (Tong et al. 2018). In the extrathoracic region, correlations of H_2O_2 with OP measures (R^2 = 0.43 and 0.36 for OP^{DTT} or OP^{AA}, respectively) are much lower than those for the $\cdot O_2^-$ family (R^2 = 0.76 and 0.83 for OP^{DTT} or OP^{AA}, respectively). These weaker correlations may be due to a low activity of Fe in the DTT and ascorbic acid assays, whereas Fe is effective in H_2O_2 generation.

In contrast, ·OH production rates do not show strong correlations with OP^{DTT} or OP^{AA} (R^2 = 0.08–0.55). The lack of correlation between OH production rates and OP measures is consistent with low correlations of ·OH with $\cdot O_2^-$ and H_2O_2 production rates. ·OH radicals are mainly generated by SOA through decomposition of ROOH and Fenton reactions of Fe with H_2O_2 (·OH production rates are strongly associated with Fe [$R^2 \geq 0.90$]). Since the DTT and ascorbic acid assays are less sensitive to Fe ($R^2 < 0.4$) (Fang et al. 2016), ·OH and OP correlations become stronger when removing high-Fe data points (R^2 increases from below 0.32 to 0.53–0.76). This suggests that organic compounds may contribute to both ·OH production and OP, which is consistent with a recent study finding that ROOH can consume DTT (Jiang and Jang 2018).

In winter, OP^{DTT} is mainly driven by organic species as shown by the strong correlation with quinones and SOA (R^2 = 0.81) and the moderate to weak correlation with Cu and Fe ($R^2 < 0.35$). In winter, biomass burning is a major PM source in Atlanta with a high abundance of aromatics or HULIS (Fang et al. 2016); previous studies have shown that HULIS plays an important role in DTT decay and $\cdot O_2$ production (Lin and Yu 2011; Verma et al. 2015b). HULIS concentrations are at much higher levels in winter than in summer, due to high levels of biomass burning in winter in the southeastern United States. Estimated HULIS concentrations were implemented into the KM-SUB-ELF model, assuming that HULIS would have a similar or one order of magnitude higher $\cdot O_2^-$ generating capability than quinones. With this estimation the correlation between OP^{DTT} and the model $\cdot O_2^-$ family, as well as H_2O_2 production rate in winter, improves substantially (R^2 increases from ~0.3 to 0.4–0.7), supporting the hypothesis that HULIS are the missing sources of ROS production in the model. This

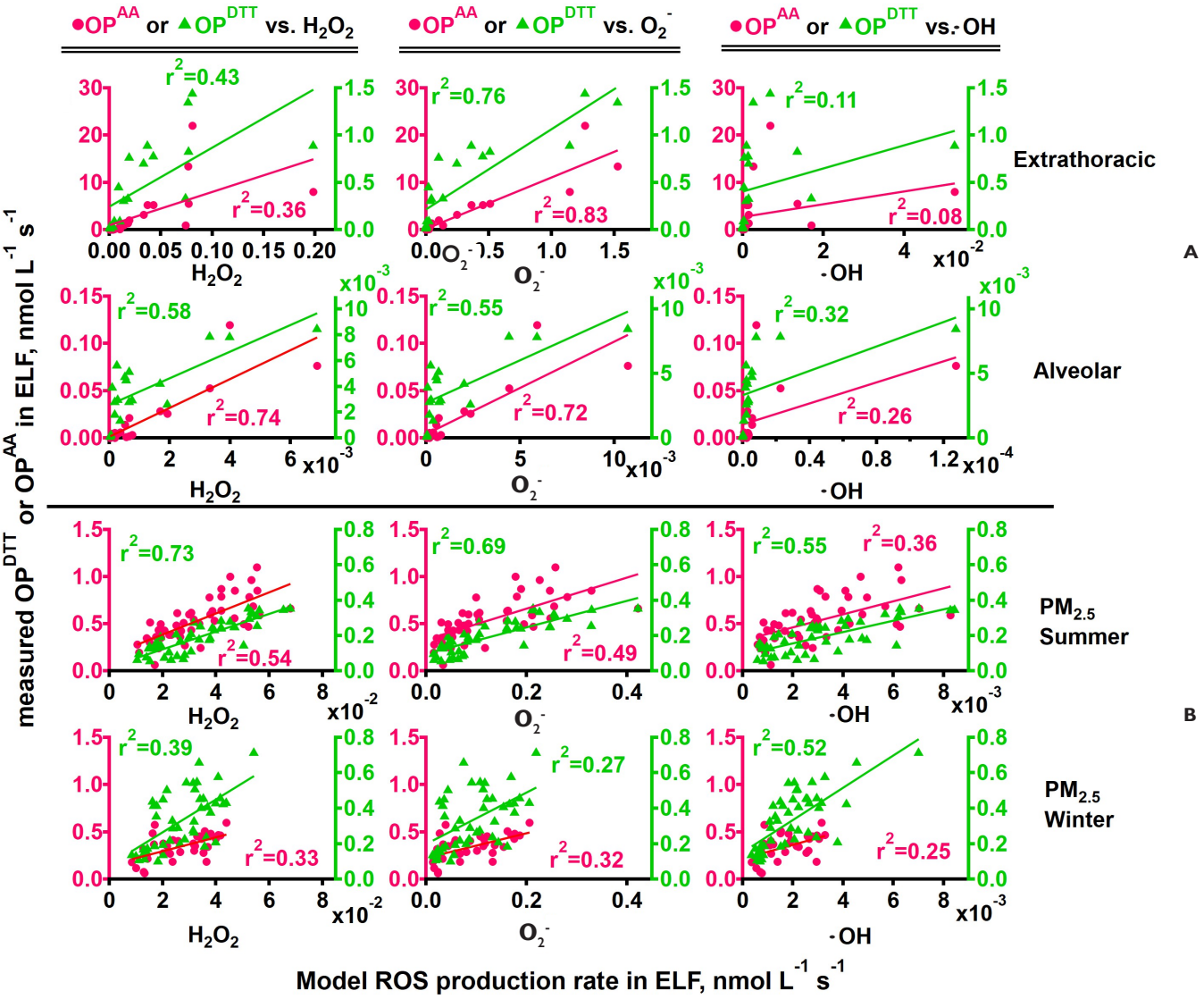

Figure 14. Correlations between oxidative potential measured by the dithiothreitol (OPDTT) and ascorbic acid (OPAA) assays and H_2O_2, the $\cdot O_2^-$ family, and ·OH production rates. A. by size-dependent respiratory deposition of the size-segregated particles collected from both road-side and urban sites in extrathoracic and alveolar regions and **B**. by respiratory deposition of $PM_{2.5}$ particles collected at the urban site in summer and winter in the total ELF. Reprinted with permission from Fang et al. 2019. Copyright 2019 American Chemical Society.

exercise also suggests the potential use of brown carbon measurements to estimate ROS generation from HULIS activities. In fact, brown carbon shows strong correlations with measured 1,4-naphthoquinone (R^2 = 0.84) and moderate correlations with 1,2-naphthoquinone (R^2 = 0.47), two of the three ROS-generating quinones species. Recent studies have shown that ROS formation and the OP of HULIS can be altered significantly upon complex formation with metals (Gonzalez et al. 2017; Wei et al. 2019) or in the presence of pyridine, imidazole, and their alkyl derivatives (Dou et al. 2015). Other potential chemical species affecting ROS generation but not included in the model are peroxyacyl nitrates and electron-deficient alkenes (Jiang and Jang 2018). Further laboratory experiments and implementation into the model are required to evaluate the impact of ROS generation by these species.

CELLULAR VS. CHEMICAL ROS IN ELF

Figure 15A and B show the measured temporal evolution of control-corrected chemical and cellular $\cdot O_2^-$ production rates upon exposure to PQN and isoprene-derived SOA, respectively. Cellular $\cdot O_2^-$ production rate increased to ~0.4 μM min^{-1}

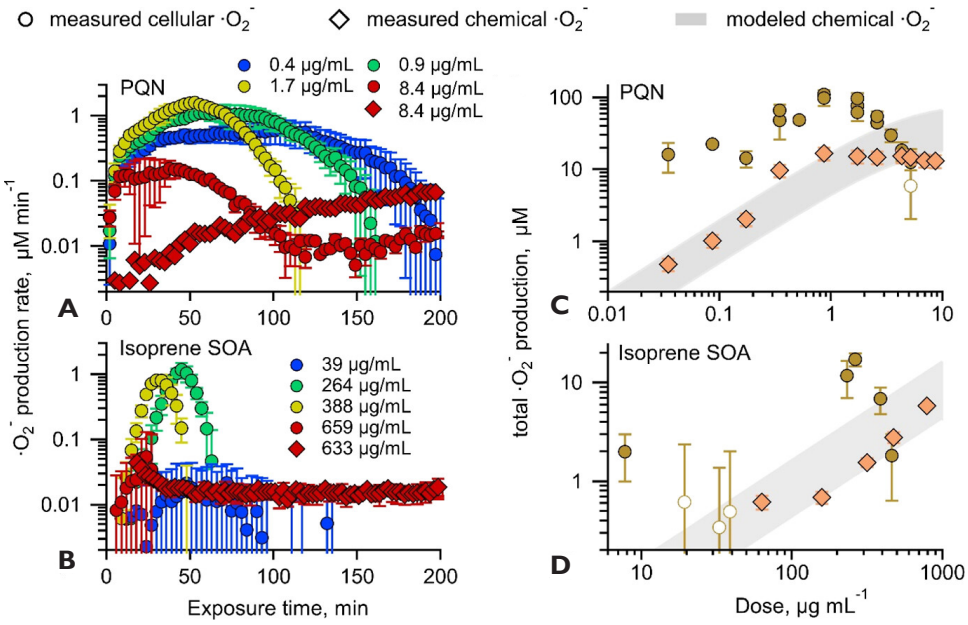

Figure 15. Total $\cdot O_2^-$ production upon exposure to PQN and isoprene-derived SOA. Cellular $\cdot O_2^-$ release from RAW264.7 macrophages (circles) and chemical (diamonds) is shown in time profiles (A, B) and in dose–response curves (C, D). **A & B.** Markers are color-coded with dose (in g/mL). Data points with error bars represent the average and uncertainties calculated from error propagation based on variabilities from samples and controls (see Statistical Analyses section for details). **C & D.** Statistically insignificant ($P > 0.05$, unpaired *t* test) comparisons of exposure groups with vehicle controls are plotted as open circles. Chemical production of $\cdot O_2^-$ was also simulated using kinetic models with shaded areas representing model uncertainties. Adapted from Fang et al. 2022.

when exposed to 0.4 µg mL^{-1} of PQN. With increased doses of 0.9 and 1.7 µg mL^{-1}, cellular $\cdot O_2^-$ production rates increased and reached maximum at ~1 µM min^{-1} after ~50 minutes, followed by decreases over time. At a higher dose of 8.4 µg mL^{-1}, macrophages responded faster to reach a lower peak at ~0.2 µM min^{-1} at 40 minutes and decreased more swiftly afterward. At all doses, cellular $\cdot O_2^-$ production rates eventually decreased to the level observed for controls with ~0.1 µM min^{-1}, which may be regulated by mitochondrial respiration (Winterbourn 2008). In the absence of cells, PQN triggered redox reactions to produce $\cdot O_2^-$ increasingly to reach ~0.1 µM min^{-1} over a few hours. While relatively low doses of PQN stimulate macrophages for $\cdot O_2^-$ release for a few hours, much higher doses of isoprene SOA are required for $\cdot O_2^-$ release, which lasts less than 1 hour. With doses of isoprene SOA increasing from 264 µg mL^{-1} to 388 µg mL^{-1}, cellular $\cdot O_2^-$ production rates reached their peaks above ~1 µM min^{-1} and decreased to control levels earlier in time with a faster cellular response at higher doses. At the very high dose of 659 µg mL^{-1}, the peak cellular $\cdot O_2^-$ release rate is comparable to the chemical $\cdot O_2^-$ production rate of ~0.05 µM min^{-1} via aqueous reactions of SOA components in the absence of cells.

The dose–response relationships are shown in Figure 15C and D, where responses are given as total $\cdot O_2^-$ production as obtained from the integration of control-corrected $\cdot O_2^-$ production rates over exposure time. The measured chemical total $\cdot O_2^-$ production increased with an increase of dose. PQN generates $\cdot O_2^-$ via redox-cycling reactions with antioxidants (D'Autréaux and Toledano 2007; Lakey et al. 2016), while isoprene-derived SOA yields $\cdot O_2^-$ via a series of aqueous reactions including decomposition of α-hydroxyperoxyl radicals and ROOH, as well as ·OH oxidation of primary or secondary alcohols (Wei et al. 2021b). We applied kinetic models that include these chemical mechanisms to simulate chemical $\cdot O_2^-$ production (Lakey et al. 2016; Wei et al. 2021b), producing consistent results as the measurements (shaded areas).

Interestingly, cellular $\cdot O_2^-$ release induced by PQN and isoprene-derived SOA shows inverted U-shaped dose–response distributions. Under low doses, macrophages release $\cdot O_2^-$ under regular cellular metabolisms with a control level of ~23 µM, which is comparable to or higher than the chemical $\cdot O_2^-$ production. Once the dose reaches a threshold, macrophages are activated and cellular total $\cdot O_2^-$ production increases sharply, dominating over chemical $\cdot O_2^-$ production. The onset dose of cell activation for PQN (~0.2 µg mL^{-1}) is much lower than isoprene-derived SOA (>40 µg mL^{-1}), indicating that macrophages are more sensitive to PQN than isoprene-derived SOA in producing ROS. This suggests that quinones are intrinsically more toxic than isoprene-derived SOA, consistent with previous studies that show anthropogenic aromatics have higher toxicity compared with biogenic aerosols (Offer et al. 2022; Tuet et al. 2017a,b).

Cellular $\cdot O_2^-$ production induced by PQN and isoprene-derived SOA then decreased at higher doses, surpassed by chemical $\cdot O_2^-$ production. The decreases of cellular $\cdot O_2^-$ release at higher doses (Figure 15C and D) and longer exposure time (Figure 15A and B) are not due to cell death. Cell cytotoxicity measurements show that cells exposed to doses of up to 5 μg mL^{-1} for PQN and 923 μg mL^{-1} for isoprene SOA have fluorescence signals similar to that of filter blanks (fresh filter without particle collection) (unpaired *t* test, $P > 0.05$). These signals were much lower than those from the positive control lysed cells ($P < 0.05$), confirming that cells are alive during the whole course of exposure. Instead, the decreased cellular release of $\cdot O_2^-$ is most likely due to redox homeostasis by cells upregulating the antioxidant response elements to scavenge ROS for protection against proinflammatory effects (Droge 2002). Previous studies have found that antioxidant enzymes can be upregulated by the transcription factor Nrf2 when oxidative stress is induced upon exposure to ambient and diesel exhaust PM containing polycyclic aromatic hydrocarbons and quinones (Gurgueira et al. 2002; Li et al. 2004; Pardo et al. 2020).

Note that cell cytotoxicity measurements also imply that the range of doses applied in this study are reasonable. The conversion of doses to ambient PM concentrations is highly complex as respiratory deposition is largely affected by the nature of breathing (nasal vs. oral, tidal volume, and frequency), individual differences in lung anatomy, the airflow patterns in the lung airways, and the presence of deposition hotspots in the lung (Porra et al. 2018). Phalen and colleagues (2006) demonstrated by dosimetry model predictions that the surface PM deposition can reach up to 85.5 μg cm^{-2} but vary by up to three orders of magnitude in the tracheobronchial region. With a bottom area of 0.32 cm^2 and a working volume of 0.2 mL of a 96-well plate, the surface doses for SOA and PQN in the current study are 5–412 μg cm^{-2} and 0.02–5.3 μg cm^{-2}, respectively. Combining all the uncertainties and variabilities (up to four orders of magnitude), and also considering that the surface area of the alveolar region is about 200 times larger and the deposition in the alveolar region is up to 3 fold higher than in the tracheobronchial region (Vicente et al. 2021), the applied surface doses are within relevant ranges for real-life exposure scenarios and are consistent with the doses applied in previous submerged cell exposure studies.

We then applied cellular imaging techniques to study the mechanism of cellular $\cdot O_2^-$ release and its impacts on cell membranes. Selected doses that activate massive cellular $\cdot O_2^-$ release were used for exposure. In the Phasor-FLIM method, the NAD(P)H fluorescence lifetime is visualized in polar coordinates by calculating the Fourier sine and cosine transformation of the FLIM photon histogram curve (Digman et al. 2008). The cell membranes and cytoplasm mainly fall along a metabolic trajectory represented by a line joining positions of free NAD(P)H and protein-bound NAD(P)H on a phasor plot (**Figure 16A**) (Digman et al. 2008; Stringari et al. 2012). The relative locations on the trajectory can be used to obtain the bound NAD(P)H fractions (Figure 16B). Macrophages exposed to PQN and isoprene-derived SOA show lower bound NAD(P)H fractions than the controls, indicating that the bound state NADPH is oxidized to nonfluorescent $NADP^+$, releasing superoxide: $NADPH + 2O_2 \rightarrow NADP^+ + H^+ + 2\cdot O_2^-$ (Cross and

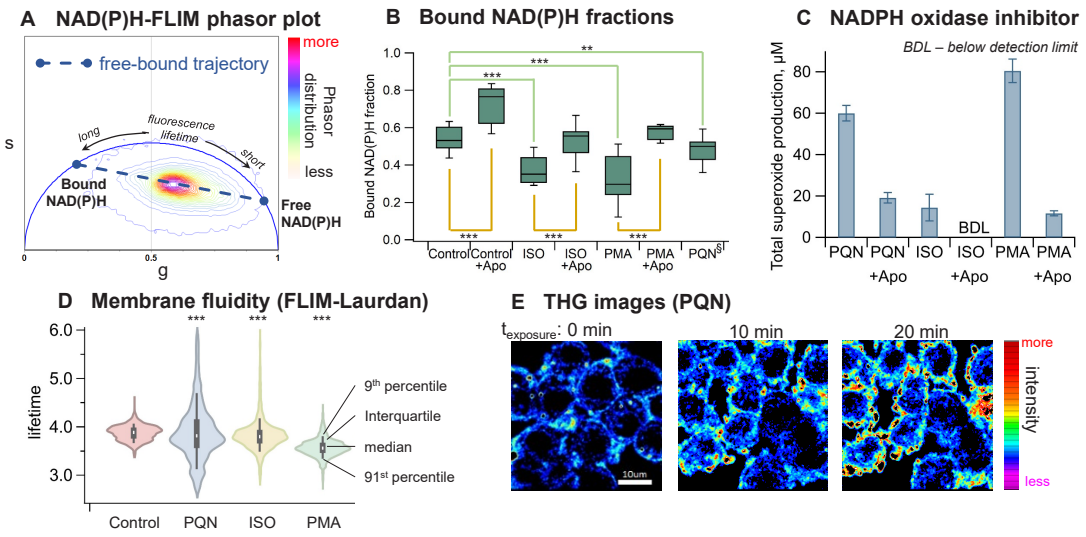

Figure 16. NADPH oxidase activities and oxidative stress on cell membranes. A. Phasor plot of the FLIM images from RAW 264.7 macrophage treated with control (vehicle) and all samples. **B.** NAD(P)H bound fractions based on phasor locations in A for macrophage treated with control and samples with and without NADPH oxidase inhibitor apocynin (Apo). The box plots show the median, 10, 25, 75, and 90 percentiles. **C.** Effect of apocynin on total $\cdot O_2^-$ production. Bars with error bars represent the average from triplicates and the standard deviation. **D.** Membrane fluidity measured with FLIM with a Laurdan probe. **E.** Locations and intensity of lipid accumulation from THG imaging on cells treated with 9,10-phenanthrenequinone (PQN). Unpaired *t* test, $***P < 0.0001$, $** P < 0.001$. §FLIM images were taken from cells after 10-min exposure of PQN, washed with PBS buffer, and replaced with fresh incomplete media. BDL = below detectable limit; ISO = isoprene-derived SOA; PMA = phorbol 12-myristate 13-acetate. Adapted from Fang et al. 2022.

Segal 2004; Wientjes and Segal 1995). A bound-to-free shift of NAD(P)H is observed upon exposure to PMA, commonly used as an inducer to activate NADPH oxidase and increase endogenous $\cdot O_2^-$ production. Additionally, apocynin (or Apo), a specific NADPH oxidase inhibitor, results in higher bound NAD(P)H fractions in cells than those without the inhibitor (Figure 16B). Consequently, apocynin reduces cellular $\cdot O_2^-$ production substantially upon exposure to PQN, isoprene-derived SOA, and PMA (Figure 16C). These observations strongly indicate that PQN and isoprene-derived SOA trigger cellular $\cdot O_2^-$ production mainly through activating the NADPH oxidase.

To investigate the impact of generated $\cdot O_2^-$ on cell membranes, we used the emission spectrum of a solvatochromic probe, Laurdan, which is incorporated into the hydrophobic phase in the membrane (Golfetto et al. 2013). Since Laurdan dye adheres mostly to cell membranes, only the fluorescence signals from cell membranes were selected for fluorescence lifetime calculations. A total of 15 cells from each sample were averaged and presented as violin plots in Figure 16D. We observed significant decreases in the fluorescence lifetimes of the Laurdan probe on cell membranes from macrophages exposed to PQN, isoprene SOA, and PMA, which indicates that these samples cause an increase in membrane fluidity, an important parameter in membrane integrity and cell health. In addition, the THG microscopy imaging shows that 10–20 minutes of exposure to PQN causes an increase of THG signal around cell membranes, suggesting the accumulation of lipids (Figure 16E). Bright-field cell images also suggest that macrophages may have taken up oxidized low-density lipoprotein-forming foam cells, a key event suggested to involve the activation of NADPH oxidase observed in previous studies (Aviram et al. 1996; Forman and Torres 2001). Therefore, with the revealing of increased membrane fluidity and laden lipids around the cell membranes, we suggest that macrophages are undergoing lipid peroxidation caused by $\cdot O_2^-$ or other ROS produced thereafter.

DISCUSSION AND CONCLUSIONS

In this project, we aimed to investigate the chemical mechanism and formation kinetics of ROS by SOA in the ELF and also to quantify the relative importance of ROS formation by chemical reactions and macrophages. We generated SOA particles using a reaction chamber and collected ambient PM next to major highways and at an urban site during wildfire events. The collected particles on filters were extracted, and the generated ROS was quantified using EPR spectroscopy with a spin-trapping technique. Kinetic modeling was applied for the analysis and interpretation of experimental data. PM OP was also quantified using the DTT assay. Finally, we quantified cellular and chemical superoxide generation by representative anthropogenic and biogenic PM components using a chemiluminescence assay combined with EPR spectroscopy as well as kinetic modeling. We also applied cellular imaging techniques to study the cellular mechanism of superoxide release and oxidative damage on cell membranes.

Our work elucidates ROS generation pathways from aqueous reactions of biogenic SOA. Multigenerational atmospheric oxidation and autoxidation of biogenic VOCs by ·OH and O_3 leads to the formation of HOM and ELVOC (Bianchi et al. 2019; Ehn et al. 2014). Most of these compounds contain alcohol and hydroperoxide functional groups. After condensation into the particle phase, a fraction of ROOH decomposes to form ·OH, which can act as an ignition step for a cascade of ROS formation pathways. The e-folding times for the ROOH decomposition are estimated to be 4–30 hours, which represent average lifetimes for different ROOH compounds; some of them may have shorter timescales (Krapf et al. 2016; Pospisilova et al. 2020), while others may be very stable (Kenseth et al. 2018; Zhang et al. 2017). This decomposition process can be accelerated by photolysis (Badali et al. 2015; Epstein et al. 2014) and Fenton-like reactions of transition metal ions (Fang et al. 2020; Tong et al. 2016, 2017).

While a recent study (Zhang et al. 2017) found that the PAM-reactor-generated α-pinene SOA contain substantial amounts of particle-phase HOM, consistent with the gas-phase measurements in previous studies (Ehn et al. 2012, 2014; Kirkby et al. 2016), we acknowledge a caveat of this work that the particle mass concentrations in the PAM reactor are much higher compared with ambient conditions, leading to more prominent condensation of semi-volatile organic compounds. While this study serves as a proof of concept and provides mechanistic insights into possible mechanisms of ROS formation, future studies are warranted to investigate the ROS formation from SOA generated under atmospherically relevant conditions. Higher oxidant and precursor concentrations would increase the chance of $RO_2\cdot$ to react with each other to form ROOR. With lower concentrations in the ambient atmosphere, $RO_2\cdot$ would favorably react with $HO_2\cdot$ to form ROOH, which would increase the ROS formation potential of SOA.

·OH radicals released by ROOH decomposition can abstract hydrogen from primary or secondary alcohols ($R_1R_2CH(OH)$) to form α-hydroxyalkyl radicals, which quickly react with dissolved O_2 to form α-hydroxyperoxyl radicals. Within milliseconds α-hydroxyperoxyl radicals can undergo unimolecular decomposition to form $\cdot O_2^-/HO_2\cdot$ radicals. Through $HO_2\cdot$ termination, α-hydroxyperoxyl radicals form α-hydroxyalkyl hydroperoxides, which can decompose to generate H_2O_2, another important ROS (Qiu et al. 2020a; Sauer et al. 1999). Other feasible pathways of H_2O_2 formation by SOA have also been discussed in the literature, including hydrolysis of diacyl peroxides or peroxy acids (Ziemann 2002). The relative contributions of different H_2O_2 sources still warrant further studies.

The aqueous phase chemical reactions that generate ROS are affected by pH. Inhalation and deposition of organic aerosols can lead to oxidative stress by the formed ROS at physiological

pH. Under neutral conditions organic hydroperoxides can preferably undergo unimolecular decomposition to generate highly reactive ·OH radicals, which can initiate a cascade of reactions to propagate further radical formation (Gligorovski et al. 2015), as well as to directly attack biological components and induce pathological processes such as lipid peroxidation (Yin et al. 2011). The formed organic radicals can be persistent even in the presence of antioxidants (Wei et al. 2021a), although their capacity in causing OP still warrants further studies. Our work then establishes the mechanisms driving organic radical formation by the interactions between SOA and Fe^{2+} in the ELF. While ROOR are thermally stable under physiological temperature (Sanchez and Myers 2004), the chemical lifetimes of ROOR with respect to Fe^{2+} reactions were calculated to be 0.3–46 hours, depending on Fe^{2+} concentrations in the experimental range of 0.05–0.8 mM. Meanwhile, the antioxidant defense system can counteract ROS formation: for example, ascorbate efficiently scavenges ·OH and $\cdot O_2^-/HO_2\cdot$ (Adams et al. 1965; Nadezhdin and Dunford 1979). In comparison, organic radicals, especially R·, react with ascorbate more slowly by multiple orders of magnitude, leading to much longer lifetimes (Buettner and Jurkiewicz 1996). A recent study found that the reaction rates of ascorbate and glutathione with alkyl radicals are too slow to protect proteins from peroxidation (Nauser and Gebicki 2017). The rapid redox cycling of Fe^{3+}/Fe^{2+} maintained by ascorbate can further facilitate the ROOR decomposition and subsequent organic radical formation. Note that Fe^{3+}/Fe^{2+} redox cycles can also be mediated by ROS such as superoxide (Gonzalez et al. 2017; Voelker and Sedlak 1995), which can be hindered by the addition of antioxidants through direct scavenging of ROS. Antioxidants play a reciprocal role by depleting short-lived reactive radicals while amplifying organic radical formation. While this study used synthetic ELF containing lung antioxidants, future studies may apply alternative approaches using appropriately concentrated components to represent true ELF concentrations or bronchoalveolar lavage fluid from healthy and diseased participants.

We found that a variety of radicals are generated by ambient PM collected in the Los Angeles Basin. Highway PM mainly generate ·OH, while wildfire PM mainly generate R· and ·OH, with minor contributions from superoxide and RO·. Evaluating the representativeness of the PM investigated in this project requires further studies of PM collected from different locations in the United States and around the world. OP-DTT is found to be high in wildfire PM, exhibiting little correlation with radical forms of ROS, which are in stark contrast with highway PM that correlate well with OP-DTT. The relation between OP and ROS formation is highly complex. Various acellular OP assays (e.g., ascorbic acid and glutathione) and cellular assays should be applied to conduct a comprehensive evaluation of PM OP (Shahpoury et al. 2022). In addition, for complete ROS quantification and robust intercomparison with PM OP, different methods of ROS measurements should be applied, and ROS that were not measured in this study, such as singlet oxygen and peroxy nitrite, should also be quantified.

Epithelial cell membranes contain phospholipid bilayers, and ·OH and $HO_2\cdot$ are known to initiate a cascade of propagation reactions known as lipid peroxidation (Ayala et al. 2014; Yin et al. 2011), which may alter the membrane fluidity and trigger the inactivation of membrane-embedded proteins functioning as ion channels and receptors (Los and Murata 2004). Our results on the persistency of organic radicals even in the presence of antioxidants imply that organic radicals may also participate in radical chain reactions involved in lipid peroxidation. Despite the significance in numerous pathological processes, lipid peroxidation has not been linked mechanistically to radical formation from organic aerosols and transition metals, which underlines the need for future studies. Overall, our experimental and modeling results demonstrate the central role of Fe^{2+} in inducing organic radical formation by facilitating ROOR decomposition in lung fluid, which highlights the significance of the interactions among redox-active components in ambient PM in potentially causing oxidative stress.

A novel aspect of our modeling study is the derivation of production rates of different types of ROS in the ELF, based on ambient measurements of redox-active chemical components, for comparison with OP measurements. For both the size-segregated data in different respiratory regions and $PM_{2.5}$ in different seasons, OP shows strong correlations with modeled $\cdot O_2^-$ family and H_2O_2 production rates in the ELF, but not with ·OH production rates. These correlations can be explained by the major chemical species that contribute to ROS production and DTT/ascorbic acid loss. The correlations are consistent with the fact that the rate-limiting step for $\cdot O_2^-$ and H_2O_2 is the reaction between antioxidants and redox-active components, while that for ·OH is Fenton and Fenton-like reactions or SOA decomposition without involving antioxidants. Direct measurements of ROS in the ELF or in its surrogate are currently lacking, which needs to be addressed in future studies for more robust comparisons with OP measurements.

Figure 17 summarizes multitier chemical and cellular response mechanisms in SOA exposure in ELF. At low doses or early exposure, $\cdot O_2^-$ is mainly produced from normal cellular metabolism via mitochondrial respiration with minor contributions from chemical reactions. After a threshold dose to macrophages, NADPH oxidase activities are upregulated for respiratory burst, releasing massive amounts of $\cdot O_2^-$, which can cause oxidative stress by increasing cell membrane fluidity through lipid peroxidation. Further increases of doses or exposure time leads to the activation of antioxidant response elements, reducing the net cellular $\cdot O_2^-$ production. Chemical $\cdot O_2^-$ production may become comparably important at very high doses, especially if escalation of oxidative stress leads to cell death. Given that cellular $\cdot O_2^-$ release mostly dominates over its chemical production by PM-reactive and redox-active components, widely applied acellular assays that measure OP and ROS activity may need to be interpreted with caution. Note that alveolar macrophages reside primarily in alveoli, so chemical ROS should still be relevant for causing oxidative stress in the upper respiratory tract, including the extrathoracic and bronchial regions.

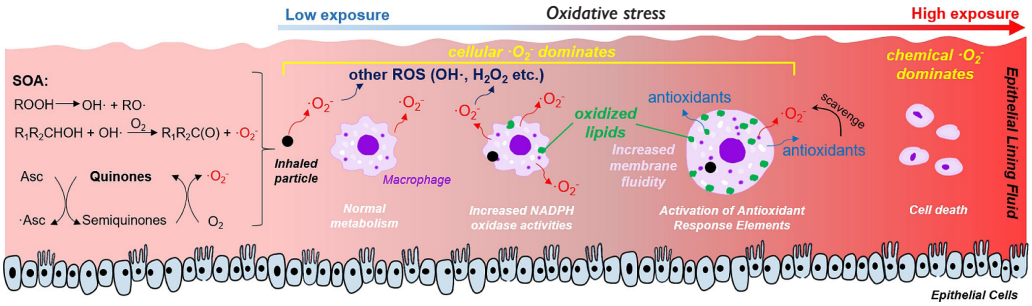

Figure 17. Multitier chemical and cellular response mechanisms upon PM deposition in epithelial lining fluid. Cellular $\cdot O_2^-$ release by alveolar macrophages via activation of NADPH oxidase dominates over chemical $\cdot O_2^-$ production, causing lipid peroxidation and activation of antioxidant response elements. Adapted from Fang et al. 2022.

Future studies should be extended to include other chemical compounds that have high OP and redox activity, such as transition metals; the presence of metals in ambient PM might enhance the importance of chemical ROS (Charrier and Anastasio 2012; Fang et al. 2019; Guo et al. 2019; Shirmohammadi et al. 2015). In this study, we used RAW 264.7 macrophages as an established cell line for studying the oxidative stress responses of macrophages. Other immortalized alveolar cell lines such as NR8383, MH-S, THP-1, and also primary alveolar macrophages may need to be used to confirm and to strengthen the findings of this project. While current work is based on the standard submerged cell culture method, this classical condition should be extended to represent more realistic conditions with multiple types of cells, including macrophages and endothelial cells, to simulate synthetic interactions between cell populations (Li et al. 2002) with an application of the air-liquid interface for simulating exposure and respiratory deposition of aerosol particles (Offer et al. 2022).

The knowledge on ROS formation by PM obtained in this project and the developed kinetic model can provide useful metric (i.e., ROS levels in lung lining fluid) to epidemiological studies. We applied the KM-SUB-ELF model to estimate ROS concentrations in ELF by using measured ambient concentrations of Fe and Cu. Their concentrations in the ELF can be estimated using their ambient concentrations, their fractional solubilities, breathing rate, PM deposition rate, and total ELF volume. Then, the KM-SUB-ELF model estimated ROS generation in human respiratory tract by resolving mass transport and chemical reactions between lung antioxidants and Fe and Cu ions. The estimated ELF concentrations were found to have positive associations with respiratory diseases (Zhang et al. 2021), cardiovascular diseases (Zhang et al. 2020), and COVID-19 incidences (Stieb et al. 2021), strongly indicating the connection between oxidative stress in lungs and various adverse health outcomes.

In conclusion, the mechanistic understandings and quantifications of ROS formation obtained in this project provide a basis for further elucidation of adverse health effects and oxidative stress upon respiratory deposition of $PM_{2.5}$. For a comprehensive assessment of PM toxicity and health effects via oxidative stress, we demonstrated that it is important to consider both chemical reactions and cellular processes for the formation of ROS upon respiratory deposition. Chemical composition of PM strongly influences ROS formation triggered by PM; thus, further investigations are required that will study ROS formation from various PM components such as different types of carbonaceous aerosols, inorganic components, and metals emitted from a variety of sources including transportation (tailpipe and nontailpipe emissions), fossil fuel combustion, industrial and agricultural activities, and biomass burning. Such research will provide critical information to environmental agencies and policymakers for the development of air quality policy and regulation.

ACKNOWLEDGMENTS

Research described in this report was conducted under contract to the HEI (RFA 17-3), an organization jointly funded by the U.S. Environmental Protection Agency (Assistance Award No. CR–83998101) and certain motor vehicle and engine manufacturers. The contents of this article do not necessarily reflect the views of HEI, or its sponsors, nor do they necessarily reflect the views and policies of the U.S. Environmental Protection Agency or motor vehicle and engine manufacturers. We thank our collaborators including William Brune, Rodney Weber, Heejung Jung, Xiaoliang Wang, Cynthia Wong, Katherine Hopstock, Haijie Tong, Steven Lelieveld, Thomas Berkemeier, and Ulrich Pöschl, as well as all coauthors on manuscripts stemmed from this project.

REFERENCES

Abbas AK, Lichtman AH, Pillai S. 2010. Basic immunology. Functions and Disorders of the Immune system.Philadelphia, PA:Saunders Elsevier.

Adams G, Boag J, Currant J, Michael B. 1965. Absolute Rate Constants for the Reaction of the Hydroxyl radical with Organic Compounds. New York:Academic Press.

Alpert PA, Dou J, Corral Arroyo P, Schneider F, Xto J, Luo B, et al. 2021. Photolytic radical persistence due to anoxia in viscous aerosol particles. Nat Commun 12:1769.

Anderson GH, Smith JG. 1968. Acid-catalyzed rearrangement of hydroperoxides. II. Phenylcycloalkyl hydroperoxides. Can J Chem 46:1561–1570.

Arangio AM, Tong H, Socorro J, Pöschl U, Shiraiwa M. 2016. Quantification of environmentally persistent free radicals and reactive oxygen species in atmospheric aerosol particles. Atmos Chem Phys 16:13105–13119.

Aviram M, Rosenblat M, Etzioni A, Levy R. 1996. Activation of NADPH oxidase is required for macrophage-mediated oxidation of low-density lipoprotein. Metabolism 45:1069–1079.

Ayala A, Muñoz MF, Argüelles S. 2014. Lipid peroxidation: Production, metabolism, and signaling mechanisms of malondialdehyde and 4-hydroxy-2-nonenal. Oxid Med Cell Longev 2014:360438.

Badali KM, Zhou S, Aljawhary D, Antiñolo M, Chen WJ, Lok A, et al. 2015. Formation of hydroxyl radicals from photolysis of secondary organic aerosol material. Atmos Chem Phys 15:7831–7840.

Bateman AP, Nizkorodov SA, Laskin J, Laskin A. 2011. Photolytic processing of secondary organic aerosols dissolved in cloud droplets. Phys Chem Chem Phys 13:12199–12212.

Bates JT, Fang T, Verma V, Zeng L, Weber RJ, Tolbert PE, et al. 2019. Review of acellular assays of ambient particulate matter oxidative potential: Methods and relationships with composition, sources, and health effects. Environ Sci Technol 53:4003–4019.

Beck-Speier I, Dayal N, Karg E, Maier KL, Schumann G, Schulz H, et al. 2005. Oxidative stress and lipid mediators induced in alveolar macrophages by ultrafine particles. Free Radic Biol Med 38:1080–1092.

Bedard K, Krause K-H. 2007. The NOX family of ROS-generating NADPH oxidases: Physiology and pathophysiology. Physiol Rev 87:245–313.

Berkemeier T, Ammann M, Krieger UK, Peter T, Spichtinger P, Pöschl U, et al. 2017. Technical note: Monte Carlo genetic algorithm (MCGA) for model analysis of multiphase chemical kinetics to determine transport and reaction rate coefficients using multiple experimental data sets. Atmos Chem Phys 17:8021–8029.

Bianchi F, Kurten T, Riva M, Mohr C, Rissanen MP, Roldin P, et al. 2019. Highly oxygenated organic molecules (HOM) from gas-phase autoxidation involving peroxy radicals: A key contributor to atmospheric aerosol. Chem Rev 119:3472–3509.

Birben E, Sahiner UM, Sackesen C, Erzurum S, Kalayci O. 2012. Oxidative stress and antioxidant defense. World Allergy Organ J 5:1–11.

Bothe E, Schuchmann MN, Schulte-Frohlinde D, Vonsonntag C. 1978. HO_2 elimination from α-hydroxyalkylperoxyl radicals in aqueous-solution. Photochem Photobiol 28:639–644.

Brunekreef B, Holgate ST. 2002. Air pollution and health. Lancet 360:1233–1242.

Buettner GR, Jurkiewicz BA. 1993. Ascorbate free radical as a marker of oxidative stress: An EPR study. Free Radical Biol Med 14:49–55.

Buettner GR, Jurkiewicz BA. 1996. Catalytic metals, ascorbate and free radicals: Combinations to avoid. Rad Res 145:532–541.

Carrasquillo AJ, Daumit KE, Kroll JH. 2015. Radical reactivity in the condensed phase: Intermolecular versus intramolecular reactions of alkoxy radicals. J Phys Chem Lett 6:2388–2392.

Charrier JG, Anastasio C. 2011. Impacts of antioxidants on hydroxyl radical production from individual and mixed transition metals in a surrogate lung fluid. Atmos Environ 45:7555–7562.

Charrier JG, Anastasio C. 2012. On dithiothreitol (DTT) as a measure of oxidative potential for ambient particles: Evidence for the importance of soluble transition metals. Atmos Chem Phys 12:9321–9333.

Charrier JG, Anastasio C. 2015. Rates of hydroxyl radical production from transition metals and quinones in a surrogate lung fluid. Environ Sci Technol 49:9317–9325.

Charrier JG, McFall AS, Richards-Henderson NK, Anastasio C. 2014. Hydrogen peroxide formation in a surrogate lung fluid by transition metals and quinones present in particulate matter. Environ Sci Tech 48:7010–7017.

Charrier JG, McFall AS, Vu KK, Baroi J, Olea C, Hasson A, et al. 2016. A bias in the "mass-normalized" DTT response — An effect of non–linear concentration–response curves for copper and manganese. Atmos Environ (1994) 144:325–334.

Charrier JG, Richards-Henderson NK, Bein KJ, McFall AS, Wexler AS, Anastasio C. 2015. Oxidant production from source-oriented particulate matter — part 1: Oxidative potential using the dithiothreitol (DTT) assay. Atmos Chem Phys 15:2327–2340.

Chen Q, Liu Y, Donahue NM, Shilling JE, Martin ST. 2011a. Particle-phase chemistry of secondary organic material: Modeled compared to measured O:C and H:C elemental ratios provide constraints. Environ Sci Technol 45:4763–4770.

Chen X, Hopke PK, Carter WPL. 2011b. Secondary organic aerosol from ozonolysis of biogenic volatile organic compounds: Chamber studies of particle and reactive oxygen species formation. Environ Sci Technol 45:276–282.

Chevallier E, Jolibois RD, Meunier N, Carlier P, Monod A. 2004. "Fenton-like" reactions of methylhydroperoxide and ethylhydroperoxide with Fe^{2+} in liquid aerosols under tropospheric conditions. Atmos Environ 38:921–933.

Cho AK, Sioutas C, Miguel AH, Kumagai Y, Schmitz DA, Singh M, et al. 2005. Redox activity of airborne particulate matter at different sites in the Los Angeles Basin. Environ Res 99:40–47.

Chowdhury PH, He Q, Lasitza Male T, Brune WH, Rudich Y, Pardo M. 2018. Exposure of lung epithelial cells to photochemically aged secondary organic aerosol shows increased toxic effects. Environ Sci Technol Lett 5:424–430.

Cross AR, Segal AW. 2004. The NADPH oxidase of professional phagocytes–prototype of the NO_x electron transport chain systems. Biochim Biophys Acta 1657:1–22.

Crounse JD, Nielsen LB, Jørgensen S, Kjaergaard HG, Wennberg PO. 2013. Autoxidation of organic compounds in the atmosphere. J Phys Chem Lett 4:3513–3520.

D'Autréaux B, Toledano MB. 2007. ROS as signalling molecules: Mechanisms that generate specificity in ROS homeostasis. Nat Rev Mol Cell Biol 8:813–824.

Daellenbach KR, Uzu G, Jiang J, Cassagnes L-E, Leni Z, Vlachou A, et al. 2020. Sources of particulate-matter air pollution and its oxidative potential in Europe. Nature 587:414419.

Dellinger B, Loninicki S, Khachatryan L, Maskos Z, Hall RW, Adounkpe J, et al. 2007. Formation and stabilization of persistent free radicals. Proc Combust Inst 31:521–528.

Denisov ET, Tumanov VE. 2005. Estimation of the bond dissociation energies from the kinetic characteristics of liquid-phase radical reactions. Russ Chem Rev 74:825–858.

Deno NC, Billups WE, Kramer KE, Lastomirsky RR. 1970. Rearrangement of aliphatic primary, secondary, and tertiary alkyl hydroperoxides in strong acid. J Org Chem 35:3080–3082.

Digman MA, Caiolfa VR, Zamai M, Gratton E. 2008. The phasor approach to fluorescence lifetime imaging analysis. Biophys J 94:L14–L16.

Dikalov SI, Kirilyuk IA, Voinov M, Grigor'ev IA. 2011. EPR detection of cellular and mitochondrial superoxide using cyclic hydroxylamines. Free Rad Res 45:417–430.

Docherty KS, Wu W, Lim YB, Ziemann PJ. 2005. Contributions of organic peroxides to secondary aerosol formed from reactions of monoterpenes with O_3. Environ Sci Technol 39:4049–4059.

Dockery DW, Pope CA, Xu XP, Spengler JD, Ware JH, Fay ME, et al. 1993. An association between air pollution and mortality in 6 United States cities. N Engl J Med 329:1753–1759.

Dou J, Lin P, Kuang B-Y, Yu JZ. 2015. Reactive oxygen species production mediated by humic-like substances in atmospheric aerosols: Enhancement effects by pyridine, imidazole, and their derivatives. Environ Sci Technol 49:6457–6465.

Droge W. 2002. Free radicals in the physiological control of cell function. Physiol Rev 82:47–95.

Dvornikov A, Malacrida L, Gratton E. 2019. The DIVER microscope for imaging in scattering media. Methods Protoc 2:53.

Eames J, Watkinson M. 2001. Catalytic allylic oxidation of alkenes using an asymmetric Kharasch–Sosnovsky reaction. Angewandte Chem Int Ed Engl 40:3567–3571.

Eaton GR, Eaton SS, Barr DP, Weber RT. 2010. Quantitative EPR. Vienna, Austria:Springer Science & Business Media.

Edwards KC, Klodt AL, Galeazzo T, Schervish M, Wei J, Fang T, et al. 2022. Effects of nitrogen oxides on the production of reactive oxygen species and environmentally persistent free radicals from α-pinene and naphthalene secondary organic aerosols. J Phys Chem A 126:7361–7372; doi.10.1021/acs.jpca.2c05532.

Ehn M, Kleist E, Junninen H, Petaja T, Lonn G, Schobesberger S, et al. 2012. Gas phase formation of extremely oxidized pinene reaction products in chamber and ambient air. Atmos Chem Phys 12:5113–5127.

Ehn M, Thornton JA, Kleist E, Sipila M, Junninen H, Pullinen I, et al. 2014. A large source of low-volatility secondary organic aerosol. Nature 506:476-479.

El-Sawalhi MM, Ahmed LA. 2014. Exploring the protective role of apocynin, a specific NADPH oxidase inhibitor, in cisplatin-induced cardiotoxicity in rats. Chem-Biol Interact 207:58–66.

Epstein SA, Blair SL, Nizkorodov SA. 2014. Direct photolysis of α-pinene ozonolysis secondary organic aerosol: Effect on particle mass and peroxide content. Environ Sci Technol 48:11251–11258.

Erben-Russ M, Michel C, Bors W, Saran M. 1987. Absolute rate constants of alkoxyl radical reactions in aqueous solution. J Phys Chem 91:2362–2365.

Fang T, Guo H, Zeng L, Verma V, Nenes A, Weber RJ. 2017a. Highly acidic ambient particles, soluble metals, and oxidative potential: A link between sulfate and aerosol toxicity. Environ Sci Technol 51:2611–2620.

Fang T, Hwang BCH, Kapur S, Hopstock K, Wei J, Nguyen V, et al. 2023. Wildfire particulate matter as a source of environmentally persistent free radicals and reactive oxygen species. Environ Sci Atmos 3:581–594.

Fang T, Huang Y-K, Wei J, Monterrosa Mena JE, Lakey PSJ, Kleinman MT, et al. 2022. Superoxide release by macrophages through NADPH oxidase activation dominating chemistry by isoprene secondary organic aerosols and quinones to cause oxidative damage on membranes. Environ Sci Technol 56:17029–17038; doi.10.1021/acs.est.2c03987.

Fang T, Lakey PSJ, Rivera-Rios JC, Keutsch FN, Shiraiwa M. 2020. Aqueous-phase decomposition of isoprene hydroxy hydroperoxide and hydroxyl radical formation by Fenton-like reactions with iron ions. J Phys Chem A 124:5230–5236.

Fang T, Lakey PSJ, Weber RJ, Shiraiwa M. 2019. Oxidative potential of particulate matter and generation of reactive oxygen species in epithelial lining fluid. Environ Sci Technol 53:12784–12792; doi.10.1021/acs.est.9b03823.

Fang T, Verma V, Bates JT, Abrams J, Klein M, Strickland MJ, et al. 2016. Oxidative potential of ambient water-soluble $PM_{2.5}$ in the southeastern United States: Contrasts in sources and health associations between ascorbic acid (AA) and dithiothreitol (DTT) assays. Atmos Chem Phys 16:3865–3879.

Fang T, Verma V, Guo H, King LE, Edgerton ES, Weber RJ. 2015. A semi-automated system for quantifying the oxidative potential of ambient particles in aqueous extracts using the dithiothreitol (DTT) assay: Results from the Southeastern Center for Air Pollution and Epidemiology (SCAPE). Atmos Meas Tech 8:471–482.

Fang T, Zeng L, Gao D, Verma V, Stefaniak AB, Weber RJ. 2017b. Ambient size distributions and lung deposition of aerosol dithiothreitol-measured oxidative potential: Contrast between soluble and insoluble particles. Environ Sci Technol 51:6802–6811.

Fenton HJH. 1894. LXXIII.— Oxidation of tartaric acid in presence of iron. J Chem Soc Trans 65:899–910.

Finkel T, Holbrook NJ. 2000. Oxidants, oxidative stress and the biology of ageing. Nature 408:239–247.

Forman HJ, Torres M. 2001. Redox signaling in macrophages. Mol Aspects Med 22:189–216.

Forman HJ, Torres M. 2002. Reactive oxygen species and cell signaling. Am J Resp Crit Care Med 166:S4–S8.

Franzi LM, Bratt JM, Williams KM, Last JA. 2011. Why is particulate matter produced by wildfires toxic to lung macrophages? Toxicol Appl Pharmacol 257:182–188.

Fridovich I. 1970. Quantitative aspects of the production of superoxide anion radical by milk xanthine oxidase. J Biol Chem 245:4053–4057.

Fujitani Y, Furuyama A, Tanabe K, Hirano S. 2017. Comparison of oxidative abilities of $PM_{2.5}$ collected at traffic and residential sites in Japan. Contribution of transition metals and primary and secondary aerosols. Aerosol Air Qual Res 17:574–587.

Fuller SJ, Wragg FPH, Nutter J, Kalberer M. 2014. Comparison of on-line and off-line methods to quantify reactive oxygen species (ROS) in atmospheric aerosols. Atmos Environ 92:97–103.

Gao D, Fang T, Verma V, Zeng L, Weber R. 2017. A method for measuring total aerosol oxidative potential (OP) with the dithiothreitol (DTT) assay and comparisons between an urban and roadside site of water-soluble and total OP. Atmos Meas Tech Discuss 2017:1–25.

Garofalo LA, Pothier MA, Levin EJT, Campos T, Kreidenweis SM, Farmer DK. 2019. Emission and evolution of submicron organic aerosol in smoke from wildfires in the western United States. ACS Earth Space Chem 3:1237–1247.

Gehling W, Dellinger B. 2013. Environmentally persistent free radicals and their lifetimes in $PM_{2.5}$. Environ Sci Technol 47:8172–8178.

Ghio AJ, Richards JH, Dittrich KL, Samet JM. 1998. Metal storage and transport proteins increase after exposure of the rat lung to an air pollution particle. Toxicol Path 26:388–394.

Ghio AJ, Turi JL, Yang F, Garrick LM, Garrick MD. 2006. Iron homeostasis in the lung. Biol Res 39:67–77.

Gilbert BC, Holmes RG, Laue HA, Norman RO. 1976. Electron spin resonance studies. Part L. Reactions of alkoxyl radicals generated from alkyl hydroperoxides and titanium (III) ion in aqueous solution. J Chem Soc, Perkin Trans 2:1047–1052.

Gligorovski S, Strekowski R, Barbati S, Vione D. 2015. Environmental implications of hydroxyl radicals (·OH). Chem Rev 115:13051–13092.

Goldstein S, Meyerstein D. 1999. Comments on the mechanism of the "Fenton like" reaction. Acc Chem Res 32:547–550.

Golfetto O, Hinde E, Gratton E. 2013. Laurdan fluorescence lifetime discriminates cholesterol content from changes in fluidity in living cell membranes. Biophys J 104:1238–1247.

Gomes A, Fernandes E, Lima JLFC. 2005. Fluorescence probes used for detection of reactive oxygen species. J Biochem Biophys Methods 65:45–80.

Gonzalez DH, Cala CK, Peng Q, Paulson SE. 2017. Hulis enhancement of hydroxyl radical formation from Fe(II): Kinetics of fulvic acid–Fe(II) complexes in the presence of lung antioxidants. Environ Sci Technol 51:7676–7685.

Guin PS, Das S, Mandal PC. 2011. Electrochemical reduction of quinones in different media: A review. Int J Electrochem 2011:816202.

Guo H-b, Li M, Lyu Y, Cheng T-t, Xv J-j, Li X. 2019. Size-resolved particle oxidative potential in the office, laboratory, and home: Evidence for the importance of water-soluble transition metals. Environ Pollut 246:704–709.

Gurgueira SA, Lawrence J, Coull B, Murthy GG, Gonzalez-Flecha B. 2002. Rapid increases in the steady-state concentration of reactive oxygen species in the lungs and heart after particulate air pollution inhalation. Environ Health Perspect 110:749–755.

Gutteridge J. 1995. Lipid peroxidation and antioxidants as biomarkers of tissue damage. Clin Chem 41:1819–1828.

Hasson AS, Ho AW, Kuwata KT, Paulson SE. 2001. Production of stabilized Criegee intermediates and peroxides in the gas phase ozonolysis of alkenes: 2. Asymmetric and biogenic alkenes. J Geophys Res-Atmos 106:34143–34153.

Hayyan M, Hashim MA, AlNashef IM. 2016. Superoxide ion: Generation and chemical implications. Chem Rev 116:3029–3085.

He M, Ichinose T, Yoshida S, Ito T, He C, Yoshida Y, et al. 2017. $PM_{2.5}$-induced lung inflammation in mice: Differences of inflammatory response in macrophages and type II alveolar cells. J Appl Toxicol 37:1203–1218.

Herrmann H, Tilgner A, Barzaghi P, Majdik Z, Gligorovski S, Poulain L, et al. 2005. Towards a more detailed description of tropospheric aqueous phase organic chemistry: CAPRAM 3.0. Atmos Environ 39:4351–4363.

Heyder J. 2004. Deposition of inhaled particles in the human respiratory tract and consequences for regional targeting in respiratory drug delivery. Proc Am Thorac Soc 1:315–320.

Hiura TS, Kaszubowski MP, Li N, Nel AE. 1999. Chemicals in diesel exhaust particles generate reactive oxygen radicals and induce apoptosis in macrophages. J Immunol 163:5582–5591.

Hoffmann EH, Tilgner A, Wolke R, Böge O, Walter A, Herrmann H. 2018. Oxidation of substituted aromatic hydrocarbons in the tropospheric aqueous phase: Kinetic mechanism development and modelling. Phys Chem Chem Phys 20:10960–10977.

Holevinsky KO, Nelson DJ. 1995. Simultaneous detection of free radical release and membrane current during phagocytosis. J Biol Chem 270:8328–8336.

Hwang B, Fang T, Pham R, Wei J, Gronstal S, Lopez B, et al. 2021. Environmentally persistent free radicals, reactive oxygen species generation, and oxidative potential of highway $PM_{2.5}$. ACS Earth Space Chem 5:1865–1875.

Huang R-J, Zhang Y, Bozzetti C, Ho K-F, Cao J-J, Han Y, et al. 2014. High secondary aerosol contribution to particulate pollution during haze events in China. Nature 514:218–222.

ICRP. 1994. Publication 66: Human Respiratory Tract Model for Radiological Protection. Oxford, UK: Pergamon.

Jiang H, Jang M. 2018. Dynamic oxidative potential of atmospheric organic aerosol under ambient sunlight. Environ Sci Technol 52:7496–7504.

Jiang H, Jang M, Sabo-Attwood T, Robinson SE. 2016. Oxidative potential of secondary organic aerosols produced from photooxidation of different hydrocarbons using outdoor chamber under ambient sunlight. Atmos Environ 131:382–389.

Jimenez JL, Canagaratna MR, Donahue NM, Prevot ASH, Zhang Q, Kroll JH, et al. 2009. Evolution of organic aerosols in the atmosphere. Science 326:1525–1529.

Jokinen T, Berndt T, Makkonen R, Kerminen V-M, Junninen H, Paasonen P, et al. 2015. Production of extremely low volatile organic compounds from biogenic emissions: Measured yields and atmospheric implications. Proc Natl Acad Sci USA 112:7123–7128.

Jung H, Guo B, Anastasio C, Kennedy IM. 2006. Quantitative measurements of the generation of hydroxyl radicals by soot particles in a surrogate lung fluid. Atmos Environ 40:1043–1052.

Kaiser J. 2000. Evidence mounts that tiny particles can kill. Science 289:22–23.

Kang E, Root MJ, Toohey DW, Brune WH. 2007. Introducing the concept of potential aerosol mass (PAM). Atmos Chem Phys 7:5727–5744.

Kautzman KE, Surratt JD, Chan MN, Chan AWH, Hersey SP, Chhabra PS, et al. 2010. Chemical composition of gas- and aerosol-phase products from the photooxidation of naphthalene. J Phys Chem A 114:913–934.

Kenseth CM, Huang Y, Zhao R, Dalleska NF, Hethcox JC, Stoltz BM, et al. 2018. Synergistic O_3 + OH oxidation pathway to extremely low-volatility dimers revealed in β-pinene secondary organic aerosol. Proc Nat Acad Sci USA 115:8301–8306.

Khachatryan L, Vejerano E, Lomnicki S, Dellinger B. 2011. Environmentally persistent free radicals (EPFRs). 1. Generation of reactive oxygen species in aqueous solutions. Environ Sci Technol 45:8559–8566.

Khamkaew C, Chantara S, Janta R, Pani SK, Prapamontol T, Kawichai S, et al. 2016. Investigation of biomass burning chemical components over Northern Southeast Asia during 7-SEAS/BASELinE 2014 campaign. Aerosol Air Qual Res 16:2655–2670.

Kirkby J, Duplissy J, Sengupta K, Frege C, Gordon H, Williamson C, et al. 2016. Ion-induced nucleation of pure biogenic particles. Nature 533:521–526.

Kleeman MJ, Schauer JJ, Cass GR. 1999. Size and composition distribution of fine particulate matter emitted from wood burning, meat charbroiling, and cigarettes. Environ Sci Tech 33:3516–3523.

Kleinman MT, Bufalino C, Rasmussen R, Hyde D, Bhalla DK, Mautz WJ. 2000. Toxicity of chemical components of ambient fine particulate matter ($PM_{2.5}$) inhaled by aged rats. J Appl Toxicol 20:357–364.

Krapf M, El Haddad I, Bruns EA, Molteni U, Daellenbach KR, Prévôt ASH, et al. 2016. Labile peroxides in secondary organic aerosol. Chem-US 1:603–616.

Kumagai Y, Arimoto T, Shinyashiki M, Shimojo N, Nakai Y, Yoshikawa T, et al. 1997. Generation of reactive oxygen species during interaction of diesel exhaust particle components with NADPH-cytochrome P450 reductase and involvement of the bioactivation in the DNA damage. Free Radic Biol Med 22:479–487.

Kumagai Y, Shinkai Y, Miura T, Cho AK. 2012. The chemical biology of naphthoquinones and its environmental implications. Annu Rev Pharmacol Toxicol 52:221–247

Lakey PSJ, Berkemeier T, Tong H, Arangio AM, Lucas K, Pöschl U, et al. 2016. Chemical exposure-response relationship between air pollutants and reactive oxygen species in the human respiratory tract. Sci Rep 6:32916; doi.10.1038/srep32916.

Lambe AT, Ahern AT, Williams LR, Slowik JG, Wong JPS, Abbatt JPD, et al. 2011. Characterization of aerosol photooxidation flow reactors: Heterogeneous oxidation, secondary organic aerosol formation and cloud condensation nuclei activity measurements. Atmos Meas Tech 4:445–461.

Lambe AT, Chhabra PS, Onasch TB, Brune WH, Hunter JF, Kroll JH, et al. 2015. Effect of oxidant concentration, exposure time, and seed particles on secondary organic aerosol chemical composition and yield. Atmos Chem Phys 15:3063–3075.

Lee M, Heikes BG, Jacob DJ, Sachse G, Anderson B. 1997. Hydrogen peroxide, organic hydroperoxide, and formaldehyde as primary pollutants from biomass burning. J GeophyRes–Atmos 102:1301–1309.

Lelieveld J, Evans JS, Fnais M, Giannadaki D, Pozzer A. 2015. The contribution of outdoor air pollution sources to premature mortality on a global scale. Nature 525:367–371.

Lelieveld S, Wilson J, Dovrou E, Mishra A, Lakey PSJ, Shiraiwa M, et al. 2021. Hydroxyl radical production by air pollutants in epithelial lining fluid governed by interconversion and scavenging of reactive oxygen species. Environ Sci Technol 55:14069–14079.

Levin ME, Gonzales NO, Zimmerman LW, Yang J. 2006. Kinetics of acid-catalyzed cleavage of cumene hydroperoxide. J Hazard Mater 130:88–106.

Leviss DH, Van Ry DA, Hinrichs RZ. 2016. Multiphase ozonolysis of aqueous α-terpineol. Environ Sci Technol 50:11698–11705.

Li J-M, Shah AM. 2001. Differential NADPH– versus NADH–dependent superoxide production by phagocyte–type endothelial cell NADPH oxidase. Cardiovasc Res 52:477–486.

Li N, Alam J, Venkatesan MI, Eiguren-Fernandez A, Schmitz D, Di Stefano E, et al. 2004. Nrf2 is a key transcription factor that regulates antioxidant defense in macrophages and epithelial cells: Protecting against the proinflammatory and oxidizing effects of diesel exhaust chemicals. J Immunol 173:3467–3481.

Li N, Sioutas C, Cho AK, Schmitz D, Misra C, Sempf J, et al. 2003. Ultrafine particulate pollutants induce oxidative stress and mitochondrial damage. Environ Health Perspect 111:455–460.

Li N, Wang M, Oberley TD, Sempf JM, Nel AE. 2002. Comparison of the pro-oxidative and proinflammatory effects of organic diesel exhaust particle chemicals in bronchial epithelial cells and macrophages. J Immunol 169:4531–4341.

Li W, Ge P, Chen M, Tang J, Cao M, Cui Y, et al. 2021. Tracers from biomass burning emissions and identification of biomass burning. Atmosphere 12:1401.

Lim SS, Vos T, Flaxman AD, Danaei G, Shibuya K, Adair-Rohani H, et al. 2013. A comparative risk assessment of burden of disease and injury attributable to 67 risk factors and risk factor clusters in 21 regions, 1990-2010: A systematic analysis for the Global Burden of Disease Study 2010. Lancet 380:2224–2260.

Lin P, Yu JZ. 2011. Generation of reactive oxygen species mediated by humic-like substances in atmospheric aerosols. Environ Sci Technol 45:10362–10368.

Liu J, Banerjee S, Oroumiyeh F, Shen J, del Rosario I, Lipsitt J, et al. 2022. Cokriging with a low-cost sensor network to estimate spatial variation of brake and tire-wear metals and oxidative stress potential in Southern California. Environ Int 168:107481; doi:10.1016/j.envint.2022.107481.

Liu F, Saavedra MG, Champion JA, Griendling KK, Ng NL. 2020. Prominent contribution of hydrogen peroxide to intracellular reactive oxygen species generated upon exposure to naphthalene secondary organic aerosols. Environ Sci Technol Lett 7:171–177.

Los DA, Murata N. 2004. Membrane fluidity and its roles in the perception of environmental signals. Biochim Biophys Acta 1666:142–157.

Lucas K, Maes M. 2013. Role of the toll like receptor (TLR) radical cycle in chronic inflammation: Possible treatments targeting the TLR4 pathway. Mol Neurobiol 48:190–204.

Mathai JC, Sitaramam V. 1994. Stretch sensitivity of transmembrane mobility of hydrogen peroxide through voids in the bilayer. Role of cardiolipin. J Biol Chem 269:17784–17793.

McCord JM. 1985. Oxygen-derived free radicals in postischemic tissue injury. N Eng J Med 312:159–163.

McWhinney RD, Zhou S, Abbatt JPD. 2013. Naphthalene SOA: Redox activity and naphthoquinone gas–particle partitioning. Atmos Chem Phys 13:9731–9744.

Mentel TF, Springer M, Ehn M, Kleist E, Pullinen I, Kurtén T, et al. 2015. Formation of highly oxidized multifunctional compounds: Autoxidation of peroxy radicals formed in the ozonolysis of alkenes — deduced from structure–product relationships. Atmos Chem Phys 15:6745–6765.

Mertes P, Pfaffenberger L, Dommen J, Kalberer M, Baltensperger U. 2012. Development of a sensitive long path absorption photometer to quantify peroxides in aerosol particles (Peroxide-LOPAP). Atmos Meas Tech 5:2339–2348.

Messner KR, Imlay JA. 2002. In vitro quantitation of biological superoxide and hydrogen peroxide generation. Methods Enzymol 349:354–361.

Monks PS, Granier C, Fuzzi S, Stohl A, Williams ML, Akimoto H, et al. 2009. Atmospheric composition change – global and regional air quality. Atmos Environ 43:5268–5350.

Mudway IS, Kelly FJ. 2000. Ozone and the lung: A sensitive issue. Mol Aspects Med 21:1–48.

Nadezhdin AD, Dunford HB. 1979. The oxidation of ascorbic acid and hydroquinone by perhydroxyl radicals. A flash photolysis study. Can J Chem 57:3017–3022.

Nauser T, Gebicki JM. 2017. Reaction rates of glutathione and ascorbate with alkyl radicals are too slow for protection against protein peroxidation in vivo. Arch Biochem Biophys 633:118–123.

Nel A. 2005. Air pollution–related illness: Effects of particles. Science 308:804–806.

Nguyen GT, Green ER, Mecsas J. 2017. Neutrophils to the ROScue: Mechanisms of NADPH oxidase activation and bacterial resistance. Front Cell Infect Microbiol 7:373.

Nguyen TB, Bateman AP, Bones DL, Nizkorodov SA, Laskin J, Laskin A. 2010. High-resolution mass spectrometry analysis of secondary organic aerosol generated by ozonolysis of isoprene. Atmos Environ 44:1032–1042.

Offer S, Hartner E, Di Bucchianico S, Bisig C, Bauer S, Pantzke J, et al. 2022. Effect of atmospheric aging on soot particle toxicity in lung cell models at the air–liquid interface: Differential toxicological impacts of biogenic and anthropogenic secondary organic aerosols (SOAs). Environ Health Perspect 130:027003.

Panday A, Sahoo MK, Osorio D, Batra S. 2015. NADPH oxidases: An overview from structure to innate immunity–associated pathologies. Cell Mol Immuno 12:5–23.

Pardo M, Qiu X, Zimmermann R, Rudich Y. 2020. Particulate matter toxicity is NRF2 and mitochondria dependent: The roles of metals and polycyclic aromatic hydrocarbons. Chem Res Toxicol 33:1110–1120.

Pate KT, Stringari C, Sprowl–Tanio S, Wang K, TeSlaa T, Hoverter NP, et al. 2014. Wnt signaling directs a metabolic program of glycolysis and angiogenesis in colon cancer. EMBO J 33:1454–1473.

Pavlovic J, Hopke PK. 2010. Detection of radical species formed by the ozonolysis of α-pinene. J Atmos Chem 66:137–155.

Pedersen JA. 1985. Handbook of EPR Spectra from Quinones and Quinols. Boca Raton, FL:CRC Press.

Peng Z, Jimenez JL. 2020. Radical chemistry in oxidation flow reactors for atmospheric chemistry research. Chem Soc Rev 49:2570–2616.

Phalen RF, Oldham MJ, Nel AE. 2006. Tracheobronchial particle dose considerations for in vitro toxicology studies. Toxicol Sci 92:126–132.

Pope CA, Dockery DW. 2006. Health effects of fine particulate air pollution: Lines that connect. J Air Waste Manag Assoc 56:709–742.

Porra L, Dégrugilliers L, Broche L, Albu G, Strengell S, Suhonen H, et al. 2018. Quantitative imaging of regional aerosol deposition, lung ventilation and morphology by synchrotron radiation CT. Sci Repo 8:3519.

Pöschl U, Shiraiwa M. 2015. Multiphase chemistry at the atmosphere–biosphere interface influencing climate and public health in the anthropocene. Chem Rev 115:4440–4475.

Pospisilova V, Lopez–Hilfiker FD, Bell DM, El Haddad I, Mohr C, Huang W, et al. 2020. On the fate of oxygenated organic molecules in atmospheric aerosol particles. Sci Adv 6:eaax8922.

Pryor WA, Squadrito GL, Friedman M. 1995. The cascade mechanism to explain ozone toxicity – the role of lipid ozonation products. Free Radical Biol Med 19:935–941.

Qiu J, Liang Z, Tonokura K, Colussi AJ, Enami S. 2020a. Stability of monoterpene–derived α–hydroxyalkyl–hydroperoxides in aqueous organic media: Relevance to the fate of hydroperoxides in aerosol particle phases. Environ Sci Technol 54:3890–3899.

Qiu J, Tonokura K, Enami S. 2020b. Proton–catalyzed decomposition of α–hydroxyalkyl-hydroperoxides in water. Environ Sci Technol 54:10561–10569.

Ranjit S, Malacrida L, Stakic M, Gratton E. 2019. Determination of the metabolic index using the fluorescence lifetime of free and bound nicotinamide adenine dinucleotide using the phasor approach. J Biophotonics 12:e201900156.

Rehman AU, Anwer AG, Gosnell ME, Mahbub SB, Liu G, Goldys EM. 2017. Fluorescence quenching of free and bound NADH in HeLa cells determined by hyperspectral imaging and unmixing of cell autofluorescence. Biomed Opt Express 8:1488–1498.

Rich DQ, Ozkaynak H, Crooks J, Baxter L, Burke J, Ohman–Strickland P, et al. 2013. The triggering of myocardial infarction by fine particles is enhanced when particles are enriched in secondary species. Environ Sci Tech 47:9414–9423.

Ripley S, Minet L, Zalzal J, Godri Pollitt K, Gao D, Lakey PSJ, et al. 2022. Predicting spatial variations in multiple measures of $PM_{2.5}$ oxidative potential and magnetite nanoparticles in Toronto and Montreal, Canada. Environ Sci Technol 56:7256–7265; doi:10.1021/acs.est.1c05364.

Riva M. 2016. Multiphase chemistry of highly oxidized molecules: The case of organic hydroperoxides. Chem 1:526–528.

Sachse A, Wolf G. 2007. Angiotensin II–induced reactive oxygen species and the kidney. J Am Soc Nephrol 18:2439–2446.

Saffari A, Daher N, Shafer MM, Schauer JJ, Sioutas C. 2014. Seasonal and spatial variation in dithiothreitol (DTT) activity of quasi-ultrafine particles in the Los Angeles Basin and its association with chemical species. J Environ Sci Health A Tox Hazard Subst Environ Eng 49:441–451.

Sanchez J, Myers TN. 2004. Peroxides and Peroxide Compounds, Organic Peroxides. In Kirk–Othmer Encyclopedia of Chemical Technology (5th edition). Hoboken, NJ:Wiley Interscience,1–86.

Santana-Casiano JM, González-Dávila M, Millero FJ. 2005. Oxidation of nanomolar levels of Fe(II) with oxygen in natural waters. Environ Sci Technol 39:2073–2079.

Sato K, Hatakeyama S, Imamura T. 2007. Secondary organic aerosol formation during the photooxidation of toluene: NO_x dependence of chemical composition. J Phys Chem 111:9796–9808.

Sauer F, Schafer C, Neeb P, Horie O, Moortgat GK. 1999. Formation of hydrogen peroxide in the ozonolysis of isoprene and simple alkenes under humid conditions. Atmos Environ 33:229–241.

Schwantes RH, Schilling KA, McVay RC, Lignell H, Coggon MM, Zhang X, et al. 2017. Formation of highly oxygenated low-volatility products from cresol oxidation. Atmos Chem Phys 17:3453–3474.

Shahpoury P, Zhang ZW, Filippi A, Hildmann S, Lelieveld S, Mashtakov B, et al. 2022. Inter-comparison of oxidative potential metrics for airborne particles identifies differences between acellular chemical assays. Atmos Poll Res 13:101596.

Shen H, Anastasio C. 2011. Formation of hydroxyl radical from San Joaquin Valley particles extracted in a cell–free surrogate lung fluid. Atmos Chem Phys 11:9671–9682.

Shen J, Griffiths PT, Campbell SJ, Utinger B, Kalberer M, Paulson SE. 2021. Ascorbate oxidation by iron, copper and reactive oxygen species: Review, model development, and derivation of key rate constants. Sci Rep 11:7417.

Shiraiwa M, Selzle K, Pöschl U. 2012. Hazardous components and health effects of atmospheric aerosol particles: Reactive oxygen species, soot, polycyclic aromatic compounds and allergenic proteins. Free Radical Res 46:927–939.

Shiraiwa M, Ueda K, Pozzer A, Lammel G, Kampf CJ, Fushimi A, et al. 2017. Aerosol health effects from molecular to global scales. Environ Sci Technol 51:13545–13567.

Shirmohammadi F, Hasheminassab S, Wang D, Saffari A, Schauer JJ, Shafer MM, et al. 2015. Oxidative potential of coarse particulate matter ($PM_{10-2.5}$) and its relation to water solubility and sources of trace elements and metals in the Los Angeles Basin. Environ Sci: Processes Impacts 17:2110–2121.

Shirmohammadi F, Wang D, Hasheminassab S, Verma V, Schauer JJ, Shafer MM, et al. 2017. Oxidative potential of on-road fine particulate matter ($PM_{2.5}$) measured on major freeways of Los Angeles, CA, and a 10-year comparison with earlier roadside studies. Atmos Environ 148:102–114.

Sies H, Berndt C, Jones DP. 2017. Oxidative stress. Annu Rev Biochem 86:715–748.

Snow JA, Heikes BG, Shen H, O'Sullivan DW, Fried A, Walega J. 2007. Hydrogen peroxide, methyl hydroperoxide, and formaldehyde over North America and the North Atlantic. J Geophys Res Atmos 112(D12); doi:*10.1029/2006JD007746*.

Sompayrac LM. 2022. How the immune system works. Malden, MA:John Wiley & Sons.

Stieb DM, Evans GJ, To TM, Lakey PSJ, Shiraiwa M, Hatzopoulou M, et al. 2021. Within–city variation in reactive oxygen species from fine particle air pollution and COVID–19. Am J Respir Crit Care Med 204:168–177.

Stoll S, Schweiger A. 2006. Easyspin, a comprehensive software package for spectral simulation and analysis in EPR. J Mag Reson 178:42–55.

Stringari C, Cinquin A, Cinquin O, Digman MA, Donovan PJ, Gratton E. 2011. Phasor approach to fluorescence lifetime microscopy distinguishes different metabolic states of germ cells in a live tissue. Proc Natl Acad Sci USA 108:13582.

Stringari C, Edwards RA, Pate KT, Waterman ML, Donovan PJ, Gratton E. 2012. Metabolic trajectory of cellular differentiation in small intestine by phasor fluorescence lifetime microscopy of NADH. Sci Rep 2:568.

Studer A, Curran DP. 2016. Catalysis of radical reactions: A radical chemistry perspective. Angew Chem Int Ed Engl 55:58–102.

Sun H, Xie G, He D, Zhang L. 2020. Ascorbic acid promoted magnetite Fenton degradation of alachlor: Mechanistic insights and kinetic modeling. Applied Catalysis B:Environmental 267:118383; doi.10.1016/j.apcatb.2019.118383.

Surratt JD, Murphy SM, Kroll JH, Ng NL, Hildebrandt L, Sorooshian A, et al. 2006. Chemical composition of secondary organic aerosol formed from the photooxidation of isoprene. J Phys Chem A 110:9665–9690.

Teufelhofer O, Weiss R-M, Parzefall W, Schulte-Hermann R, Micksche M, Berger W, et al. 2003. Promyelocytic HL60 cells express NADPH oxidase and are excellent targets in a rapid spectrophotometric microplate assay for extracellular superoxide. Toxicol Sci 76:376–383.

Tilgner A, Herrmann H. 2018. Tropospheric aqueous-phase OH oxidation chemistry: Current understanding, uptake of highly oxidized organics and its effects. In: Multiphase environmental chemistry in the atmosphere. Washington DC:American Chemical Society, 1299:49–85.

To T, Terebessy E, Zhu J, Zhang K, Lakey PSJ, Shiraiwa M, et al. 2022. Does early life exposure to exogenous sources of reactive oxygen species (ROS) increase the risk of respiratory and allergic diseases in children? A longitudinal cohort study. Environ Health 21:90; doi:10.1186/s12940-022-00902-7.

Togashi DM, Nicodem DE. 2004. Photophysical studies of 9,10-phenanthrenequinones. Spectrochim Acta A Mol Biomol Spectrosc 60:3205–3212.

Tong H, Arangio AM, Lakey PSJ, Berkemeier T, Liu F, Kampf CJ, et al. 2016. Hydroxyl radicals from secondary organic aerosol decomposition in water. Atmos Chem Phys 16:1761–1771.

Tong H, Lakey PSJ, Arangio AM, Socorro J, Kampf CJ, Berkemeier T, et al. 2017. Reactive oxygen species formed in aqueous mixtures of secondary organic aerosols and mineral dust influencing cloud chemistry and public health in the anthropocene. Faraday Discuss 200:251–270.

Tong H, Lakey PSJ, Arangio AM, Socorro J, Shen F, Lucas K, et al. 2018. Reactive oxygen species formed by secondary organic aerosols in water and surrogate lung fluid. Environ Sci Technol 52:11642–11651.

Tröstl J, Chuang WK, Gordon H, Heinritzi M, Yan C, Molteni U, et al. 2016. The role of low–volatility organic compounds in initial particle growth in the atmosphere. Nature 533:527–531.

Tsai P, Ichikawa K, Mailer C, Pou S, Halpern HJ, Robinson BH, et al. 2003. Esters of 5-Carboxyl-5-methyl-1-pyrroline *N*-Oxide: A family of spin traps for superoxide. J Org Chem 68:7811–7817.

Tuet WY, Chen Y, Fok S, Champion JA, Ng NL. 2017a. Inflammatory responses to secondary organic aerosols (SOA) generated from biogenic and anthropogenic precursors. Atmos Chem Phys 17:11423–11440.

Tuet WY, Chen Y, Xu L, Fok S, Gao D, Weber RJ, et al. 2017b. Chemical oxidative potential of secondary organic aerosol (SOA) generated from the photooxidation of biogenic and anthropogenic volatile organic compounds. Atmos Chem Phys 17:839–853.

Valko M, Morris H, Cronin MTD. 2005. Metals, toxicity and oxidative stress. Curr Med Chem 12:1161–1208.

van der Vliet A, O'Neill CA, Cross CE, Koostra JM, Volz WG, Halliwell B, et al. 1999. Determination of low–molecular–mass antioxidant concentrations in human respiratory tract lining fluids. Am J Physiol-Lung C 276:L289–L296.

Venkatachari P, Hopke PK, Brune WH, Ren X, Lesher R, Mao J, et al. 2007. Characterization of wintertime reactive oxygen species concentrations in Flushing, New York. Aerosol Sci Technol 41:97–111.

Venkatachari P, Hopke PK, Grover BD, Eatough DJ. 2005. Measurement of particle-bound reactive oxygen species in rubidoux aerosols. J Atmos Chem 50:49–58.

Vereecken L, Francisco JS. 2012. Theoretical studies of atmospheric reaction mechanisms in the troposphere. Chem Soc Rev 41:6259–6293.

Verma V, Fang T, Xu L, Peltier RE, Russell AG, Ng NL, et al. 2015a. Organic aerosols associated with the generation of reactive oxygen species (ROS) by water-soluble $PM_{2.5}$. Environ Sci Technol 49:4646–4656.

Verma V, Wang Y, El-Afifi R, Fang T, Rowland J, Russell AG, et al. 2015b. Fractionating ambient humic-like substances (HULIS) for their reactive oxygen species activity – Assessing the importance of quinones and atmospheric aging. Atmos Environ 120:351–359.

Vicente ED, Alves CA, Martins V, Almeida SM, Lazaridis M. 2021. Lung-deposited dose of particulate matter from residential exposure to smoke from wood burning. Environ Sci Poll Res 28:65385–65398.

Vidrio E, Jung H, Anastasio C. 2008. Generation of hydroxyl radicals from dissolved transition metals in surrogate lung fluid solutions. Atmos Environ 42:4369–4379.

Villamena FA, Merle JK, Hadad CM, Zweier JL. 2005. Superoxide radical anion adduct of 5,5–dimethyl–1–pyrroline *N*–oxide (DMPO). 1. The thermodynamics of formation and its acidity. J Phys Chem A 109:6083–6088.

Voelker BM, Sedlak DL. 1995. Iron reduction by photoproduced superoxide in seawater. Mar Chem 50:93–102.

Walczak MM, Dryer DA, Jacobson DD, Foss MG, Flynn NT. 1997. pH dependent redox couple: An illustration of the Nernst equation. J Chem Educ 74:1195.

Walling C. 1963. Chemistry of the organic peroxides. Radiat Res Sup 3:3–16.

Wang S, Takhar M, Zhao Y, Al Rashdi LNS, Chan AWH. 2021. Dynamic oxidative potential of organic aerosol from heated cooking oil. ACS Earth Space Chem 5:1150–1162.

Wang X, Ho K-F, Chow JC, Kohl SD, Chan CS, Cui L, et al. 2018. Hong Kong vehicle emission changes from 2003 to 2015 in the Shing Mun Tunnel. Aerosol Sci Tech 52:1085–1098.

Wang Y, Arellanes C, Curtis DB, Paulson SE. 2010. Probing the source of hydrogen peroxide associated with coarse mode aerosol particles in Southern California. Environ Sci Technol 44:4070–4075.

Wang Y, Arellanes C, Paulson SE. 2012. Hydrogen peroxide associated with ambient fine-mode, diesel, and biodiesel aerosol particles in Southern California. Aerosol Sci Technol 46:394–402.

Wang Y, Hopke PK, Sun L, Chalupa DC, Utell MJ. 2011a. Laboratory and field testing of an automated atmospheric particle–bound reactive oxygen species sampling–analysis system. J Toxicol 2011.

Wang Y, Kim H, Paulson SE. 2011b. Hydrogen peroxide generation from α- and β-pinene and toluene secondary organic aerosols. Atmos Environ 45:3149–3156.

Weber G. 1981. Resolution of the fluorescence lifetimes in a heterogeneous system by phase and modulation measurements. J Phys Chem 85:949–953.

Wei J, Fang T, Lakey PSJ, Shiraiwa M. 2021a. Iron-facilitated organic radical formation from secondary organic aerosols in surrogate lung fluid. Environ Sci Technol 56:7234–7243; doi.10.1021/acs.est.1c04334.

Wei J, Fang T, Shiraiwa M. 2022. Effects of acidity on reactive oxygen species formation from secondary organic aerosols. ACS Environmental Au 2:336–345; doi.10.1021/acsenvironau.2c00018.

Wei J, Fang T, Wong C, Lakey PSJ, Nizkorodov SA, Shiraiwa M. 2021b. Superoxide formation from aqueous reactions of biogenic secondary organic aerosols. Environ Sci Technol 55:260–270.

Wei J, Yu H, Wang Y, Verma V. 2019. Complexation of iron and copper in ambient particulate matter and its effect on the oxidative potential measured in a surrogate lung fluid. Environ Sci Technol 53:1661–1671.

West JJ, Cohen A, Dentener F, Brunekreef B, Zhu T, Armstrong B, et al. 2016. What we breathe impacts our health: Improving understanding of the link between air pollution and health. Environ Sci Technol 50:4895–4904.

Wientjes FB, Segal AW. 1995. NADPF oxidase and the respiratory burst. Semin Cell Biol 6:357–365.

Winterbourn CC. 2008. Reconciling the chemistry and biology of reactive oxygen species. Nature Chem Biol 4:278–286.

Xiong Q, Yu H, Wang R, Wei J, Verma V. 2017. Rethinking dithiothreitol–based particulate matter oxidative potential: Measuring dithiothreitol consumption versus reactive oxygen species generation. Environ Sci Technol 51:6507–6514.

Yamazaki T, Kawai C, Yamauchi A, Kuribayashi F. 2011. A highly sensitive chemiluminescence assay for superoxide detection and chronic granulomatous disease diagnosis. Trop Med Health 39:41–45.

Yang X, Ma K. 2007. Characterization of an exceedingly active NADH oxidase from the anaerobic hyperthermophilic bacterium thermotoga maritima. J Bacteriol 189:3312–3317.

Yaremenko IA, Vil' VA, Demchuk DV, Terent'ev AO. 2016. Rearrangements of organic peroxides and related processes. Beilstein J Org Chem 12:1647–1748.

Yin H, Xu L, Porter NA. 2011. Free radical lipid peroxidation: Mechanisms and analysis. Chem Rev 111:5944–5972

Yuan X, Miller CJ, Pham AN, Waite TD. 2014. Kinetics and mechanism of auto– and copper–catalyzed oxidation of 1,4–naphthohydroquinone. Free Radic Bio Med 71:291–302.

Zhang X, Lambe AT, Upshur MA, Brooks WA, Gray Bé A, Thomson RJ, et al. 2017. Highly oxygenated multifunctional compounds in α-pinene secondary organic aerosol. Environ Sci Technol 51:5932–5940.

Zhang X, Staimer N, Tjoa T, Gillen DL, Schauer JJ, Shafer MM, et al. 2016. Associations between microvascular function and short–term exposure to traffic–related air pollution and particulate matter oxidative potential. Environ Health 15:81.

Zhang ZH, Hartner E, Utinger B, Gfeller B, Paul A, Sklorz M, et al. 2022. Are reactive oxygen species (ROS) a suitable metric to predict toxicity of carbonaceous aerosol particles? Atmos Chem Phys 22:1793–1809.

Zhang Z, Weichenthal S, Kwong JC, Burnett RT, Hatzopoulou M, Jerrett M, et al. 2020. Long-term exposure to iron and copper in fine particulate air pollution and their combined impact on reactive oxygen species concentration in lung fluid: A population-based cohort study of cardiovascular disease incidence and mortality in Toronto, Canada. Int J Epidemiol 50:589–601; doi.10.1093/ije/dyaa230.

Zhang Z, Weichenthal S, Kwong JC, Burnett RT, Hatzopoulou M, Jerrett M, et al. 2021. A population-based cohort study of respiratory disease and long-term exposure to iron and copper in fine particulate air pollution and their combined impact on reactive oxygen species generation in human lungs. Environ Sci Technol 55:3807–3818.

Zhao H, Joseph J, Zhang H, Karoui H, Kalyanaraman B. 2001. Synthesis and biochemical applications of a solid cyclic nitrone spin trap: A relatively superior trap for detecting superoxide anions and glutathiyl radicals. Free Radical Biol Med 31:599–606.

Zhao J, Hopke PK. 2012. Concentration of reactive oxygen species (ROS) in mainstream and sidestream cigarette smoke. Aerosol Sci Technol 46:191–197.

Ziemann PJ. 2002. Evidence for low volatility diacyl peroxides as a nucleating agent and major component of aerosol formed from reactions of O_3 with cyclohexene and homologous compounds. J Phys Chem A 106:4390–4402.

Ziemann PJ, Atkinson R. 2012. Kinetics, products, and mechanisms of secondary organic aerosol formation. Chem Soc Rev 41:6582–6605.

ABOUT THE AUTHORS

Manabu Shiraiwa is Professor of Chemistry at UCI. He received a B.S. and an M.S. at the University of Tokyo and a Ph.D. from the Max Planck Institute for Chemistry in 2011. He has worked as a group leader at the Max Planck Institute for Chemistry and as a JSPS postdoc fellow at the California Institute of Technology. He is the lead PI of this project. His primary research interests are multiphase chemistry of atmospheric aerosols and their impacts on climate, outdoor and indoor air quality, and public health.

Ting Fang was a postdoctoral researcher working with Dr. Shiraiwa in the Department of Chemistry at UCI. She received a Ph.D. at the Georgia Institute of Technology and is currently Assistant Professor at HKUST Guangzhou.

Jinlai Wei was a graduate student working with Dr. Shiraiwa in the Department of Chemistry at UCI and received a Ph.D. in 2022.

Pascale S.J. Lakey is a project scientist working with Dr. Shiraiwa in the Department of Chemistry at UCI. She received a Ph.D. from the University of Leeds, UK.

Brian C.H. Hwang was a graduate student working with Dr. Shiraiwa in the Department of Chemistry at UCI and received a Ph.D. in 2021.

Kasey C. Edwards is a graduate student working with Dr. Shiraiwa in the Department of Chemistry at UCI.

Sukriti Kapur is a graduate student working with Dr. Shiraiwa in the Department of Chemistry at UCI.

Jessica E. Monterrosa Mena is a graduate student working with Dr. Kleinman in the Division of Occupational and Environmental Medicine at UCI.

Yu-Kai Huang is a graduate student working with Dr. Digman in the Department of Biomedical Engineering at UCI.

Michelle A. Digman is Associate Professor in the Department of Biomedical Engineering at UCI.

Scott A. Weichenthal is Associate Professor in the Department of Epidemiology, Biostatistics and Occupational Health at McGill University, Canada.

Sergey Nizkorodov is Professor of Chemistry in the Department of Chemistry at UCI.

Michael T. Kleinman is Professor of Environmental Toxicology in the Division of Occupational and Environmental Medicine at UCI.

OTHER PUBLICATIONS RESULTING FROM THIS RESEARCH

Fang T, Hwang BCH, Kapur S, Hopstock K, Wei J, Nguyen V, Nizkorodov SA, Shiraiwa M. 2023. Wildfire particulate matter as a source of environmentally persistent free radicals and reactive oxygen species. Environ Sci Atmos 3:581–594.

Fang T, Huang Y-K, Wei J, Monterrosa Mena JE, Lakey PSJ, Kleinman MT, Digman MA, Shiraiwa, M. 2022. Superoxide release by macrophages through NADPH oxidase activation dominating chemistry by isoprene secondary organic aerosols and quinones to cause oxidative damage on membranes. Environ Sci Technol 56:17029–17038; doi.10.1021/acs.est.2c03987.

Liu J, Banerjee S, Oroumiyeh F, Shen J, del Rosario I, Lipsitt J, Paulson S, Ritz B, Su J, Weichenthal S, Lakey P, Shiraiwa M, Zhu Y, Jerrett M. 2022. Cokriging with a low-cost sensor network to estimate spatial variation of brake and tire-wear metals and oxidative stress potential in Southern California. Environ Int 168:107481; doi:10.1016/j.envint.2022.107481.

Ripley S, Minet L, Zalzal J, Godri Pollitt K, Gao D, Lakey PSJ, Shiraiwa M, Maher BA, Hatzopoulou M, Weichenthal S. 2022. Predicting spatial variations in multiple measures of $PM_{2.5}$ oxidative potential and magnetite nanoparticles in Toronto and Montreal, Canada. Environ Sci Technol 56:7256–7265; doi:10.1021/acs.est.1c05364.

To T, Terebessy E, Zhu J, Zhang K, Lakey PSJ, Shiraiwa M, Hatzopoulou M, Minet L, Weichenthal S, Dell S, Stieb D. 2022. Does early life exposure to exogenous sources of reactive oxygen species (ROS) increase the risk of respiratory and allergic diseases in children? A longitudinal cohort study. Environ Health 21:90; doi:10.1186/s12940-022-00902-7.

Wei J, Fang T, Lakey PSJ, Shiraiwa M. 2021. Iron-facilitated organic radical formation from secondary organic aerosols in surrogate lung fluid. Environ Sci Technol 56:7234–7243; doi.10.1021/acs.est.1c04334.

Wei J, Fang T, Shiraiwa M. 2022. Effects of acidity on reactive oxygen species formation from secondary organic aerosols. ACS Environ 2:336–345; doi.10.1021/acsenvironau.2c00018.

Hwang B, Fang T, Pham R, Wei J, Gronstal S, Lopez B, Frederickson C, Galeazzo T, Wang X, JungH, Shiraiwa M. 2021. Environmentally persistent free radicals, reactive oxygen species generation, and oxidative potential from highway $PM_{2.5}$. ACS Earth Space Chem 5:1865–1875.

Lelieveld S, Wilson J, Dovrou E, Mishra A, Lakey PSJ, Shiraiwa M, Pöschl U, Berkemeier T. 2021. Hydroxyl radical production by air pollutants in epithelial lining fluid governed by interconversion and scavenging of reactive oxygen species. Environ Sci Technol 55:14069–14079.

Stieb DM, Evans GJ, To TM, Lakey PSJ, Shiraiwa M, Hatzopoulou M, et al. 2021. Within-city variation in reactive oxygen species from fine particle air pollution and COVID-19. Am J Respir Crit Care Med 204:168–177.

Wei J, Fang T, Wong C, Lakey PSJ, Nizkorodov SA, Shiraiwa M. 2021. Superoxide formation from aqueous reactions of biogenic secondary organic aerosols. Environ. Sci Technol 55:260–270; doi.10.1021/acs.est.0c07789.

Zhang Z, Weichenthal S, Kwong JC, Burnett R T, Hatzopoulou M, Jerrett M, van Donkelaar A, Bai L, Martin RV, Copes R, Lu H, Lakey P, Shiraiwa M, Chen H. 2021. A population-based cohort study of respiratory disease and long-term exposure to iron and copper in fine particulate air pollution and their combined impact on reactive oxygen species generation in human lungs. Environ Sci Technol 55:3807–3818.

Zhang Z, Weichenthal S, Kwong JC, Burnett RT, Hatzopoulou M, Jerrett M, van Donkelaar A, Bai, L, Martin RV, Copes R, Lu H, Lakey P, Shiraiwa M, Chen H. 2020. Long-term exposure to iron and copper in fine particulate air pollution and their combined impact on reactive oxygen species concentration in lung fluid: A population-based cohort study of cardiovascular disease incidence and mortality in Toronto, Canada. Int J Epidemiol 50:589–601; doi.10.1093/ije/dyaa230.

Fang T, Lakey PSJ, Weber RJ, Shiraiwa M. 2019. Oxidative potential of particulate matter and generation of reactive oxygen species in epithelial lining fluid, Environ Sci Technol 53:12784–12792; doi.10.1021/acs.est.9b03823.